Universität für Bodenkultur Wien
University of Natural Resources
and Life Sciences, Vienna

Master Thesis

Rolling circle amplification for plasmonic biosensors: from ensembles to single molecule detection format

Submitted by

Katharina SCHMIDT, BSc

in the framework of the Master programme

Nanobioscience

in partial fulfilment of the requirements for the academic degree

Master

Vienna, 2nd September 2021

Supervisors: Dr. Jakub Dostálek – Biosensor Technologies (AIT)
Univ.Prof. Dr. Erik Reimhult - Department of Nanobiotechnology (BOKU)

Universität für Bodenkultur Wien
University of Natural Resources
and Life Sciences, Vienna

Affidavits

I hereby declare that I am the sole author of this work. No assistance other than that which is permitted has been used. Ideas and quotes taken directly or indirectly from other sources are identified as such. This written work has not yet been submitted in any part.

Eidesstattliche Erklärungen

Ich erkläre eidesstattlich, dass ich die Arbeit selbständig angefertigt habe. Es wurden keine anderen als die angegebenen Hilfsmittel benutzt. Die aus fremden Quellen direkt oder indirekt übernommenen Formulierungen und Gedanken sind als solche kenntlich gemacht. Diese schriftliche Arbeit wurde noch an keiner Stelle vorgelegt.

Katharina Schmidt, September 2021

Acknowledgments

To begin with, I would like to express my gratitude to Dr. Jakub Dostálek who gave me the great opportunity to work in his research group at AIT. I am glad that I had the chance to develop new skills and gather valuable experiences through his guidance and constant support, which enabled me to write this thesis.

Furthermore, I am grateful to Prof. Dr. Erik Reimhult who is a great supervisor and always supported me with valuable information throughout my studies. In particular, he was helpful and quick in reviewing my thesis.

I would also like to thank Dipl.-Ing.in Simone Hageneder and Dipl.-Ing.in Bernadette Lechner for their patient explanations and useful instructions. They shared their scientific knowledge and taught me everything I needed for the successful completion of the practical lab work.

Above all, however, I would like to express my deepest gratitude to my parents, my sister and my loved ones. They constantly supported me and always had an open mind and ear for my worries. Without their encouragement, I might not have been able to achieve my ambitious goals within the given time frame.

Abstract

Rolling circle amplification (RCA) evolved to an established method in bioanalytical technologies for sensitive detection of biomolecules. It has been implemented for single molecule detection in bulk solution and for assays on the surface. This thesis investigates single stranded deoxyribonucleic acid (ssDNA) generated on the solid surface by using RCA with surface plasmon resonance (SPR) and surface plasmon-enhanced fluorescence spectroscopy (SPFS). It is utilized for the *in-situ* monitoring of the growth of ssDNA chains depending on the grafting density, response to specific ions, and affinity reaction with additional short ssDNA strands serving as staples or surface anchors.

The performed study reveals changes in the ssDNA conformation taking the long brush form or individual ssDNA coil that is modulated by the interaction with calcium ions and can be amended by the affinity staples and anchors. The study interrogates ensembles of ssDNA chains in the range of several nm (when quenching of fluorescence occurs at the metal surface) to several µm (when optical modes can be excited in the ssDNA layer). Moreover, fluorescence microscopy was performed in the regime of sparsely attached chains when individual molecules are observed.

The achieved results reveal possible mechanisms that can serve in ultrasensitive optical biosensors. When using the RCA for generating long ssDNA chains labelled with multiple fluorophores, the SPFS readout principle allowed improving the limit of detection (LOD) from 13 pM range (compared to the analyte with only one fluorophore) to 0.26 pM. When the readout is performed in imaging modality enabling counting individual chains, the LOD can be pushed to the low fM concentrations. This approach allows to facile implementation of digital readout of the assay. It holds potential to utilize the platform for future rapid multiplexed high-throughput analysis of molecular analytes to combat the raising problem of antibiotic resistant pathogens.

Zusammenfassung

Die Rolling-Circle-Amplifikation (RCA) hat sich zu einer etablierten Methode in der Bioanalytik zum Nachweis von Biomolekülen entwickelt. Sie wurde für den Einzelmolekülnachweis in Lösung und an der Oberfläche eingesetzt. In dieser Arbeit wird einzelsträngige Desoxyribonukleinsäure (ssDNA) untersucht, die auf einer Oberfläche erzeugt wird, indem RCA mit Oberflächenplasmonenresonanz (SPR) und Plasmonenfeld-verstärkter Fluoreszenzspektroskopie (SPFS) eingesetzt wird. Sie wird für die in-situ-Überwachung des Wachstums von ssDNA in Abhängigkeit von der Dichte, der Reaktion auf Ionen und der Affinität mit zusätzlichen kurzen ssDNA-Strängen, die als Klammern oder Anker dienen, eingesetzt.

Die durchgeführte Studie zeigt Veränderungen in der ssDNA-Konformation in Form einer langen Bürste oder einer einzelnen Spule, die durch die Wechselwirkung mit Kalziumionen moduliert wird und durch Klammern und Anker verändert werden kann. Es werden ssDNA-Ketten im Bereich von einigen nm bis zu mehreren µm untersucht. Außerdem wurde Fluoreszenzmikroskopie im Bereich der spärlich gebundenen Ketten durchgeführt, bei der einzelne Moleküle beobachtet werden.

Die erzielten Ergebnisse zeigen mögliche Mechanismen auf, die in ultrasensiblen optischen Biosensoren eingesetzt werden können. Bei der Verwendung der RCA zur Erzeugung langer ssDNA-Ketten, die mit mehreren Fluorophoren markiert sind, ermöglichte das SPFS-Ausleseprinzip eine Verbesserung der Nachweisgrenze (LOD) von 13 pM (verglichen mit dem Analyten mit nur einem Fluorophor) auf 0.26 pM. Wenn die Auslesung in der Bildgebungsmodalität durchgeführt wird, die das Zählen einzelner Ketten ermöglicht, kann niedrige LOD im fM-Bereich erreicht werden. Dieser Ansatz ermöglicht eine einfache Implementierung der digitalen Auslesung. Er birgt das Potenzial, die Plattform in Zukunft für die schnelle Multiplex-Hochdurchsatzanalyse molekularer Analyten zu nutzen, um das zunehmende Problem antibiotikaresistenter Krankheitserreger zu bekämpfen.

Contents

List of Abbreviations

BRE	Biorecognition Element
DNA	Deoxyribonucleic Acid
ELISA	Enzyme-linked immunosorbent assay
LOD	Limit of detection
MRE	Microfluidic RCA product enrichment
OXA	Oxacillinase
PCR	Polymerase Chain Reaction
PEF	Plasmon-enhanced Fluorescence
PLP	Padlock Probe
PSP	Propagating Surface Plasmon
RCA	Rolling Circle Amplification
RIU	Refractive Index Unit
RNA	Ribonucleic Acid
rRNA	Ribosomal Ribonucleic Acid
SAM	Self-assembled Monolayer
SPFS	Surface Plasmon Enhanced Fluorescence Spectroscopy
SPR	Surface Plasmon Resonance

1. DNA detection techniques

Deoxyribonucleic acid (DNA) forms the basis of known organisms, codes for functional proteins and is responsible for growth and survival. It has various functions leading to the possibility of the use in technology such as for genetic engineering[1], catalytic activities[2] and for DNA nanotechnology[3]. Nucleic acid holds essential biological information, which can be investigated by different detection or sequencing methods. An important application is the detection of antibiotic resistance genes. The antibiotic sensitivity testing for bacteria on the genetic basis includes various methods.[4,5] This section only describes some of the most common DNA detection techniques. However, also other methods have been introduced such as microfluidic platforms[6] or loop-mediated isothermal amplification.[7] The introduced practices hold a great potential for single molecule detection systems for the investigation of individual biomolecules.

1.1. Polymerase chain reaction (PCR)

The Polymerase Chain Reaction, short PCR, was first developed in 1986 by Kary Mullis.[8] PCR is a powerful technique to amplify target genes, which was revolutionary for science. It is used for the identification and the targeting of various antibiotic resistance genes of many different pathogens.[6]

The PCR is a thermocycling reaction, which is repeated 20-40 times. The liquid reaction mixture must include a thermostable polymerase, deoxynucleotide triphosphates (dNTP), buffer with salt, specific forward and reverse primers and the analyte nucleic acid. The DNA has to be purified after the extraction of the cells. The dNTPs include dATP, dGTP, dCTP and dTTP standing for adenin, guanin, cytosin and thymin.

The PCR consists of three steps, starting with the denaturation (see Figure 1). The sample is heated up to about 94-96 °C, which makes the double-stranded DNA instable and the strands will detach due to the breakage of the hydrogen bridges between the nucleotides. Single-stranded DNA remains and anneals to the primers at a reduced temperature in the second step. The temperature has to be adopted according to the length of the primers and their composition otherwise they will not be able to attach to the DNA or they will form unspecific DNA pairs. The last step is the elongation of the DNA strands. The temperature needs to be adjusted to the optimum condition of the polymerase. Only in this case the enzyme will be

able to incorporate further dNTPs after the primer, complementary replicating the template. Those three steps are repeated until there is a high amount of DNA in the sample, which can possibly be used for agarose-gel electrophoresis.[9] This technique includes loading the sample containing DNA into a loading chamber of an agarose-gel, through which a current is applied. The negatively charged DNA strands are specifically separated according to their length. In case of short oligonucleotides, it will penetrate the gel with higher speed and travel a longer distance. Long DNA strands will have a lower velocity and therefore do not travel so far in the gel. In order to determine the size, a DNA ladder with known size and mass is added in one chamber of the gel as reference. Prior to loading, a DNA binding dye (e.g. ethidium bromide) is added to the sample to visualize the bands on the gel under UV light.[10]

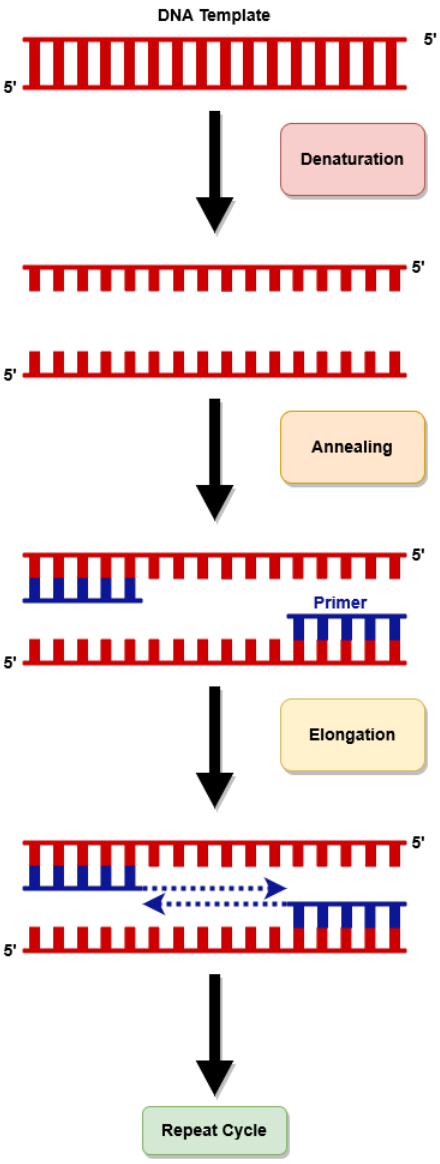

Figure 1: Schematic drawing of the PCR procedure

A more advanced version is the quantitative PCR (qPCR), in which the detection happens during the amplification process. Hence, there is no need of a gel-electrophoresis, improving the experimental time and effort. The real-time detection occurs due to the excitation of fluorescent tagged probes during the thermo-cycles.[11] Furthermore, the reverse transcription PCR (RT-PCR) uses first RNA, which is transcribed into a complementary DNA by using a certain enzyme, the reverse transcriptase. For the subsequent qPCR the produced complementary DNA strand serves as template.[12]

1.2. Rolling circle amplification (RCA)

The rolling circle amplification was developed in the 1990s as an alternative to the PCR that does not require thermal cycles. The RCA can take place at room temperature and therefore does not require a thermostable polymerase.[13] In comparison to PCR, which is an exponential replication of the target sequences, the RCA is a linear amplification process. Nowadays, the

RCA is used for various applications in different fields especially in diagnosis. It also became an important tool in nanobiotechnology (e.g. biosensors), genomics and proteomics or is used for the investigation of single molecule morphisms.[14]

As seen in Figure 2, a linear strand of DNA or RNA can be joined at the 3' and 5' terminal ends by hybridization to a highly specific template strand and subsequent ligation to form a circular padlock probe. The circular nucleic acid can then be amplified with polymerases and added deoxynucleotide triphosphates (dNTPs)[13] to a long strand of singular stranded nucleic acid with the repeating sequence from the padlock probe of 500 – 1000 times (Figure 2).[15] The process is usually conducted in solution but effort was invested to implement the RCA on the surface of a solid support.[16] The prolonged sequence can include different functionalities like sites for restriction enzymes or fluorophores. Common methods for detection are gel-electrophoresis or fluorescence-based methods.[13] The RCA reaction is a highly specific method since it depends on the hybridization of a unique DNA sequence. Its application immensely improves the sensitivity of the detection system.[14]

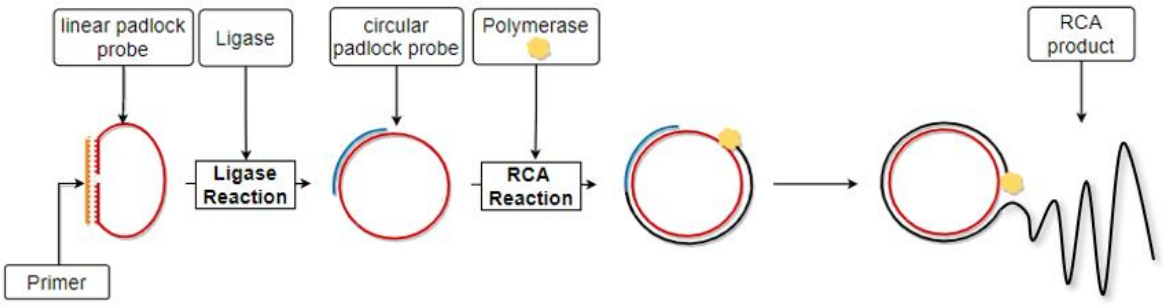

Figure 2: Schematic drawing of the RCA in solution

Multiple hybridization primers can be added to the reaction, initiating a multiple replication of the nucleic acid strand. Another possibility is the hyperbranched RCA where the RCA product operates as template for further primer sets. Moreover, the RCA product can be formed to various new padlocks after using restriction enzymes, which is called the circle-to-circle amplification.[13] The RCA reaction can also be applied to structured DNA, DNAzymes or provides a great template for DNA origami, playing an important role in synthetic biology.[14] With this approach, it is possible to bind proteins via aptamers associated to the RCA generated scaffold strand.[17] Finally, the RCA has also been used for in-situ sequencing in tissue

for investigating mutations and gene expressions as a novel next-generation sequencing method.[18]

Hatch et al. already reported about the successful implementation of the amplification of 5' terminal end anchored ssDNA strands on a solid support for the examination of polymorphisms (Figure 3).[16] This method has been advanced by combining the solid phase RCA with aptamer binding or antigen detection. A summary of solid-phase variations can be found elsewhere.[13]

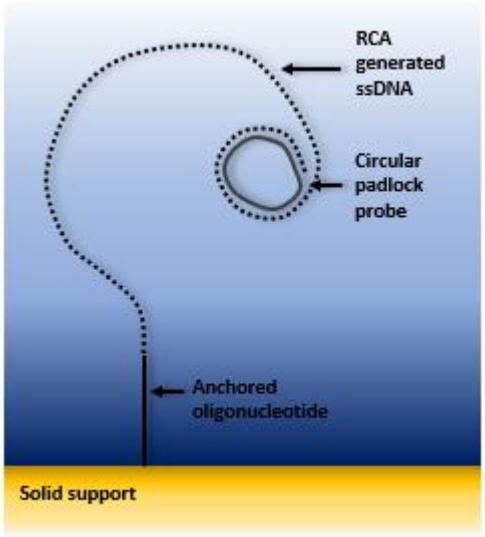

Figure 3: Representation of ssDNA generated strand by RCA on a solid support, based on figures from[16]

1.3. Whole-genome sequencing

A common approach of DNA investigation technologies is to sequence the whole genome all in one procedure. Since the whole genome can be quite long, depending on the organism, the DNA is usually fragmented prior to sequencing. Afterwards, the fragments need to be reassembled by a computer program.[19] The genetic code can be analyzed and certain genes matched with a databank. The determined DNA sequence can be thus compared to antibiotic resistance genes, which are stored in a databank.[20] This technique became an increasingly used tool in health care.[21]

Current techniques include the high-throughput method next-generation sequencing[22] or the new emerging third-generation technology of the nanopore sequencing. To decipher the whole genome has become less cost-intensive over the last years and more important

especially in health care. It allows to detect rare diseases, genetic disorders and is the basis for the decision of an appropriate therapy.[21]

There are already various commercialized instruments, which enables labs to do fast sequencing. For instance, the Ion Torrent NGS from ThermoFisher Scientific exploits the fact that a hydrogen ion is released, every time when a dNTP is incorporated.[23] This reaction occurs simultaneously a lot of times so that the pH change can be measured with a semiconductor. For third-generation sequencing, there are low-cost portable devices available with real-time sequencing by pulling the DNA through a nanopore.[24]

1.4. Microarray technology

Microarrays are an advanced technique and high throughput method to mainly detect nucleic acid, proteins or glycoms.[25] It is especially needed in food industry and diagnostics in medicine in order to detect different pathogens rapidly.[26] Jang B. Rampal defines the microarray as library where the substrate is a solid surface of a chip to which different elements can bind to.[25]

Microarrays are of clinical importance to provide a fast and cheap detection system for pathogens. It can be used for the diagnosis of various bacteria, mycobacteria and viruses. Therefore, the patient can receive the appropriate therapy earlier, which includes the prescription of the right antibiotics. Microarrays have been applied for infections in the gastrointestinal tract, respiratory tract, urinary and genital tract, bloodstream, tissue and central nervous system. [27]

The preparation of a DNA microarray starts with binding oligonucleotides to a solid support with spotted arrays. Through the interaction of the analyte with the surface and additional labelling, a signal can be produced and detected. Nucleic acids can be bound with a covalent bond to the surface or in case it is sufficient, with noncovalent interactions. For instance, a very popular linkage is the binding of streptavidin to biotin.[25] Hence, a microarray is a number of collections of biological reactions and hybridization steps, which are happening in parallel. In this way, numerous samples can be analyzed simultaneously for different analytes. If the sample contains the specific target, an optical signal is detected, indicating a positive result.[27]

1.5. Multiplexed assays

Multiplexed assay formats allow the detection of different analytes simultaneously, which is advantageous for reduction of costs, improvement of efficiency and decrease of laborious work.[28] The assay can range from very high to low multiplexed density and include various methods like second-generation sequencing, mass spectrometry, bead-based assays and quantitative PCR.[29]

There are already various systems established and commercialized like the LUMINEX xMAP® Technology. The usage of fluorescently labelled magnetic or non-magnetic beads allows the capturing of up to 500 targets for analysis. It is used for the detection of nucleic acids or numerous proteins.[30,31] An example for a commercially available multiplexed ELISA kit is the Q-Plex™ technology of QUANSYS Biosciences for human, mouse and rat marker proteins.[32] A comprehensive listing, comparison and evaluation of different ELISA systems can be found elsewhere.[33,34]

The RCA reaction can also be combined with ELISA for the detection of protein analytes. A microarray-based approach for the analysis of about 150 proteins has been established.[35] The platform uses the sandwich technique to capture the target analyte and enhances the sensor response by primer-tagged detection antibodies for the start of the RCA reaction. Common tumour marker proteins detected with ELISA have a limit of detection of 100 pg/mL, while the RCA-based approach pushes the limit to 0.1 pg/mL.[36]

A recent example for a multiplexed system, using circular DNA probes is the research of Ivan Barisic. This research group developed a microarray for the detection of 33 distinct resistance genes of ß-Lactamase for about 100 different probes.[4] The genomic DNA was digested and hybridized with the circular padlocks and amplified with the use of circle-to-circle amplification (C2CA). After ligation of the padlock, the first RCA could take place. The amplification product was labelled with oligonucleotides including an internal restriction site. Furthermore, the new padlocks are ligated, and the second RCA is initiated. The RCA product is used as template for the PCR. With the use of different fluorescence channels, the C2CA product, which was labelled with Atto532 and the Cy5-labelled PCR product could be identified by hybridizing the DNA strands to a microarray platform. In this way 75 species of human pathogens could be determined.[37] The research group improved the detection system

regarding the reduction of cost, shortening the time for the experimental procedure and improving the sensitivity over the years.[5]

1.6. Single molecule detection systems

Bioassays can be pushed towards lower sensitivity and quantification by pursuing single molecule detection. They can also be cost-intensive and laborious, which is improved through digital implementation.[38] The main principle of digital systems is the division into numerous compartments. A reaction is initiated in each chamber, giving an output, which is either positive or negative.[38,39] There are many different methods for compartmentalization, including droplet generation such as emulsification[40], soft-nanolithography[41] or pneumatic pressure[42].

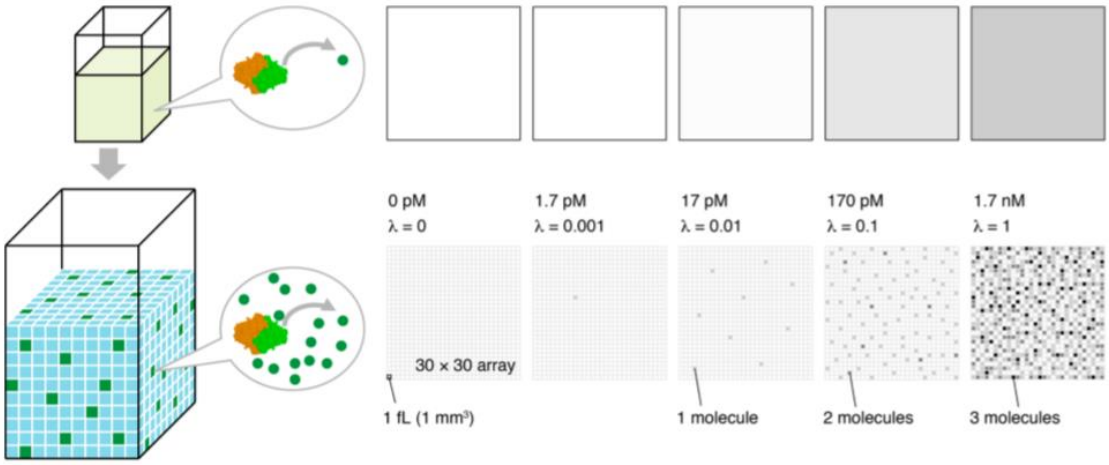

Figure 4: Representation of the principle idea of single molecule detection by compartmentalization compared to molecules in bulk solution, reprinted from[30]

The partitioning into separate reaction chambers with identical conditions, allows the counting of the positive and negative signals regardless of the intensity. It can be described with Poisson distribution. The detection of single molecules in a large volume, which are diffusion driven is rather problematic. By producing compartments where the molecules are confined, a lower limit of detection can be reached.[38]

1.6.1. Digital polymerase chain reaction (PCR)

Tachibana et al. describes a microfluidic system for simpler and faster application of PCR. Only one droplet is needed for the amplification. The liquid is repeatedly transported through capillary forces over two heating blocks. The first one has 95 °C and the second one 60 °C. Therefore, the solution rotationally enters the temperature for detaching the DNA strands,

annealing the primers and starting the replication of the templates. This happens various times, which represent the thermal cycles in a conventional PCR. Since the solution is only a thin liquid film, the heating and cooling happens rapidly, which makes the method more efficient.[43]

Furthermore, digital PCR is used for quantification of nucleic acid. Through compartmentalization the diluted sample is divided into numerous chambers. The concentration of the original sample is determined by comparing the number of chambers containing nucleic acid with the amount of chambers, which contain none. Due to advances in research the compartments already reached the scale of picolitres. This method uses the principle of real-time quantitative PCR where a signal is detected after a certain number of cycles. Form the result it is possible to calculate the concentration of the original sample. Hence, the digital system yields a better precision and sensitivity.[44]

1.6.2. Digital rolling circle amplification (RCA)

The microfluidic RCA product enrichment chip (MRE) is a common digital system for the simultaneous detection of RCA products developed by Kühnemund et al.[45] The chip consists of polydimethylsiloxane layers where the upper one has an input channel and the bottom one has an output channel. In between there is a porous membrane, which is sealed from the sides to let the solution only run through the membrane. The nucleic acid will stick to the pores and can be fluorescently imaged. The MRE chip was further developed in a pump-free version, leading to higher sensitivity outcomes and the reduction of expensive equipment. This system is widely used for different applications and provides a great platform for multiplexed methods.[46]

Literature showed the spontaneous coil-like structure of long ssDNA by local amplification, which were observed as fluorescent spots in tissue samples.[47] Another platform was developed for solid supported RCA-generated ssDNA strands by introducing two different circular templates for the detection of mutations. The detection of single-molecules by condensing the nucleic acid by specific antibodies was achieved, which were visualized with fluorescence microscopy. By this technique, it was possible to observe bright individual spots of condensed nucleic acid in cytological samples.[48]

A novel approach is the use of magnetic particles coated with streptavidin, which can bind to biotinylated capture sequence with the pre-hybridized circular padlock probe. The reactions are implemented in a magnetically controlled microfluidic system. The digital microfluidic chip provides separate reaction chambers. Therefore, the particles are moved to the RCA reaction compartment, to the digestion mix for monomerization of the RCA products and to the area with the second ligation and RCA reaction, subsequently. The C2CA-products are randomly aligned on a microscopic slide for the digital fluorescence read-out of individual bright spots. A limit of detection of 1 aM was reported for this system.[49] This system was further developed for real-time monitoring the RCA reaction by continuously measuring the fluorescence intensity.[50]

The limit of detection for other fluorescence-based RCA amplification methods was reported with 9 fM by using hyperbranched rolling circle amplification (HRCA).[51] In comparison, another method with padlock probe amplified RCA with an optomagnetic detection system reached a sensitivity of only 20 pM.[52]

1.6.3. Digital enzyme-linked immunosorbent assay (ELISA)

Enzyme-linked immunosorbent assay (ELISA) is a method to detect proteins like antibodies or antigens, which is often used in medicine for diagnosis. Firstly, a specific antibody is immobilized on a surface. Secondly, the corresponding antigen from the sample is added, which binds to the first antibody. Thirdly, a second antibody is rinsed over the surface, attaching to the antigens. The amount of antibodies bound is proportional to the sum of antigens attached. There is an enzyme associated to the second antibody, which can activate the dye after the addition of the substrate. The intensity of the color can be detected photometrically, which is proportional to the amount of target molecule.[53]

A digital version of ELISA means the reduction of the amount of substances and the improvement of sensitivity.[54] Nanoparticles or beads are coated with the capture antibody, which are binding to the target molecules. The second antibody with the attached enzyme binds to the antigen and is able to produce a fluorescence signal with the appropriate substance.[55,56] Then the beads are separated into femto-sized chambers, which can only fit a single particle.[56] Another digital ELISA system was developed where the particles with the capture antibody and the target are magnetically separated into compartments. There they

attach to tethered antibodies.[57] Single molecules can be visualized by fluorescence imaging, which allows counting of the bright spots in combination with a digital read-out.[58] An adopted method, based on single-molecule detection, has been commercialized for example by Quanterix, which is called Simoa™.[54]

1.7. Importance of antibiotic resistance

Antibiotics are antimicrobial substances, which are used for preventing and fighting bacterial infections. They act against pathogens, which can cause serious diseases and support the process of defeating the unwanted invaders in the human body. However, antibiotics can cause side-effects such as feeling sick, diarrhea or even provoking an allergic reaction. There are various groups of antibiotics but the most important are Penicillin, Cephalosporin, Aminoglycoside, Tetracycline, Macrolide and Fluoroquinolone.[59]

Pyocyanase from the supernatant of cultivated *Pseudomonas aeruginosa* was one of the first antibiotics, which was used as medicine.[60] It was investigated by Paul Ehrlich at the beginning of the twentieth century. The antibiotic Penicillin discovered by Alexander Fleming in 1928, became a life-saver during the world war II.[61] It was commercialized, and it triggered the start of the exploitation of numerous other antibiotics.

Nowadays, scientists are struggling to keep up with the emergence of further resistant bacteria even though new antibiotics or combinations of antibiotics were introduced.[62] Due to the overconsumption of antibiotics in the past, bacteria started developing resistance genes like the bacterium *Clostridium difficile*. The use of antibiotics for mild diseases is reduced nowadays because the development of antibiotic resistance is becoming a great challenge. The result is that the effectiveness of the treatment is lowered and in case of severe illnesses the medicine might not even work anymore. [63]

The World Health Organization calls antibiotic resistance “one of the biggest threats to global health, food security, and development today.“ The spread of resistant bacteria happens due to misuse in humans and in animals all over the world, causing a higher number of infections, which cannot be treated with the existing medicine. This leads to prolonged treatment and a higher death rate.[64]

1.7.1. Resistance mechanisms to antibiotics

Many gram-negative and gram-positive bacteria show resistance to antibiotics (e.g., cephalosporins, penicillins, carbapenems) due to the production of ß-Lactamases, which hydrolyse ß-lactam amide. This effect was first observed in *Staphylococcus aureus* for penicillin.

There are four relevant classes: classes A, C and D with serine as major target for hydrolysis of ß-lactam and class B, which needs metal-ions for the reaction.[65,66] Especially, the enzyme OXA-48, which belongs to class D, is clinically relevant due to the breakdown of carbapenem. It mainly appears in Enterobacteriaceae on plasmids and *Acinetobacter baumannii.* Nevertheless, the OXA class is not well understood yet and is more diverse than other classes, which implies a huge clinical challenge. Additionally, there are many complications when it comes to the detection of antibiotic resistance due to ß-lactamase. However, recent discoveries show that ß-lactamase inhibitors are the most common and effective way to defeat the ß-lactamases in resistant strains.[66]

There are several other defense mechanisms, which bacteria develop in order to reduce the effect of antibiotics. Especially gram-negative bacteria with a protective outer membrane can restrict the entry of molecules. Additionally, germs can develop pumps as an outlet for entering antibiotics or enzymes, which are able to digest the drug. However, bacteria could also either stop producing or change the substances, which are targeted by the medicine.[67]

1.7.2. Detection of antibiotic resistance

The increase in antibiotic resistance all over the world demands a counter strategy to combat with the non-treatable infections. This especially includes the prevention of misuse of antibiotics, which is only possible if the diagnosis improves. Therefore, genetic and phenotypic techniques have been developed. Since genetic susceptibility testing only provides results about resistance genes, the outcome might not necessarily match with the phenotypical testing.[68]

There are conventional methods for investigating the phenotype of bacteria. In most cases, the growth of the organism is observed. The procedure usually takes up to 48 – 72 hours until the identification can be provided. Often those techniques are too slow, leading to possible harming effects of the patient until the appropriate treatment is found.[69] The standard

methods include the microbroth technique and the disk diffusion test, which are described elsewhere.[70]

As an alternative to phenotypic susceptibility testing, antibiotic resistance genes can be investigated by genetically based techniques, as described in previous chapters 1.1 to 1.6. The most famous phylogenetic marker gene is the 16S rRNA gene coding for the rRNA incorporated in the 30S subunit of a ribosome in prokaryotes. It is mainly used for the phylogenetic reconstruction because of a small changing rate during evolution. However, biases occur due to multiple copies in the genome of the 16S rRNA gene and experimental factors. Case et al. studied 111 genomes and found 1 to 15 copies of the marker gene with 0 to 11.6% divergence within the genetic code.[71] In addition, there are various other marker genes like the rpoB or the 23S rDNA.[27]

2. Biointerfaces and molecular assembly for biosensors

The detection of biomolecules, such as nucleic acid, requires the construction of suitable biointerfaces by molecular assembly, which then serve as platforms for a recognition element. For the construction of a biosensor, additionally a transducing and a signal processing element is needed (see Figure 5). Biosensors are an important tool in the pharmaceutic industry, in the food sector, in medicine for diagnosis and for monitoring in environmental science.[72]

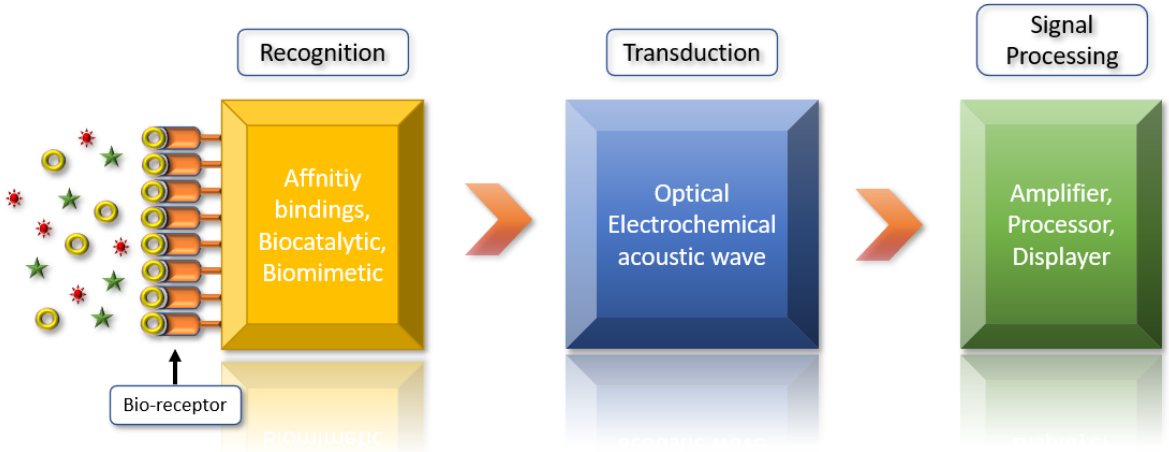

Figure 5: Composition of a biosensor with the bio-receptor binding to the target analytes as the recognition element, the transduction and the signal processing, based on figures from[73]

The binding of molecules to a biosensor needs to be controlled by using specific coating strategies. The biointerface is between the transducer and the sensing platform. It is important to make the surface antifouling to specifically control, which molecules should bind to the sensor and avoid unspecific binding. Also functional groups need to be added to capture the target molecule such as the binding of avidin to biotin (see Chapter 2.1.2).[73] A common method to attach moieties to the sensor surface is the interaction of the gold substrate to thiol-groups, which allows the self-assembly of an ordered layer (see Chapter 2.1.1).[74]

The basis of a biochemical sensor is the transduction of the signal and an element for recognition (biological recognition element BRE), which includes specific moieties to specifically interact with the analyte. Therefore, the target molecules will bind to the receptor and an equilibrium is established. This means the concentration (c) on the biosensor with the BRE (B) is constant and the same amount of analyte (A) is associated and dissociated (see Figure 6).

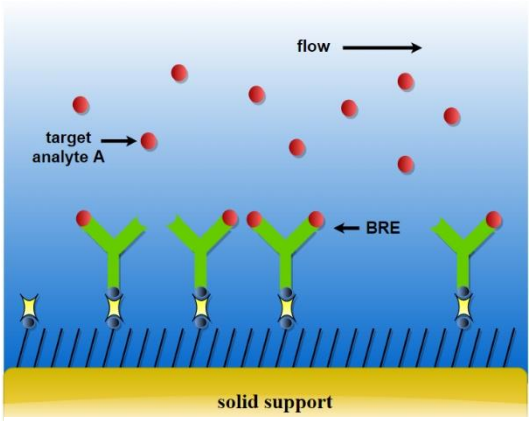

Figure 6: Schematic drawing of the function of a biorecognition element (BRE)

A high selectivity of the sensor is preferred in order to detect the desired analyte even in a complex matrix without interference.[73] The biorecognition element can be biomolecules like the highly specific antibody-antigen system. Antibodies are very complex molecules, produced as response in the immune system and usually only bind to a certain antigen. Another possibility is to use enzymes, which bind to the corresponding substrate, catalyzing an enzymatic reaction and forming a product, which can react to a fluorescent dye. In addition, nucleic acids, neuroreceptors or cells can also be used for recognition. The latter has various applications, like using microorganisms for the uptake of certain compounds. Heavy metals could be detected by monitoring the viability of the cells, including the bioluminescence, respiration and metabolism.[75] However, organelles also proved to be a useful bioreceptor. Due to the complementary sequence of DNA or RNA, oligonucleotides can be captured and fluorescently labelled. Even artificially produced membranes, molecules made by genetic engineering or molecular imprinting can function as bioreceptor.

The target molecule is adsorbed on the substrate with weak physical interactions, strong chemical bonds or a combination of different interactions. For instance, the van der Waals forces[76], which act over long distances, include interactions between dipoles and induced dipoles.[77] The electron cloud of an overall neutral molecule is fluctuating, which leads to a negative pole on the side with the higher electron density and a positive pole with the rather exposed nucleus on the other side. These interactions are non-specific and short-lived.[78]

The sensing element is sensitive to the concentration of the target analyte and a relationship between the measured signal can be established. Therefore, a transducing element is needed for translating the measured quantity into an electrical signal, which is processable, can be

optical, mass or electrochemical.[79] Optical transduction is sensing the change in frequency, amplitude or phase shift.[72] For the electrochemical transduction e.g. a platinum or carbon-based surface coated with conductive polymers can be used. Finally, the last method is to detect small changes in mass with the use of piezoelectric crystals. With an electrical signal the crystal starts vibrating in a specific frequency, which is dependent on the mass of the crystal and therefore is sensitive to the binding of molecules to the crystal.[79]

2.1. Surface architecture

2.1.1. Self-assembled molecules

Self-assembly is a spontaneous process in which disordered molecules are ordered without external influence. This is a consequence of local interactions and is often reversible, but a covalent linkage with a solid support is also possible. Amphiphilic molecules assemble automatically due to hydrophobic interactions. These compounds consist of a hydrophobic tail and a hydrophilic head group. The process can be explained with the exclusion of polar molecules like water to which the head is pointing to and the accumulation of the non-polar tails in order to escape the aqueous phase. The most popular example are the phospholipids, which are forming the membranes of cells. Amphiphiles can self-assemble into different forms, including bilayers, liposomes, micelles, which can be shaped rod-like or spherical.[73]

A common approach for functionalization of biosensors, is the use of self-assembled monolayers (SAM), see Figure 7. The most often used are n-alkyl silanes on a glass or silica substrate or alkane thiols and disulfides forming on a metal coated surface like gold or silver by relatively strong adsorption. Van der Waals interactions are the driving forces between the immobilized molecules to form an orderly packed structure.[80]

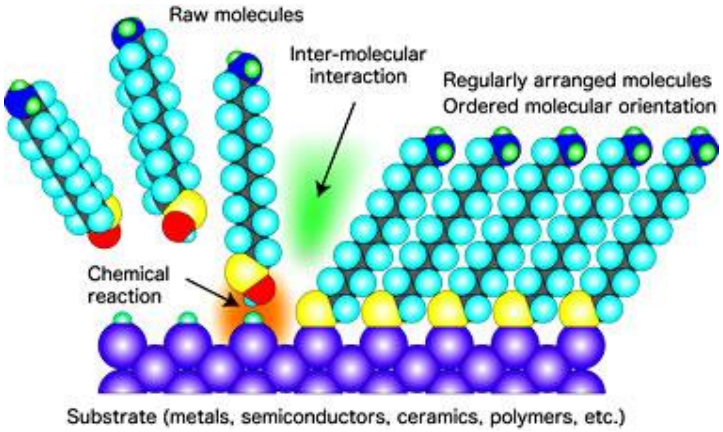

Figure 7: Schematics of the formation of a self-assembled monolayer on a substrate, reprinted from[81]

2.1.2. Affinity interactions

The use of the interaction between biotin and avidin species (avidin, streptavidin, neutravidin) is widely established for binding biological compounds to the sensor. The surface can be functionalized by biotinylated moieties, binding to avidin, which has the possibility to bind to another biotin group attached to the capture molecules.[81] The three characteristic proteins have four binding pockets for biotin and differ in the dissociation rate.[82]

The avidin-biotin system is the strongest known non-covalent interaction in biological systems. The complex is extremely stable and can withstand harsh environments. In order to disrupt the bond, conditions are needed, which would lower the functionality of the protein itself. Therefore, a new version of avidin, called captavidin, has been developed. The protein has a nitrated tyrosine in the biotin binding pocket. The result is a K_a-value of 10^9 M^{-1} at pH = 4.0 and the disruption of the bond at pH = 10. The K_a-value for avidin is 10^{15} M^{-1} and the dissociation constant $K_d = 1.3 \cdot 10^{-15}$. Garcia-Aljaro et. al. demonstrated the affinity capture of biotinylated molecules at neutral pH and the release at high pH = 10 on a biosensing platform. This system has been used for regeneration purposes of SPR sensors.[83] However, another study showed that the modified avidin bound to biotin is less stable than the unmodified version.[84]

2.1.3. Polymer brushes

The surface properties can be altered with the attachment of polymers. The wettability, the chemical reactivity on the surface, adhesion and electronic properties on the interface can be influenced. Depending on the thickness and the grafting density, different regimes can be distinguished. The conformation can be changed by altering environmental conditions.

There are two common ways to create surface brushes, which are represented in the schematic drawing from Figure 8. On the one side, there is the grafting- to approach in which the pre-synthesized polymer has a functional group attached on one end for the interaction with the surface. The polymer is covalently anchored to an oxide surface where the reaction is thermally activated. The advantage of grafting-to is the ability to characterize the grafted polymers beforehand. However, the grafting efficiency decreases with increasing molecular weight and only certain substances are applicable.[85]

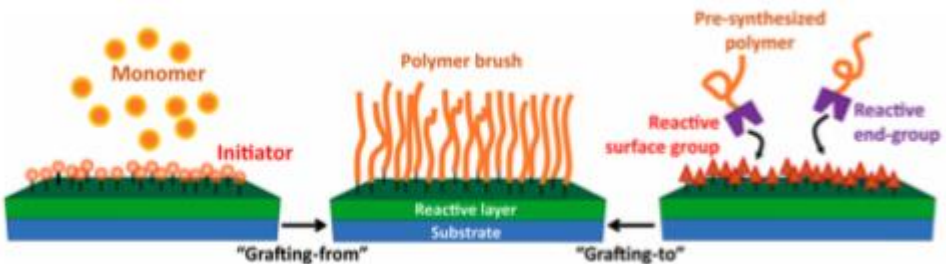

Figure 8: Representation of the grafting-from and grafting-to approach, reprinted from[86]

On the other side, the grafting-from approach is based on different polymerization techniques. The most common method is the controlled radical polymerization, which is initiated on the surface attached to an appropriate anchor with the addition of the substrate in controlled conditions. For instance, functionalized SAM on a silicon or metal substrate is a widely used approach.[85] Alternatively, methods with inimer substrates were developed[86] for achieving higher densities.[87] In addition, specific polymer brushes, which are sensitive to electron beam can be used for nano-patterning.[88]

The polymer brushes can be characterized by the surface mass density Γ and the grafting density σ. The latter defines the conformation of the brushes on the surface. The height of the polymers h scales with the degree of polymerization N and the grafting density with the exponent v, which is dependent on the type of solvent. It ranges from 0 to 1 and has the value 0.5 in a theta solvent.[85] In case of an average long-distance D between the anchor points, usually larger than two times the radius of gyration, the polymers will be in the mushroom regime. With increasing density, lower than the radius of gyration, the polymers will stretch away from the surface, forming moderate to high-density brushes.[85,89] Surfaces with lower grafting densities are more responsive to external influence due to higher flexibility.[85]

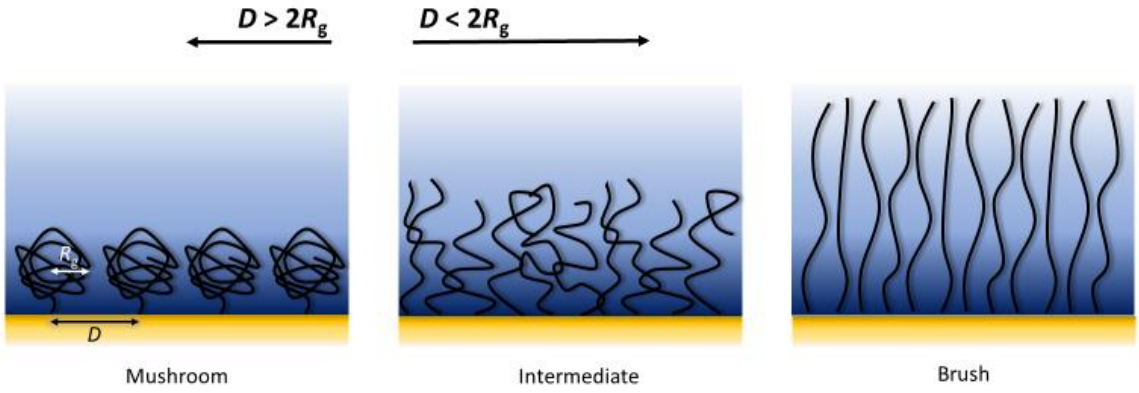

Figure 9: Representation of the effect of the grafting density on the conformation of the polymer chains

2.1.4. Structured DNA

Structured DNA is based on a smart design of DNA sequences, which self-assemble into certain geometries. The principle of the complementary base pairing between the single-stranded DNA strands is exploited. The annealing process requires a sufficient number of complementary bases, the right conditions like optimum temperature and salt concentrations. Usually there is one long DNA strand, which is brought into a specific shape by the addition of short oligonucleotides, called “staples”, which show a complementarity to at least two parts of the long strand. With this technique it is possible to form different kind of 2D (stars, smileys, etc., see Figure 10) or even 3D structures. Since the design of DNA origami is a complex process, softwares like SARSE or caDNAno were developed.[90]

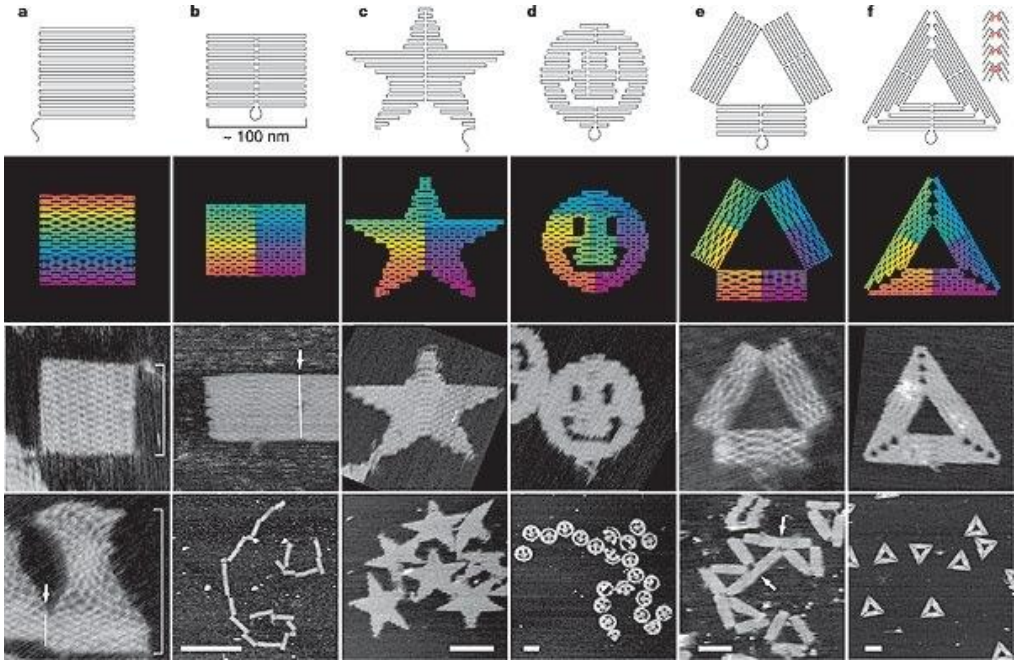

Figure 10: Various 2D DNA origami from the computational based simulated construct to images acquired by AFM, reprinted from[91]

Structured DNA can be employed on a biosensor surface for compacting long DNA strands. Literature showed the improvement of signal intensities by designing additional short oligonucleotides, which are complementary to two spatially separated sequences of the RCA product.[91] Instead of the regular RCA reaction where the product is dispersed, compaction occurs due to the staples, which pack the replicated strand into a tide coil. The DNA is fluorophore labeled and due to the local compaction, the signal intensity is enhanced by a factor of about 2. The Structure Illumination Microscope (resolution < 80 nm) was used for the read-out, which showed higher signals for the samples with the additional oligonucleotide.

2.2. Binding kinetics of affinity interactions

Molecules interacting with a surface are constantly subject to association and dissociation processes. The rate of association is expressed in the K_a constant, while the rate of dissociation is described in the K_d constant. The equilibrium of an affinity driven binding event of molecules adsorbing to a surface can be described by the Langmuir adsorption isotherm. In this case, it is assumed that the adsorption only happens as monolayer, the surface is everywhere identical and there are no interactions with adsorbed neighbor molecules.[92]

Figure 11 shows a typical measurement on a sensor surface, which do not follow the Langmuir model. At first the baseline is established with running buffer. Then a solution with molecules, which can attach to the surface is introduced. The response shows a binding kinetics and a dissociation curve when flushing again with buffer until an equilibrium is established. The difference from the new baseline to the baseline at the beginning corresponds to the amount of bound analyte. In order to bind new analytes, the surface needs to be regenerated. The regeneration solution has a different refractive index and therefore the response changes. But afterwards, in case of a successful regeneration process, the baseline should come back to the initial baseline when flushing with buffer.[93]

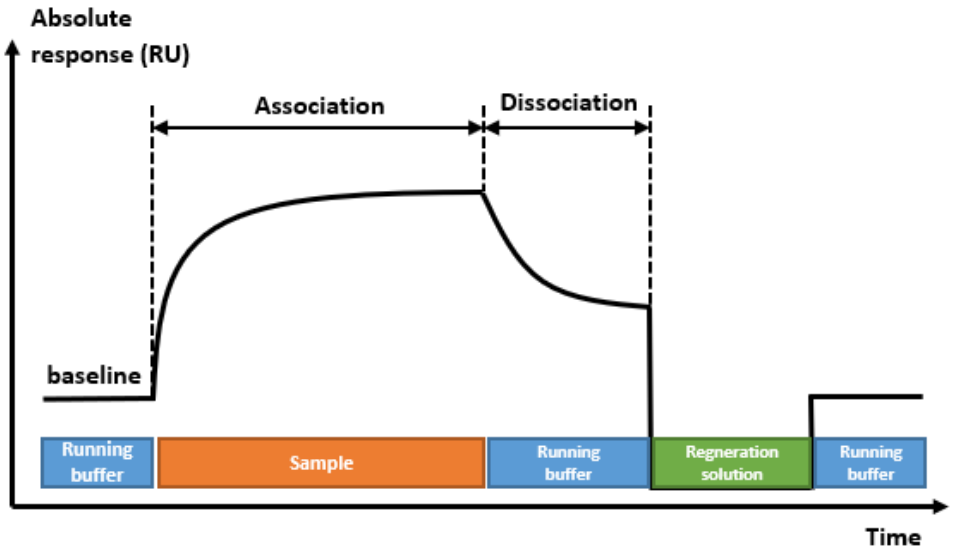

Figure 11: Binding kinetics curve of association, dissociation and regeneration events, based on figures from[94]

There are already developed systems for biosensors in order to regenerate the surface. In this process the analyte is washed off the sensor for further use of other analytes. Important in this case is not to destroy or change the sensor surface. The immobilized ligands, which should not be removed, need to stay intact and remain active.[94]

3. Plasmonic biosensors

The use of plasmonic biosensors for the quantitative analysis of biomolecules have become a common tool in research. This thesis uses surface plasmon resonance spectroscopy (SPR) and surface plasmon enhanced fluorescence spectroscopy (SPFS) for the investigation of biopolymer behavior after capturing of DNA analytes in bulk solution. The following chapter should give an overview of the physical background and a description of the applied techniques.

3.1. Optical probing of interphases

3.1.1. Electromagnetic wave

Light is a form of electromagnetic wave, which can be described as an oscillating field consisting of an electric and a magnetic part (Figure 12). The low intensity of light can be treated as flux of photons with a quantized energy *E*, which can be expressed with Plank's constant *h* and the frequency $\nu = c / \lambda$.

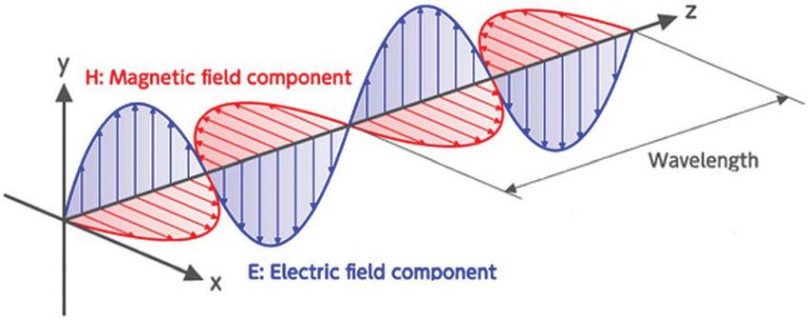

Figure 12: Schematic drawing of an electromagnetic wave, reprinted from[95]

$$E = h * \nu \qquad (Eq. 1)$$

Electromagnetic waves are often classified, depending on the wavelength λ. The longer λ, the lower is the energy *E* of the photon. At short wavelengths of the electromagnetic spectrum, λ < 10 pm, are the gamma-waves with the highest energy. The ultra-violet light (UV) is located between 10 nm to 400 nm, followed by the visible light in the region 400 nm to 650 nm. Afterwards is the infrared region. The longest wavelengths λ > 1 m are radio waves.[95]

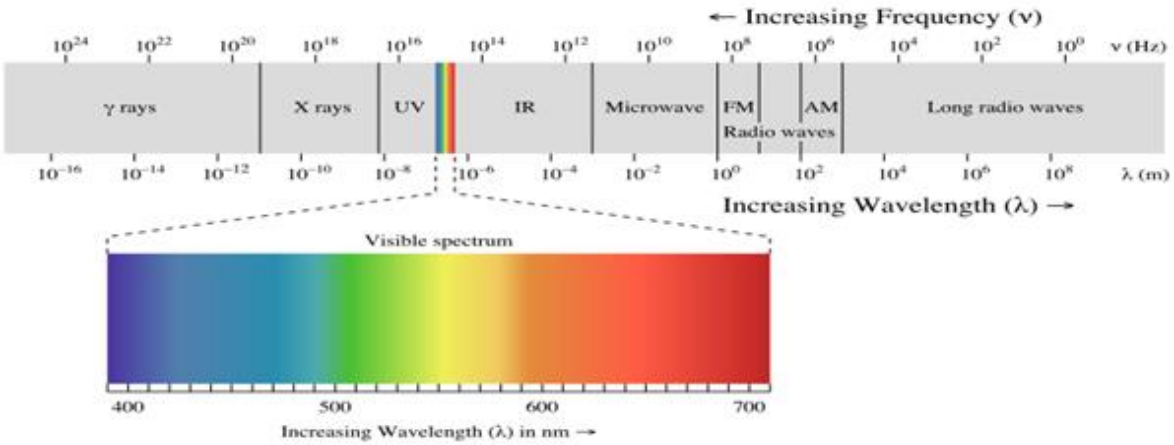

Figure 13: Electromagnetic spectrum, reprinted from[96]

3.1.2. Propagation of light at dielectric interfaces

The optical density of the medium, through which the wave is propagating, can be described by the refractive index *n*. An electromagnetic wave travels in vacuum with the speed of light *c*. The refractive index can be described as the ratio of the speed in vacuum to the speed v, which the wave has while travelling through the medium.[96] In air *n* has the value 1.0003 and in water 1.330, which takes into account the coupling of the field with matter polarizability.

$$n = \frac{c}{v} \qquad (Eq.\,2)$$

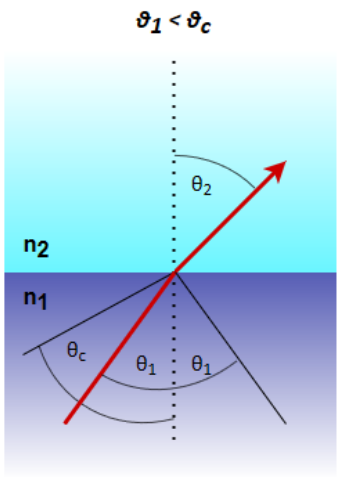

Figure 14: Refracted beam

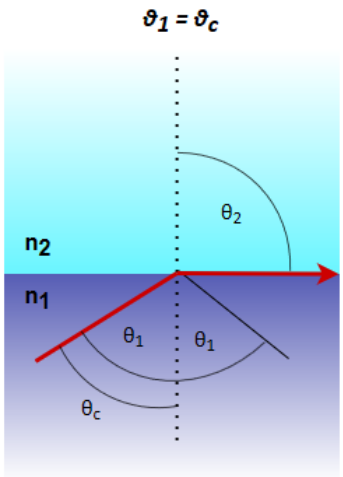

Figure 15: Propagating beam along the interface

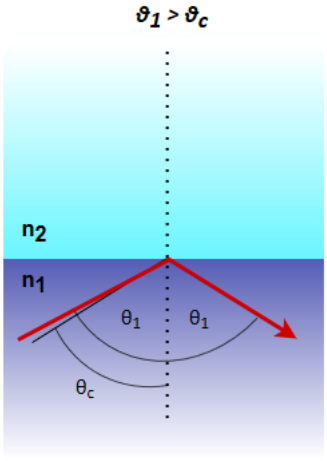

Figure 16: Total internal reflection of beam

The refractive index affects the propagation of a beam when entering from a medium with n_1 into another medium with n_2 and it depends on the wavelength. Therefore, spectrum of

polychromatic light can be dispersed due to the different angle of refraction at different wavelengths.[97]

Let us assume a light beam incident at the interface of two materials with different reflective indices with an angle θ_i, then a proportion of the beam energy is transmitted with an angle θ_t, while the other part is reflected at the same angle $\theta_i = \theta_r$ as the incident light beam. Snell's law of reflection describes this phenomenon ($Eq.3$). At the critical angle, the transmitted beam travels along the interface. If the angle exceeds the critical angle the entire beam is reflected as the transmitted beam vanishes. Total internal reflection occurs at higher angles than the critical angle θ_c. For instance, this phenomenon is applied in optical fibers. The beam is totally reflected in a glass fiber for numerous times and can be transported over huge distances. It is used in the telecommunication sector.[98]

$$Snell's\ Law: n_1 \sin\theta_1 = n_2 \sin\theta_2 \qquad (Eq.3)$$

The total internal reflection in a prism can be described with the formula, which gives the critical angle θ_c ($Eq.4$). The light is travelling through the surrounding medium with refractive index n_2, enters the prism with higher refractive index n_1 and is entirely reflected if the critical angle θ_c is exceeded. The refractive index of the prism is about 1.9 for LasFN9[99] and of a buffer solution about 1.33.[100]

$$\theta_c = \arcsin(\frac{n_2}{n_1}) \qquad (Eq.4)$$

3.1.3. Fluorescence

There are transitions possible between the electronic states, caused by UV or visible light. This process is called absorbance, which means that a specific portion of energy of an electromagnetic wave is matching with the energy level of an electron and taking up the incoming energy portion. The electron will be in an excited state S_1 and will emit the energy (hv) in order to return to the ground state S_0.[95]

A certain form of absorption is luminescence, which is a spontaneous process of emission of light in the range of UV-VIS to infrared radiation.[101] Fluorescence is a special case of luminescence. By exciting the analyte, energy is absorbed, and a valence electron is moved from the ground state to an excited state with the conserved electron spin state. When the electron returns to the initial energy state, the emitted radiation has less energy and a higher

wavelength than the absorbed wave due to internal conversion to the level S_1', known as Stokes shift (Figure 17).[102] The radiationless deactivation can also occur by collision with other molecules e.g. from the solvent or the dissipation of heat due to vibrational relaxation.[103]

The interval after the excited state until the emission to the ground state is called the fluorescence lifetime and ranges from 10^{-9} – 10^{-12} seconds.[102] The relaxation from state S_1 to S_1' takes about 10^{-14} – 10^{-11} seconds.[104] The quantum yield is a characteristic quantity to describe the fluorescence process. It can be determined by the number of emitted photons divided by the number of absorbed photons.[102]

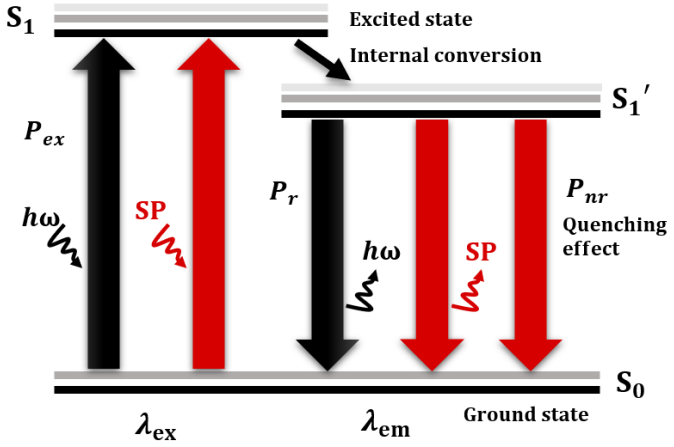

Figure 17: Jablonski diagram based on figures from[104]

There are two main effects, which influence the emission of photons from fluorophores. On the one hand, there is the quenching effect. This process is reversible and describes the suppressing of emitting radiation by the presence of specific molecules by transferring the energy to an acceptor. These compounds can either be metals, halogens or salts. This effect occurs in the vicinity of about 10 to 15 nm of the effector molecule. On the other side, photobleaching is irreversible and happens due to the limited amount of excitation, which ends in the damage of the dye. The amount of absorption and emission cycles, which a dye can go through, is depending on the molecular structure.[104,105]

3.1.4. Surface plasmons

Density of free electrons on a metal surface can couple with electromagnetic field, which leads to their collective oscillation along the surface. An evanescent field decaying perpendicular to the metal surface is then formed at the interface of a metal and a dielectric, see Figure 18.[106]

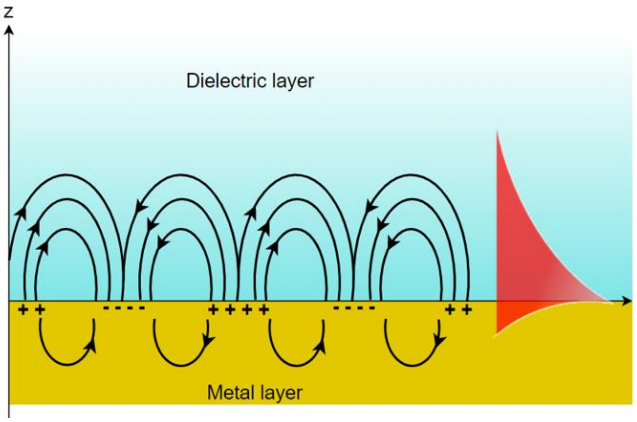

Figure 18: Schematic drawing of surface plasmons on a surface

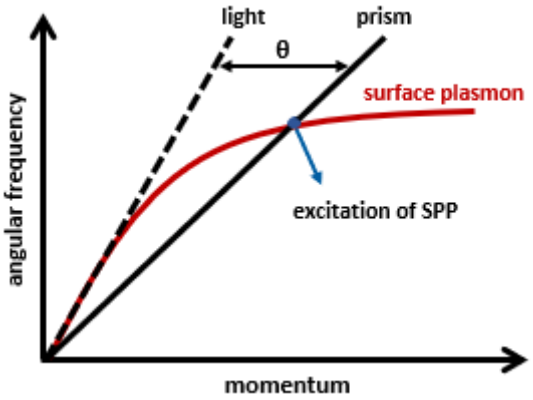

Figure 19: Dispersion relation of surface plasmons for prism coupler in Kretschmann configuration; based on figure from[107]

The electric field is decaying slower in the dielectric medium than in the metal. In order to optically excite these waves called surface plasmons polaritons (SPP), a coupling device (prism, waveguide coupler or grating coupler) is needed due to the mismatch of the wavevectors of light travelling in the dielectric and the surface plasmons (see Figure 19). Hence, a photon approaching the surface from the far field is not able to excite a plasmon. The most common coupler utilizes the glass prism for attenuated total reflection. The incident beam enters the medium with a high refractive index n_p at an angle for which it is totally reflected at the interface to the metal layer, that is attached to the prism. At a certain angle, surface plasmons are generated, which are propagating along the interface between the metal and the outer dielectric.[107] The electromagnetic wave is confined on the surface by surface plasmons in both directions from the metal surface. Usually, a thin glass slide is coated either with silver or gold layer through evaporation in vacuum for a total layer thickness of about 50 nm. The incident beam is p-polarized.[100]

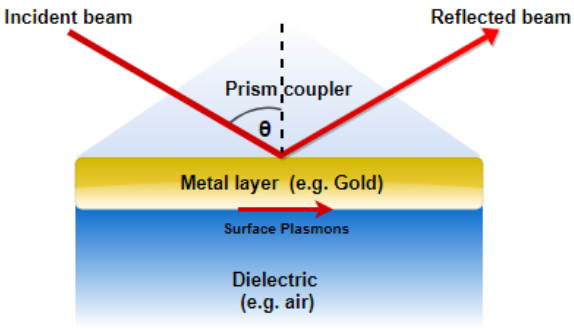

Figure 20: Prism coupler in Kretschmann configuration

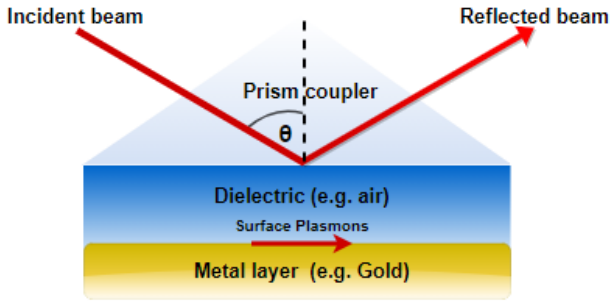

Figure 21: Prism coupler in Otto configuration

There are two configurations applicable when using a prism, which are named according to their inventors. On the one side, if the metal layer is directly attached to the glass as demonstrated in Figure 20, this mode is called Kretschmann-Raether method[108]. On the other side, the dielectric can be between the metal film and the prism, called the Otto configuration[109] (see Figure 21). However, this gap is not easy to control and therefore the Kretschmann-Raether method is mostly applied.[110]

A waveguide coupler represents another possible approach to optical exciting of surface plasmons on the interface of a metal layer and a dielectric, represented in Figure 22. A portion of the electromagnetic field is also guided through a layer with low refractive index. The waveguiding mode has the substrate (low refractive index) on the one side and the metal layer on the other, side where the surface plasmons are excited. In order to achieve the coupling, the propagation constants for the guided wave and the surface plasmons need to be equal.

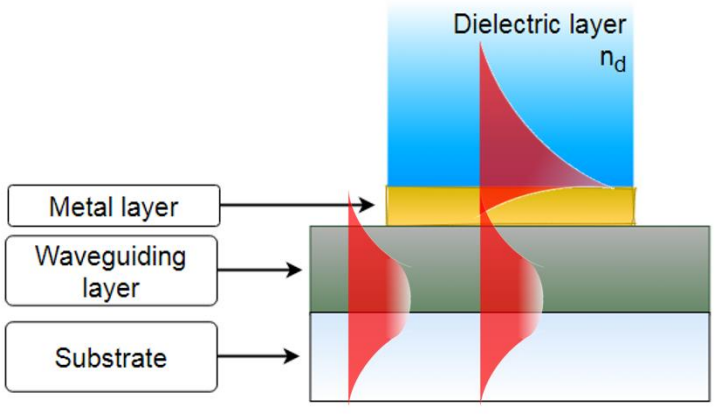

Figure 22: Schematic drawing of a waveguide coupler

To conclude with, an additional option to fulfill the coupling conditions is to use a metal with a grating structure on the surface (see Figure 23). The light enters through the dielectric medium and is diffracted at the grating of the metal layer. Surface plasmons are excited in case of the propagation constant being equal to the parallel momentum of the diffracted light enhanced by grating momentum.[107,111]

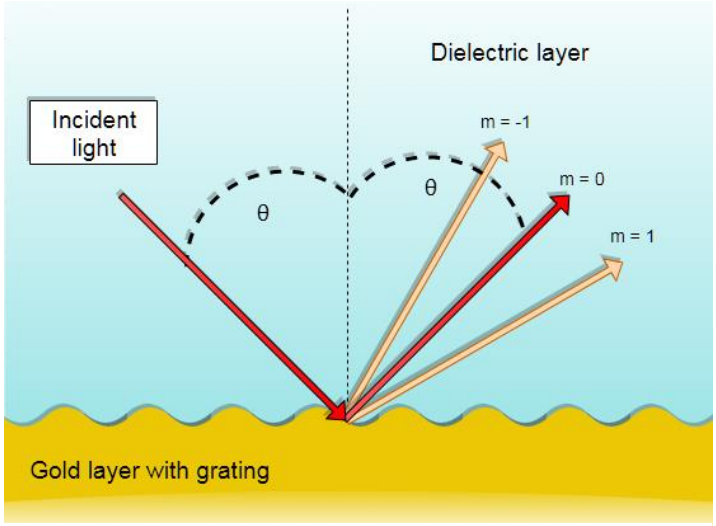

Figure 23: Grating coupler with incident light and reflected beams in diffraction order m

3.2. Surface plasmon resonance sensors (SPR)

Surface Plasmon Resonance was observed by Wood in 1902 for the first time. He used a diffraction grating and discovered black bands in the reflected pattern. However, Lord Rayleigh was one of the scientists who was able to explain the origin of the dark lines. Nevertheless, surface plasmons were only fully explained in 1968 by Andreas Otto and at the same time by Erwin Kretschmann.[112]

SPR sensors consists of a thin metal layer where surface plasmons are induced. The change in refractive index of the interfacial layer is measured, which alters according to the coupling of molecules to the surface. The angle of the incident light can be modulated and used as a sensor output, yielding spectra with a dip indicating the highest resonance for surface plasmons at a specific angle. Apart from that the angle can also be held constant and the intensity of light is used as sensor output. The applicable light is transvers magnetically polarized, called TM-mode.[107]

Below the critical angle, one portion of the light, which comes from a laser beam is transmitted, while the rest is reflected due to the noble metal layer. Hence, a lower reflectivity

is detected. At the critical angle the reflectivity shows a steep increase, which is dependent on the properties of the medium.[113]

In the reflectivity scan (see Figure 24) the intensity of the incident light is detected at different angles. At a specific angle, surface plasmons are initiated, showing a minimum of intensity at the resonance angle where most of the light intensity is trapped on the surface. The resonance angle is dependent on the refractive index of the interfacial layer and will be shifted to higher angles if the refractive index changes. Those alterations can be due to the binding of molecules to the surface.[112] Alternatively, not only the angle of incidence θ can be interrogated, but also the wavelength λ, the phase shift or the intensity can be monitored instead.[114]

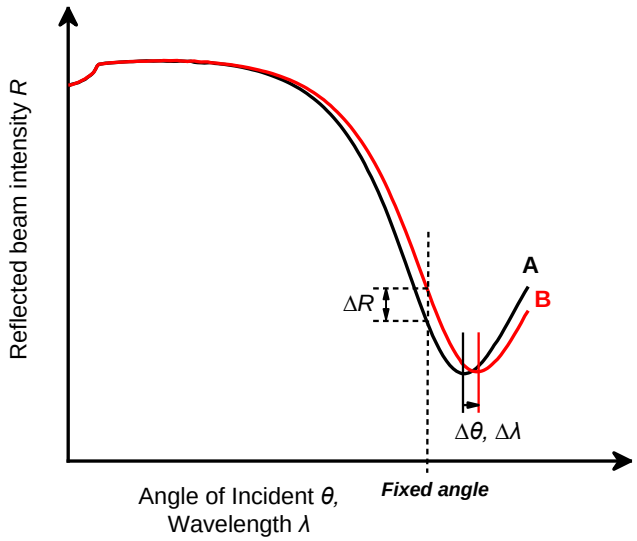

Figure 24: Shift of the reflectivity curve due to binding of mass to the sensor surface, measured by SPR

By determining the shift of the resonance angle in the angular reflectivity curve $R(\theta)$, the layer thickness d_p can be approximated and the refractive index n_p can be adjusted for thick layers (> 1 µm) with an additional feature appearing at the critical angle (see Chapter 3.2.1). From these values the surface mass density Γ[115] is calculated with the corresponding refractive indices of the layer n_p and the buffer n_{buffer} according to the following equation:

$$\Gamma = d_p \left(n_p - n_{buffer}\right) \frac{dc}{dn} \qquad (Eq. 5)$$

For DNA the value for the change in refractive index depending on the concentration $\frac{dc}{dn}$ is 0.17 mm³/mg.[116] The attached layer can be additionally characterized by the grafting density

σ in nmol/mm², which is determined from the molar mass *MW* and the surface mass density Γ in ng/mm²:

$$\sigma = \frac{\Gamma}{MW} \qquad (Eq. 6)$$

Real-time measurements *R*(*t*) are done for following binding kinetics during an experiment. The angle of incidence θ, which is chosen at the resonance edge with the highest slope, and the wavelength λ are set constant and the intensity is measured depending on the refractive index change by altering the surrounding media and the attachment of biomolecules. First, the sensor surface needs to be flushed with buffer for establishing the baseline. Then the analyte is flowed over the surface to attach to the specific capture moieties. During this process the association curve can be monitored. By flushing with buffer again, the baseline before and after the binding of the target molecules can be compared and a prediction can be made about the amount of bound analyte.

The association and dissociation constant of binding events can be determined, indicating the strength of the attachment.[112] In addition, the binding molecules can be labelled with fluorophores, which can be monitored with SPFS (see also Chapter 3.3). With this method it is possible to detect analytes with a low molecular mass, which is not able to produce a shift in the reflectivity measurement.[113]

3.2.1. Optical waveguide

A waveguide is the transmission of light through a densely packed medium. The common example is the use of a bundle of optical fibers, which are long and thin glass or silica fibers. The beam enters the fiber with an angle higher than the critical angle. The light is internally totally reflected each time it hits the fiber wall and guided to the exit of the fiber. The fibers are in micrometer-range in thickness. Total internal reflection occurs at the interface of the silica or glass core with a high refractive index to the surrounding cladding material with lower refractive index. The main application for optical fibers in medicine are medical devices like endoscopy or measuring of blood oxygen.[117]

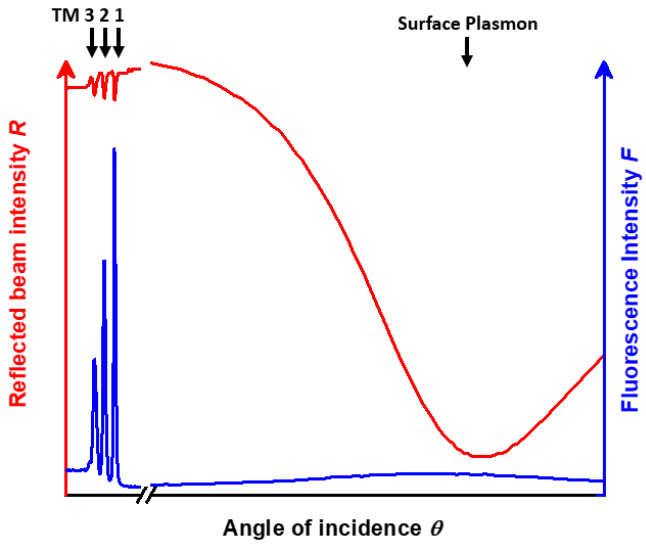

Figure 25: Optical waveguides in the reflectivity and fluorescence curve, measured by SPR and SPFS

There are different sensing methods based on optical waveguides, which are guided in a polymer layer, which is based on the resonator of Charles Fabry und Alfred Pérot, called the Fabry-Pérot resonator. This method can be applied to the Surface Plasmon Resonance Spectroscopy. Waveguides are produced in the polymer layer, acting as resonator with thickness of few micrometers on top of a 50 nm gold layer. As seen in the principle spectrum in Figure 25, there are peaks in the TM mode indicating the waveguides, which depend on the thickness and the refractive index of the gold and the polymer layer.[118]

The optical waveguide spectroscopy (OWS) is a useful technique to investigate molecules in thin layers on a solid support. The absorption of the analyte changes the refractive index of the layer.[119] The adsorbed layer is able to act as a waveguide due to multiple total internal reflection. Combinations of OWS with Raman spectroscopy,[120] attenuated internal spectroscopy[121] and SPR[122] were reported. A detailed description of the different methods of OWS can be found elsewhere.[123]

3.3. Surface plasmon enhanced fluorescence spectroscopy (SPFS)

The SPR measurement has limitations. For instance, the metal surface can be covered with a few nanometers thick layer of streptavidin whose molecular weight is high enough to produce a detectable shift in the angular scan. However, in case of binding of molecules with a low molecular mass or only a low surface coverage is achieved, the detection limit is reached. In order to overcome these sensitivity limitations, fluorophores are used in connection with SPR.

The fluorophores are conjugated to molecules, which are able to affinity bind to the sensing surface by which they are placed within the evanescent field.[113] The electromagnetic field around fluorophores is enhanced by surface plasmons leading to higher excitation rate of fluorescence. This principle is exploited in SPFS.[124] The transition rate of the fluorophore between the ground level and the excited state is altered.[125] The highest field enhancement is basically at the point where most of the incident light is propagating as surface plasmons at the interface, which is at the minimum of the reflectivity (see Figure 26). In fact, due to resonance conditions, the maximum of the fluorescence is slightly shifted to lower angles in comparison to the dip of the reflectivity curve. Furthermore, the intensity of the fluorescence light is dependent on the distance of the dye to the surface. The reason is the influence of the electron gas of the metal on the orbital structure of the chromophores, which has an increasing effect on the life-time and the intensity with approaching dyes.[113] However, at very short distances, below 15 nm, quenching occurs and the energy dissipates as heat on the metal surface. This happens due to the Förster energy transfer[125] where the donor chromophore non-radiatively transfers energy to an acceptor (metal) by dipole-dipole coupling. This is the basis for Förster resonance energy transfer (FRET).[126]

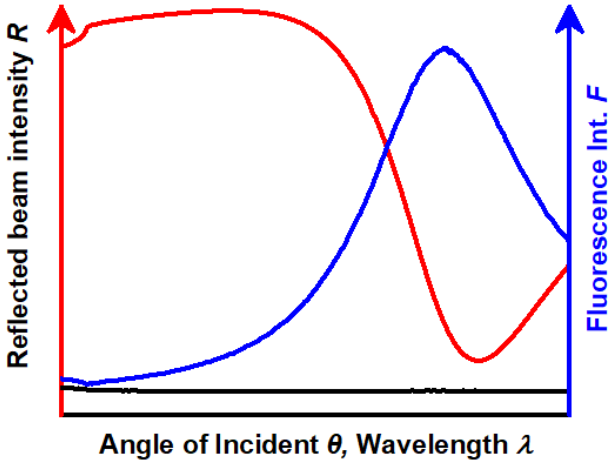

Figure 26: SPR reflectivity curve in red and corresponding fluorescence intensity in blue, which is most enhanced close to the resonance angle

A common dye, which is especially used in biological samples, for instance for coloring different parts of cells, is the Cy5 fluorophore. It has the excitation maximum at λ_{ex} = 649 nm and the emission maximum at λ_{em} = 666 nm. The far-red fluorescence region is advantageous due to the low autofluorescence. This also applies to Alexa Fluor 647.[127] The detection of fluorescence light takes place in the far field on the other side of the cell, which is illustrated in the schematic representation of the experimental set-up in Chapter 5.2 (see Figure 28).

4. Aim of thesis

The currently established principles for single molecule detection formats dominantly rely on the confining of single target molecules into a series of small compartments, where their presence following Poisson's statistics is detected with the use of fluorescence spectroscopy and enzymatic amplification. The enzymatic amplification is implemented in the bulk solution and typically the presence of target analyte in the miniature reaction compartment is associated with conversion of a dark substrate to highly fluorescent species.[15] Alternative approaches are investigated based on the capture of target analyte at a solid surface in conjunction with other optical enhancement and enzymatic strategies that are inherently confined in the vicinity to the target analyte. This avenue holds potential to provide new analytical tools with higher throughput enabled by the multiplexing and potentially simpler and faster assay format.

Additionally, the conjunction of surface plasmon-enhanced fluorescence spectroscopy (PEF) and rolling circle amplification (RCA) allows for sensitive detection of generated long strands of DNA with repeating sequence of the padlock probe, which are tethered to a metallic sensor surface and can be labelled with multiple fluorescence dyes.

This thesis concerns RCA on the solid metallic surface with gradually decreasing tethering density of generated ssDNA strands. It aims at the investigation of possible means for their efficient manipulation for the sensitive probing with the use of evanescent wave optical readout. The growth of ssDNA on a thiol-SAM-modified gold sensor surface is implemented as indicated in Figure 27 and the long tethered ssDNA strands are fluorophore labelled and detected with the use of combination of, PEF, SPR, and fluorescence microscopy. In particular, the following aspects are addressed:

- Changes in the conformation of the long ssDNA chains that are grafted with decreasing surface density.
- Response of the ssDNA chains to variation in bulk environment and affinity interaction with short oligonucleotides that can serve as staples or tether the chains to solid surface at multiple points.

- Utilization of RCA on a metallic surface for sensitive plasmonic biosensor and possible transition from the readout of ensemble of target molecules to detection of individual captured molecules for establishing the digital readout format.

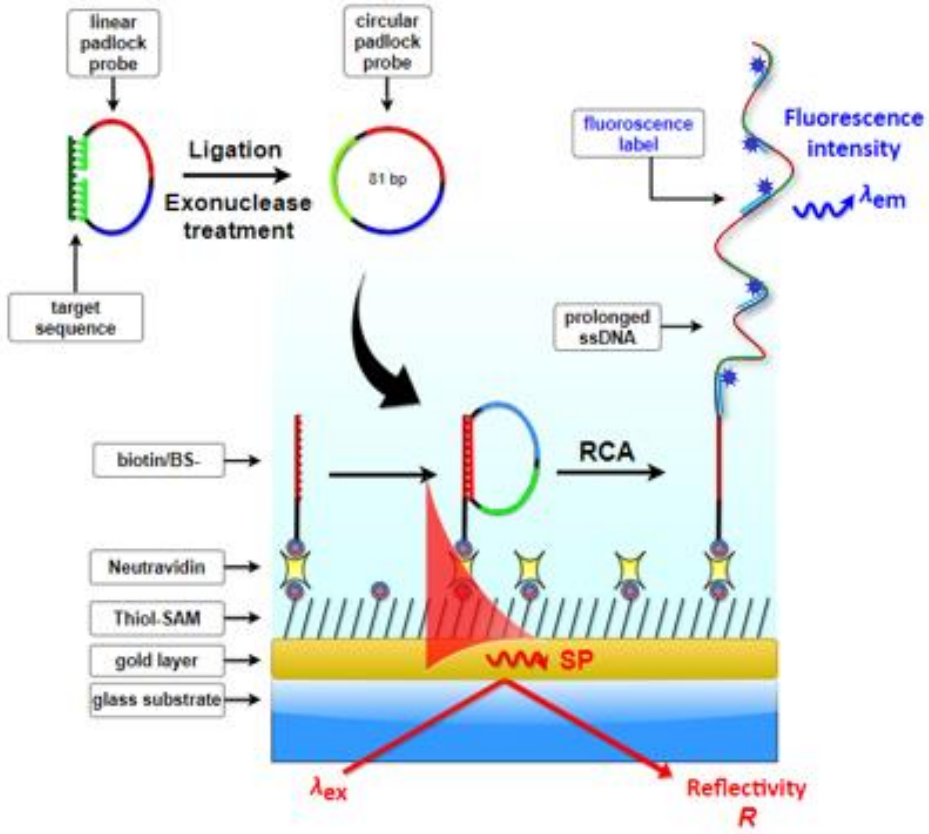

Figure 27: Schematics of the RCA implementation on a solid metallic surface that is probed by a combined SPR and PEF methods

5. Materials and Methods

5.1. Materials

The OEG-thiols (OEG-OH, HS-$(CH2)_{11}$-EG_6-OH, prod. No. TH 001-m11.n6); OEG-biotin, HS-$(CH2)_{11}$-EG_6-biotin, prod. No. TH 004-m11.n6) were obtained from ProChimia Surfaces. From VWR are the phosphate buffered saline (PBS, pH=7.4, cat. No. E504), nuclease-free water (NFW, cat. No. E476), Tween 20 (cat. No. 437082Q) and 99.9 % pure ethanol (cat. No. 1.11727). Calcium chloride ($CaCl_2$, cat. No. C1016) and sucrose (cat. No. S7903) were purchased from Sigma Aldrich. Bovine serum albumin (BSA, cat. No. B9000S) was obtained from New England Biolabs.

Ampligase DNA ligase (cat. No. A3210K) were purchase from Epicentre. Exonuclease I (Exo I, cat. No. EN0581) and FastAP Thermosensitive Alkaline Phosphatase (cat. No. EF0651), phi29 DNA polymerase (ϕ-29 Pol, cat. No. EP0094), deoxy nucleoside triphosphates (dNTPs, cat. No. R0192) and neutravidin (cat. No. 31050) were from Thermo Scientific™.

The table summarizes the DNA sequences, which were obtained from Integrated DNA Technologies. The DNA products were stored at 4°C after being dissolved in nuclease-free water.

Table 1: DNA sequences and description in schemes of used oligonucleotide probes

Probe	description in schemes (5' - 3')	sequence (5' - 3')
Padlock Probe (PLP)	**TS+/C2CA+/BS+/TS+**	/5Phos/TG TGA TAC AGC TTT CTT GCGC GTG TAT GCA GCT CCT CGA GTA GC C GCA GTT CGC GCC GCA G GG CCG ATA CGT GTA ACT TAT
Primer sequence	**TS-**	/5Phos/AAG AAA GCT GTA TCA CAA TAA GTT ACA CGT ATC GG
Primer sequence	biotin/20T/**TS-**	/5Biosg/TTTTTTTTTTTTTTTTTTT AAG AAA GCT GTA TCA CAA TAA GTT ACA CGT ATC GG
Capture sequence	biotin/20T/BS-	/5Biosg/TTTTTTTTTTTTTTTTTTTTC TGC GGC GCG AAC TGC G
Tethering sequence	biotin/20T/**11TS+**/ddC	/5Biosg/TTT TTT TTT TTT TTT TTT TTC CG ATA CGT GT /3ddC/-3'
Control sequence	biotin/20T/random	/5Biosg/TTTTTTTTTTTTTTTTTTTC GAC TAC GAC TAC GAC TAC
Labelling sequence	5'-Cy5/**C2CA+**	/5Cy5/GTG TAT GCA GCT CCT CGA GTA
Labelling sequence	5'-Cy5/**C2CA-**	/5Cy5/TAC TCG AGG AGC TGC ATA CAC
Cy5/BA accordion	Cy5/BA+	/5Cy5/TT ATT GTG ATA CAG CT GGC CGA TAC GTG TAA C-3
Cy5/DC accordion	Cy5/DC+	/5Cy5/CAG CTC CTC GAG TAG CT TCT TGC GCG TGT ATG-3
Cy5/DCBA accordion	Cy5/DCBA+	/5Cy5/CAG CTC CTC GAG TAG CT TCT TGC GCG TGT ATG TT ATT GTG ATA CAG CT GGC CGA TAC GTG TAA C-3

5.2. Optical set-up

The home-built optical set-up for the SPR measurements is built in Kretschmann configuration. The beam of the Helium-Neon laser (Lasos, LGK 7628, 350 µW/cm², λ_{ex} = 632.8 nm) is directed through the bandpass filter (LBPF, Thorlabs, FL632.8-10), the chopper (Signal Recovery, Model 197, frequency f = 933 Hz) and the polarizer. The monochromatic beam enters a prism made of LASF9 glass (Schott, n = 1.850), which is fixed on a rotation stage and is reflected by the sensor chip. In order to optically match the sensor chip with the prism, an immersion oil (Cargille Laboratories; n = 1.7000, cat. No.1812) with high refractive index is used. For the detection of the beam, a photodiode in combination with a lock-in amplifier (EG&G, Model 5210) is used. The photomultiplier (Hamamatsu, H6240-01) and photon counter (Agilent, 53131A, f = 225 Mhz) collected the emitted fluorescence light (λ_{em} = 670 nm) after passing through two lenses (Thorlabs, focal length f = 50 mm, numerical aperture of NA = 0.2, LB1471), a laser notch filter (LNF, Melles Griot, XNF-632.8-25.0M CVI) and two bandpass filters (FBPF, Thorlabs, FB670-10 and Andover Corporation Optical Filter, 670FS10-25). The reflected beam intensity R in % and the fluorescence intensity F in counts per seconds (cps) were displayed by the software Wasplas (Max Planck Institute for Polymer Research in Mainz, Germany) with respect to time $R(t)$ or the angle of incidence $R(\theta)$.

The flow-cell with a volume of 10 µL is a silica glass (Sico Technology) with two drilled holes for the inlet and outlet and sealed with a PDMS gasket. The utilized Tygon tubing had either the inner diameter of I_d = 0.25 mm or I_d = 0.60 mm. The solutions were transported with a peristaltic pump.

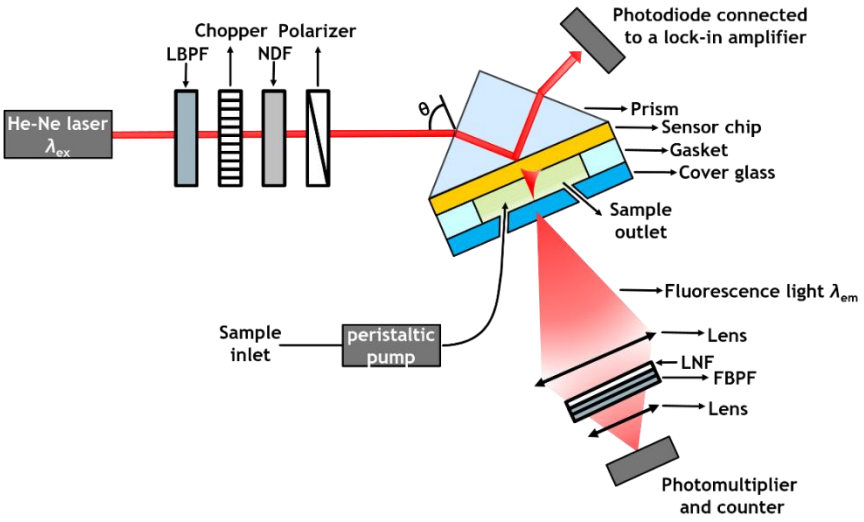

Figure 28: Schematic representation of the experimental set-up, based on figures from[128,129]

5.3. Preparation of biosensor chips

Microscope slides (BK7 or LasF9 glass) were cut into pieces of about 25x20 mm with a diamond cutter. The cleaning procedure was the piranha cleaning with 25 % of hydrogen peroxide and 75 % of sulfuric acid for 1 hour. Afterwards the slides were washed with ethanol and sonicated with 1 % Hellmanex (Hellma Optics) in MilliQ water ($R \geq 18.2$ MΩ/cm²), solely MilliQ water and subsequently with ethanol for 15 minutes. The glass substrates, dried with pressured air, were mounted onto a sample holder and loaded into the evaporator (HHV Ltd, Auto306 Lab Coater). Vacuum (lower than 10^{-6} mbar) was established by a vacuum pump and liquid nitrogen. First, chromium (MaTeck, cat. No. 009540) was thermally evaporated until a thickness of 2 nm was reached. Then a gold layer (MaTeck, cat. No. 900426) with thickness of 50 nm was deposited in the same vacuum.

For the formation of SAMs the gold chips were incubated in an ethanol solution containing a mixture of OEG-thiols (of OEG-OH and OEG-biotin) over night. The slides are rinsed with pure ethanol and stored in the dark under argon in order to prevent oxidation.

5.4. Ex-situ padlock probe preparation

For circularizing the linear padlock probe a ligation reaction was performed. Therefore, 15 µL ampligase (lucigen – 5 U/µL), 185 µL NFW-BSA (0.2 mg/mL), 25 µL ligase buffer (20 mM Tris-HCl, 25 mM KCl, 10 mM $MgCl_2$, 0.5 mM NAD, and 0.01% Triton® X-100), 15 µL padlock probe (3 µM in NFW) and 10 µL of the target sequence (2 µM in NFW) were mixed. The total volume was 250 µL. The solution was incubated on the shaker at 50°C for one hour and afterwards the enzyme was inactivated at 85°C for 15 minutes.

For the exonuclease treatment 217.5 µL NFW, 25 µL exonuclease buffer (67 mM glycine-KOH, 6.7 mM $MgCl_2$, 1 mM DTT), 2.5 µL Exonuclease I (20 U/µL) and 5 µL Alkaline Phosphatase (1 U/µL) were added to the mixture after the ligase reaction. The total volume was 500 µL. The solution was incubated on the shaker at 37°C for 15 minutes and afterwards at 85°C for 15 minutes. In between the enzymatic steps, the solution was always immediately chilled on ice.

5.5. On-chip kinetic measurements

Before the start of the kinetic measurements $R(t)$, an angular reflectivity scan $R(\theta)$ of the chip in contact with air (θ = 20°-30°) was conducted. Afterwards, the flow-cell was clamped and PBST (nuclease-free PBS with 0,05% (v/v) of Tween20) with n = 1.3330 was flowed over the

chip. The kinetic measurement *R*(*t*) was started by determining the fixed angle of the low-angle side of the resonance dip in the angular reflectivity scan *R*(θ) (θ = 45°-60°) in PBST. The solutions were applied with a flow rate of 40 µL/min in a closed loop. Between every reaction step, PBST was flushed and an angular reflectivity spectrum *R*(θ) (θ = 45°-60°) was recorded to ensure the determination of the layer thickness *d*, respectively.

At the beginning of the kinetic measurement *R*(*t*), sucrose with 1%, 2% and 4% (w/v) in PBST (*n* = 1.3344, 1.3359, 1.3388) was applied for calibration purposes. Then neutravidin (1.87 µM) in PBST was reacted with biotin groups of the sensor surface for 30 minutes until saturation was established (5-20 minutes). The biotinylated primer sequence (biotin/20T/BS-) with the molar concentration of 40 nM was applied for 25 minutes. The ligated and exonuclease treated padlock probe (40 nM), which was prepared as described in chapter 5.2., was immobilized for 40 minutes. In cases of lower molar concentrations of PLP, the solution was prepared with the molar concentration of 40 nM and then diluted. In order to determine the change in mRIU, only the ligation buffer, which was treated as the PLP, was flushed for 5 minutes. If the PLP was pre-labelled with Cy5/C2CA- (10 nM), the PLP and the buffer were incubated ex-situ on the HulaMixer (Thermo Fisher Scientific) for 10 minutes. Additionally, the bulk response of Cy5/C2CA- in PBST was measured prior to the immobilization of the PLP.

The mixture for the RCA contained the DNA polymerase (100 Units of ϕ29-Pol) in the respective buffer (33 mM Tris-acetate, 10 mM Mg-acetate, 66 mM K-acetate, 0.1% (v/v) Tween 20, 1 mM DTT) and NFW-BSA (0.2 mg/mL). The total volume was 500 µL. The RCA mixture was flowed over the surface until an equilibrium of rebinding and unbinding of the polymerase was established. Then the dNTPs were added (100 µM of each dNTP). The baseline was established in RCA buffer, prior to the reaction. After 1 hour, the RCA reaction was usually stopped by flushing PBST. The amplified ssDNA strands were labelled by applying 10 nM of Cy5/C2CA+ for 15 minutes. The fluorescence background of the dye was measured prior to RCA.

5.6. Data fitting and evaluation

By flowing 1%, 2% and 4% of sucrose (w/v) in PBST for calibration over the sensor surface, it was possible to normalize the SPR response *R*(t) from the kinetic measurement by setting the baseline in PBST to zero for conversion into mRIU.

The angular reflectivity scans $R(\theta)$ after every immobilisation step were analysed by the Winspall programme enables fitting the curves with Fresnel reflectivity model for determining the thickness *d* and the refractive index *n* of the layers. The parameters, which were used for the fitting, are presented in Table 2. There are variations in the values of the refractive index *n* due to differences in the sensor chips, which happened during the production.

Table 2: Parameters used for fitting the measured layer thickness d at λ = 633 nm

layer	Thickness *d* [nm]	refractive index *n*
glass (LasF9)	0	1.845
chromium (Cr)	2	3.1 + 3.3i
gold (Au)	50	0.2 + 3.5i
SAM	1	1.45
neutravidin	fitted	1.45
primer (biotin/20T/BS-)	fitted	1.45
padlock probe	fitted	1.45
RCA product	fitted d_p	fitted n_p
PBST buffer	-	1.333

By using the (Eq. 5) stated in Chapter 3.2 the surface mass density Γ could be calculated from the determined layer thickness d_p with the values from Table 2. The polymer brushes can be additionally characterized by the grafting density σ in nmol/mm² (see Eq. 6), which is determined from the molar mass *MW* and the surface mass density Γ in ng/mm² for neutravidin (67 kDa), the primer (11.2 kDa) and the padlock probe (25 kDa).

The average distance between the individual chains *D* in nm can be derived from the surface mass density Γ of the padlock probe with the molar mass MW_{PLP} and the Avogadro constant $N_A = 6.022 \cdot 10^{23}$ according to the following equation. The factor *Q* is introduced to relate the fluorescence intensity ΔF with the surface mass density Γ.

$$Average\ Distance\ D = \sqrt{\frac{MW_{PLP}}{\Gamma \cdot N_A}} = \sqrt{\frac{MW_{PLP} \cdot Q}{\Delta F \cdot N_A}} \qquad (Eq. 7)$$

5.7. Gel-electrophoresis

For the gel-electrophoresis, the RCA reaction was conducted in liquid phase with a total volume of 40 µL. The mixture included 20 µL of the ligated padlock probe (40 nM), 2 µL of the primer sequence (biotin/20T/TS-) with a molar concentration of 40 nM, 1 µL of dNTPs (25 µM) and 2 µL of ϕ29-Polymerase (20 Units) in 13 µL NFW-BSA (0.2 mg/mL). The control sample contained an unspecific random sequence (40 nM) was used instead of the primer sequence. The samples were incubated on the HulaMixer. For stopping the reaction, the enzymes were inactivated on the thermomixer at 70°C with 700 rpm for 10 minutes.

10 µL of the RCA mixture was used for a 0.8 % agarose-gel. Prior to loading the sample was mixed with 10 µL of the 1:10 diluted loading dye. In order to determine the length of the ssDNA strands, 2 µL of a home-made ladder of 1 kb and 100 bp with 3 µL loading dye were used. The separation voltage was set to 100 Volt for about 30 minutes.

Another agarose-gel with 1 % was prepared for the ligated padlock probe. 100 µL of the samples with 10 µL loading dye were loaded into the chambers. At 125 Volt the DNA had 20 minutes to migrate through the gel.

5.8. Microarray experiments

The padlock probe was prepared one day before use as it is described in Chapter 5.4. The microarray experiments were conducted with 75x25 mm^2 (BK7) microscope slides, which were produced according to Chapter 5.3.

The gold coated slides were incubated in a neutravidin solution with the mass concentration of 3.5 mg/L for 30 minutes and subsequently in a biotin/20T/BS- (150 nM) solution or mixed with biotin/20T/11TS+ (150 nM) or biotin/20T/random (150 nM) for 70 minutes. The padlock probe was diluted with a final concentration of 150 mM NaCl and spotted by hand (0.5 µL) for the incubation overnight in a humid environment. The RCA reaction was started in individual chambers of a total volume of 100 µL with 16 U of Φ29 Polymerase, 10 µL 10x Reaction buffer, 2 µL BSA (10 mg/mL), 5 µL dNTP mix (2 mM), 2 µL of either Cy5/C2CA+/dideoxy (100 µM) or Atto532/BA+/dideoxy (100 µM) and 79.5 µL MilliQ water for 1.5 hours at 37 °C. In between the immobilization steps, the slides were washed with PBST two times, shortly rinsed with MilliQ water and dried in a centrifuge at 700 rpm for 4 minutes. The microarrays were scanned with the green channel of the Tecan PowerScanner (Männedorf, Switzerland).

6. Results and Discussion

The single-stranded padlock probe OXA-48 was designed by the collaborator Ivan Barišić (AIT, HMD) with three distinct sections. It contains the target sequence TS+ (35 bp), which is the complementary sequence of *bla*$_{OXA-48}$ for detecting its presence in samples. In bacteria, this gene encodes for *β*-lactamase.

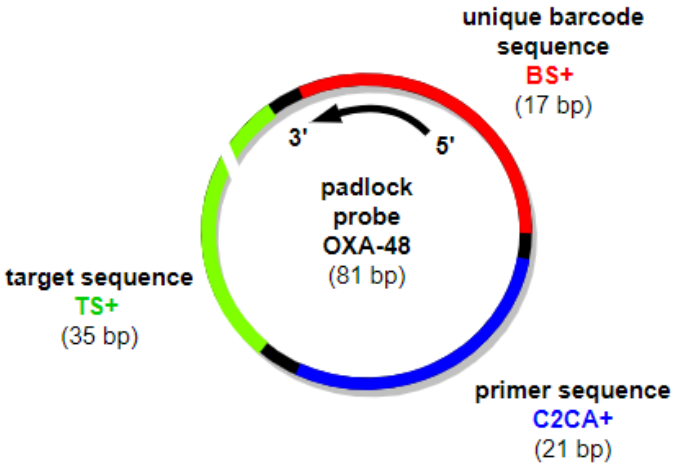

Figure 29: Detailed schematic representation of the padlock probe OXA-48, containing three specific sequences: the target sequence (TS+) in green with the complementarity to the target sequences in the sample (TS-); the unique barcode sequence (BS+) in red with the complementarity to the biotinylated barcode sequence (BS-), which is attached on one end to the sensor surface, to immobilize the padlock probe on the chip; the primer sequence (C2CA+) for fluorescently labelling the RCA generated ssDNA

Another segment of the padlock probe is the unique barcode sequence BS+ with 17 bp for capturing the padlock probe on the surface, which serves for the attachment of the RCA product on a solid support. The primer sequence C2CA+ with 21 bp is used for labelling with fluorescence dyes. The overall padlock probe has 81 nucleotides. The plus sign indicates the complementary sequence to the corresponding minus sign. The length of the PLP with 0.65 nm per base is 52.65 nm. Therefore, the corresponding radius of the circularized strand is 8.38 nm.

Furthermore, the PLP is utilized for the RCA reaction that is first tested in the bulk solution (Chapter 6.1) and afterwards deployed at a gold surface (Chapter 6.2). Then, the changes in the properties of RCA-generated ssDNA chains tethered to the solid surface are investigated depending on the grafting density (Chapter 6.3). The conformation of the tethered ssDNA chains can be manipulated by the choice of the solvent, interactions with specific ions (studied in Chapter 6.4) and by the affinity binding of short single stranded DNA sequences serving as

staples (investigated in Chapter 6.5). In particular, the developed procedures for RCA-generated ssDNA can serve as amplification for assays with fluorescence readout. These long chains can serve as labels that can dock large amounts of fluorophore tags and thus greatly increase the measured fluorescence signal per captured target analyte on the surface. In this thesis, the fluorophore tags were specifically bound to the repeating sequences of RCA-generated ssDNA chains (associated with the target molecules) by using short oligonucleotides conjugated with organic fluorophores. Firstly, the reversibility of this binding was studied (Chapter 6.6) and then routes towards the implementation for biosensing were demonstrated. The initial study was performed for the readout of an assay based on a) surface plasmon enhanced fluorescence and b) by enzymatic RCA reaction (Chapter 6.7). In order to explore possible applications for multiplexed detection methods, microarray-based fluorescence readout with enzymatic RCA amplification was tested (Chapter 6.8). Finally, the use of fluorescence microscopy for the interrogation of individual binding events is utilized in the context of single molecule detection (Chapter 6.9).

6.1. Elongation of ssDNA by RCA in solution

In this thesis, RCA is used to amplify a circular padlock probe on a solid substrate. However, to prove the protocol consisting of a series of reactions, the RCA was firstly performed in solution. Details of the padlock probe were described previously (see Chapter 6).

The circular padlock probes were prepared according to the procedure described in Chapter 5.4. All reaction steps were performed in Eppendorf tubes and are schematically presented in Figure 31. The molar concentrations (c_{PLP} = 40 nM, 4 nM, 400 pM) of the target sequence (TS-) were varied before the ligase reaction and Exonuclease I treatment. The circular PLP was hybridized with the complementary sequence biotin/20T/TS- for the amplification. The RCA was conducted on a shaker for 30 seconds, 1 minute, 2 minutes, 5 minutes, 10 minutes and 20 minutes. Afterwards, the polymerase was immediately inactivated at 70°C for 10 minutes. For the control sample, a random sequence was used for the ligation reaction instead of the target sequence (TS-). The control was equally treated as the sample with 20 minutes of RCA reaction.

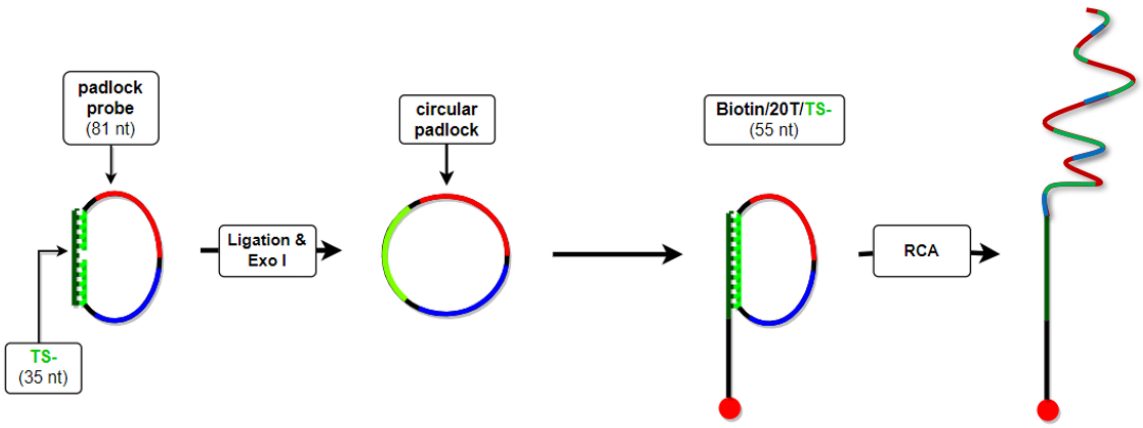

Figure 31: Schematic overview of the RCA in solution after the ligation and Exonuclease I treatment

The solutions, which contained different molar concentrations of the PLP were first examined with agarose gel-electrophoresis (see Figure 30). The oligonucleotides were separated according to size, which can be determined by the 100 bp ladder (Lane 2). All the lanes, which contained PLP (Lane 3 - Lane 6), showed a clear band around 100 bp and can be associated with the 81 nt long padlock probe. The intensity of the bands decreases by dilution of the target seuqence, shown in Lane 5 for c_{PLP} = 4 nM and in Lane 6 for c_{PLP} = 400 pM.

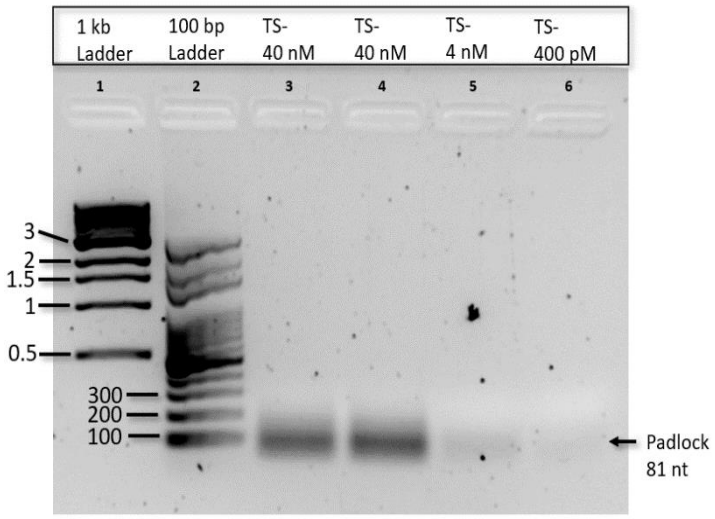

Figure 30: Image of 1% agarose gel loaded with 1kb (Lane 1)/100 bp (Lane 2) ladder and padlock probe after ligation and exonuclease treatment with different molar concentrations by dilution of the target sequence TS- (Lane 3- 6)

Another agarose gel-electrophoresis was conducted for separating the ssDNA after the RCA reaction (see Figure 32). For the new experiment, the circular padlock probe with c_{PLP} = 40 nM of the target sequence were newly prepared. 20 µL of the PLP sample were used for six RCA reactions without temperature control.

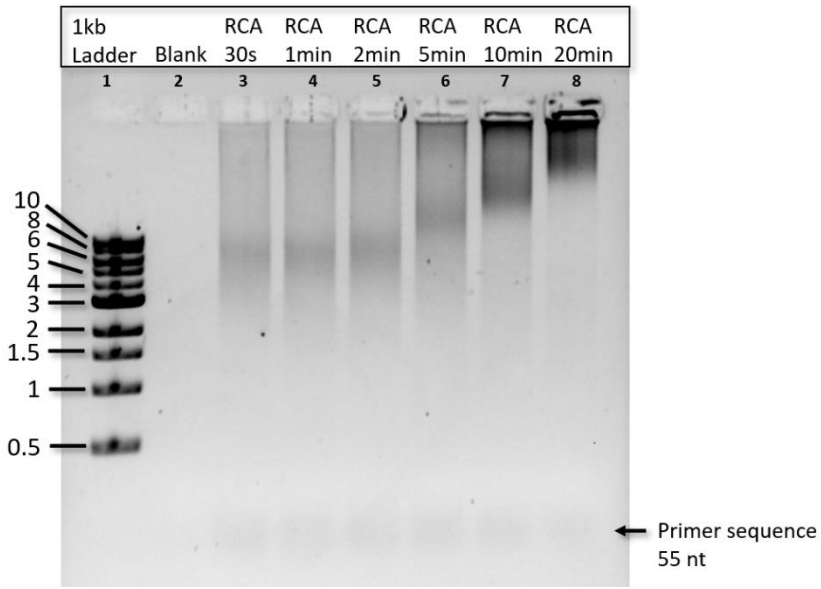

Figure 32: Image of 0.8% agarose-gel loaded with 1 kb ladder (Lane 1) and the RCA product after different times of enzymatic reaction and deactivation of the polymerase (Lane 3-8); control without padlock probe in Lane 2

Figure 32 shows the 1 kb ladder in Lane 1 for determining the size of the RCA product. The RCA product manifest itself (lanes 3-8) as dark bands that are shifting to higher molecular mass when increasing the RCA reaction time. A certain distribution of the length of the RCA product can be seen as a smear of these bands on the gel. The smearing of RCA product was already reported in literature before.[48,128,129] The center of the dark bands can be used to estimate the average length with the highest produced amount of similar sized ssDNA.

The lanes with the reaction time of 30 seconds (Lane 3), 1 minute (Lane 4) and 2 minutes (Lane 5) show very similar results and the bands are at the same level between 9000 and 10000 bp. This can be attributed to the short incubation time. It is worth of noting that the RCA reaction was terminated by heating the solution up to 70°C after the reaction, which does not allow to accurately control the time below 1 minute.

Besides the shifting of the RCA dark bands, their intensity increases with longer reaction times. After 10 minutes of RCA reaction, the ssDNA strands already reached a size, which strongly hinders movement through the gel and thus the bands are located close to the loading chambers. With increasing size of the RCA product, the ssDNA strands are more retained and therefore give a bright signal in the loading pockets. This was already observed and reported by Ducani et al.[130]

Since the DNA ladder does not contain any DNA longer than 10 kb, the length of the ssDNA strands after 2 minutes cannot be accurately determined with the used gel. However, one can estimate the speed for the shorter times of about 800 nt/s, which is more than two orders of magnitude faster in comparison to the elongation speed on a solid support of about 235 nt/min[131].

6.2. Elongation of ssDNA by RCA on the surface

The concept of the assay has been proved by performing the experimental reaction steps in solution (see Chapter 6.1). The next step is the implementation of the assay on a solid support. Thus, a gold surface was functionalized for the specific capture of the target analyte, which in this case is the circular padlock probe. Subsequently, the initiation of the RCA produced long ssDNA ensembles with one end of each strand tethered to the surface.

The formation of the circular padlock probe is illustrated in Figure 33. Instead of the target analyte from a patient sample, a synthetic DNA sequence (TS-) was used for the experiments. The affinity binding of this oligonucleotide to the linear padlock probe PLP (performed *ex-situ*), leads to hybridization of the complementary sequence. During the subsequent ligase reaction, the artificial nick of the padlock probe is sealed and the padlock probe is circularized.

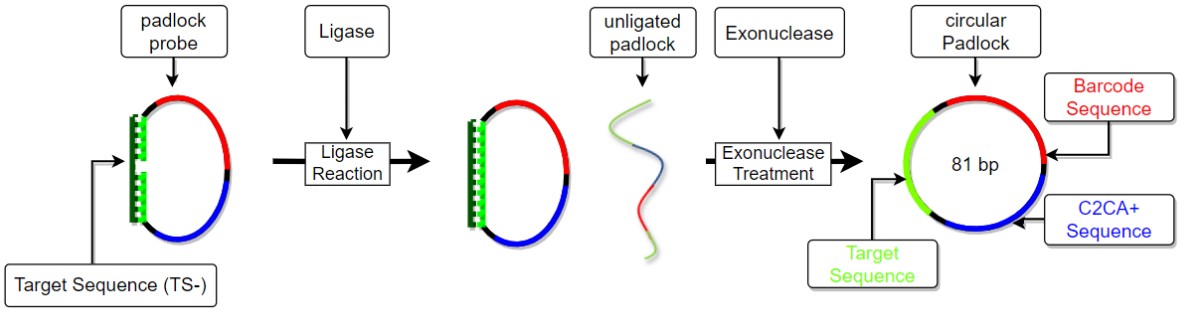

Figure 33: Schematic overview of the ligase reaction and Exonuclease I treatment ex-situ

However, after the ligase reaction unligated padlock probes can still be present in the solution that did not react with the ligase. Therefore, the unligated padlock and the target sequence need to be removed by the exonuclease treatment. The Exonuclease I degrades single stranded DNA in the 3' to 5' direction. It is assumed that the final concentration of the circular padlock probe ranges between the concentration of the initial padlock probe and the target sequence.

In order to perform the SPR / SPFS study, the RCA reaction was performed *in-situ* on a gold-coated sensor chip. For the chip production, glass slides were evaporated with 2 nm of chromium and 50 nm of gold. The surface was coated with a mixed self-assembled monolayer of thiol-OEG-OH and OEG-biotin headgroups in the ratio 5:1. In this way, antifouling properties could be achieved, and the binding of molecules via a biotin tag is controlled. The biotin groups function as linker in order to attach neutravidin. This biointerface provides the possibility to bind capture oligonucleotides, which carries a biotin tag on one end. Due to the fact that neutravidin has four binding pockets, the capture sequence can be attached to the surface. It consists of a spacer (20 thymine nucleotides) to prevent quenching of fluorescence by the metal surface and the barcode sequence (BS-), which is complementary to one section of the padlock probe.

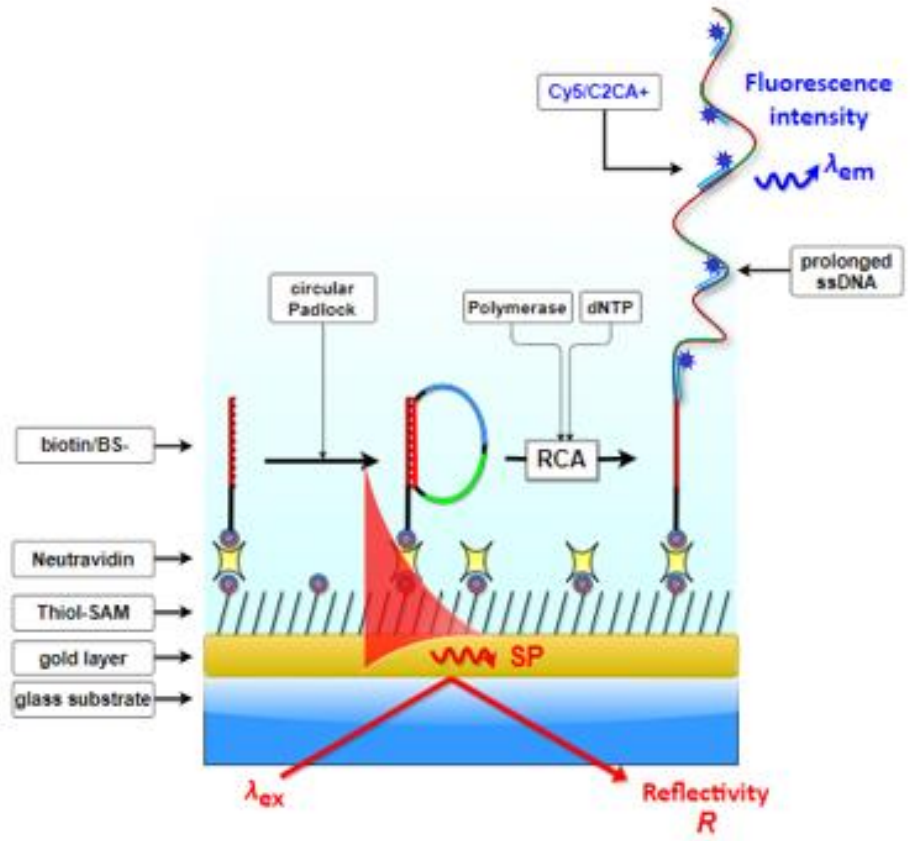

Figure 34: Schematic overview of the immobilisation of the biotinylated barcode sequence (biotin/BS-), the capturing of the circularized padlock probe and the rolling circle amplification (RCA) on the interface of the biosensor chip with SPFS readout

After affinity binding the circular padlock probe on the surface with a capture sequence, the RCA is initiated with the addition of the ϕ29-DNA-polymerase and dNTP's. Long single stranded DNA strands with the repetitive sequence of C2CA-, target TS- and barcode sequence BS- are grafted from the sensor chip. The addition of complementary sequences (C2CA+) with the Cy5-tag allowed the fluorescence labelling of the RCA product (see Figure 34).

With the SPR kinetic measurements $R(t)$ the experimental work-flow can be monitored and each immobilization step can be characterized. A typical kinetic experiment is shown in Figure 35. The angular reflectivity scans $R(\theta)$ are used to document the change in mass, which was bound to the surface (see Figure 36). These changes were determined by fitting the measured curves $R(\theta)$ with Fresnel reflectivity model by using the parameters stated in Table 3 and as further described in Chapter 5.6. From this the surface mass density Γ and grafting density σ can be determined. $F(\theta)$ was recorded to follow the changes in fluorescence intensity when the dye tagged sequences were hybridized to the RCA product. $\Delta F_{PSP} = 4.73 \cdot 10^4$ cps at the maximum peak intensity of the surface plasmon enhanced fluorophores was extracted as characteristic value.

The described procedure for the implementation of RCA on a solid support was applied in all the experiments in the following chapters (6.3 - 6.7) unless deviations from the introduced assay were stated.

Table 3: Fixed parameters (in grey) and calculated values after each immobilization step; thickness d and refractive index n (for the RCA generated ssDNA brushes) determined by the shift of the reflectivity curve to higher angles in PBST with n = 1.333 by fitting the curve with WinSpall

	Thickness *d* [nm]	refractive index *n*	Molar mass M_W [g/mol]	**surface mass density Γ [ng/mm²]**	**grafting density σ [nmol/mm²]**	**molecules/mm²**
Neutravidin	3,3	1,45	67000	1,93	2,9E-05	1,7E+10
biotin/20T/BS-	0,1	1,45	11689,7	0,06	5,0E-06	3,0E+09
Padlock	1,5	1,45	25029,1	0,88	3,5E-05	2,1E+10
RCA	3170	1,3392	327	98,27	3,0E-01	1,8E+14

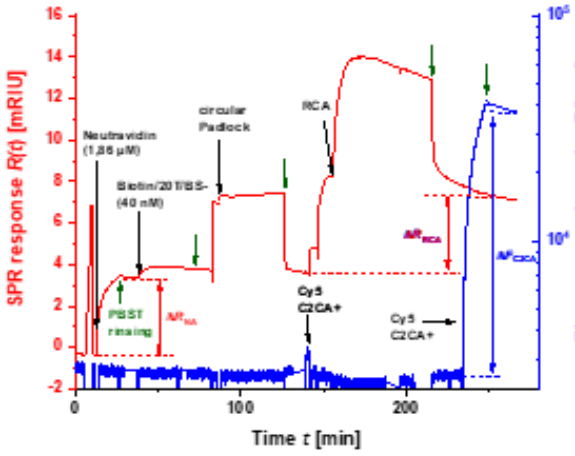

Figure 35: SPR response monitored over time R(t) in red at a fixed angle in a flow cell of 10 µL sensing volume; fluorescence intensity in blue

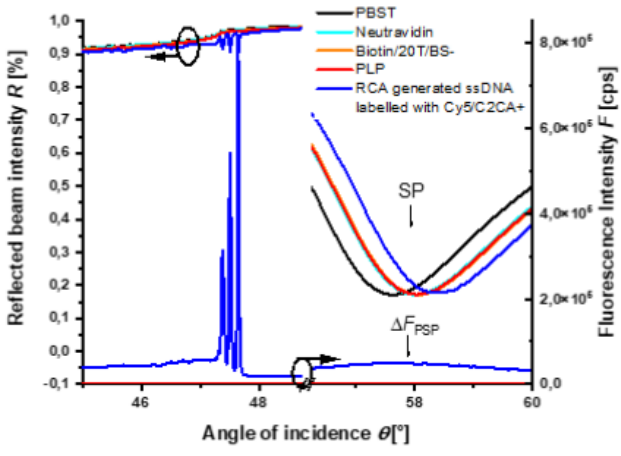

Figure 36: Angular reflectivity scans R(θ) and F(θ) after every immobilisation step and fluorescence intensity after the introduction of Cy5 labelled oligonucleotides

6.3. Effect of grafting density to RCA generated ssDNA chains

The characteristics of RCA-generated ssDNA chains at the plasmonic sensor surface have been investigated by using probing with evanescent wave optics in optical configuration that combined SPR and SPFS methods. Firstly, the behavior of the ssDNA chains is studied as a function of the tethering density on the surface that was controlled by the concentration of the padlock probe PLP reacted with the gold sensor surface with immobilized capture sequence BS-.

6.3.1. Control of average distance between tethering points

The ligation and exonuclease treatment for the creation of the padlock probe was conducted as described in Chapter 5.4. with c = 40 nM of the target sequence TS- and c = 90 nM of the linear padlock probe PLP. Therefore, it is assumed that the end solution will have a concentration of circular PLP of c_{PLP} = 40 nM as the dissociation rate of the affinity bound duplex is slow in comparison to the reaction time. After the preparation of the padlock probe with a concentration of c_{PLP} = 40 nM, the solution was diluted. Table 4 shows all PLP concentrations, which were used for the titration of the padlock probe.

Table 4: Overview of the PLP dilutions with the according molar concentration c

PLP dilution	c_{PLP}
1:10000	4 pM
1:1000	40 pM
1:100	400 pM
1:10	4 nM
1:1	40 nM

In order to employ the SPFS method, solutions with the set PLP concentration c_{PLP} was *ex-situ* reacted with Cy5/C2CA- (c = 10 nM) on the Hula-mixer for about 10 minutes. Afterwards, each solution with PLP concentration c_{PLP} was flowed over the sensor surface for 40 minutes in order to affinity capture the PLP (see Figure 37) followed by rinsing with buffer. In between every concentration step upon the rinsing step, an angular reflectivity scan $R(\theta)$ was conducted and the fluorescence intensity ΔF was recorded. As Figure 38 shows, the fluorescence intensity was increasing with the concentration c_{PLP} reaching the saturation level

of ΔF_{PSP} = 7.90·10^4 cps at c_{PLP} > 40 nM and exhibiting Langmuir isotherm behavior (showed as a fit).

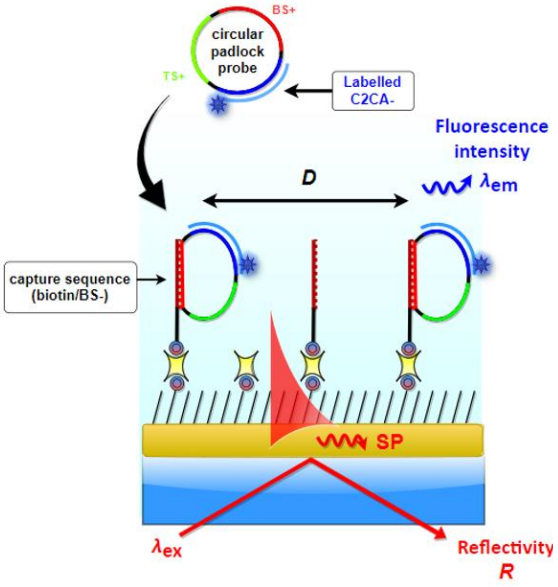

Figure 37: Schematic drawing of immobilizing directly labelled PLP

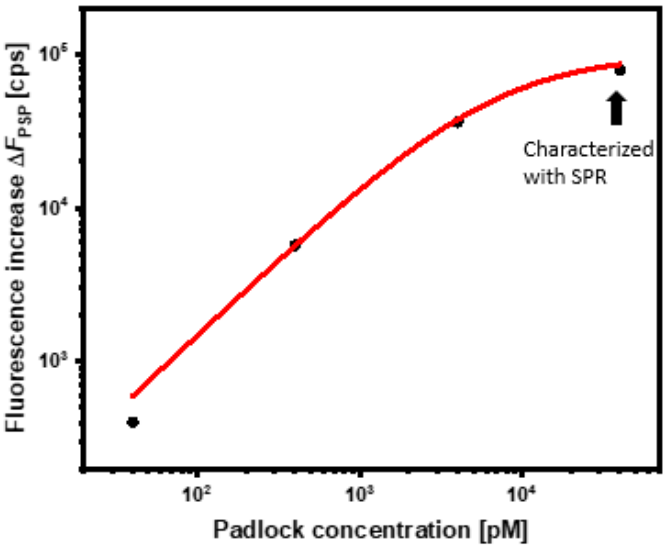

Figure 38: Linear scaling of the padlock concentration with the fluorescence intensity at c_{PLP} < 40 nM

In order to determine the surface density of the affinity-captured PLP probes (that later serve for RCA generation of long ssDNA chains), the SPR changes was measured in parallel to the fluorescence intensity ΔF. However, the SPR measurements were not sensitive to measure changes for the whole concentration range and allowed to determine the surface mass density $\Delta\Gamma$ = 0.18 ng/mm² only for the highest concentration of c_{PLP} = 40 nM. Then, by using the molecular weight of the PLP of MW = 25 kDa and the assumption that the fluorescence signal ΔF_{PSP} is proportional to $\Delta\Gamma$, a relation factor Q was determined (see Eq.7). As seen in Figure 39, we then estimated the final surface density of the captured molecule for each concentration of the PLP in the solution reacted with the surface and the corresponding average distance D as described in Chapter 5.6. As discussed further, in the RCA reaction these molecules serve as tethering points and the average distance D was used for estimation of the generated ssDNA grafting density.

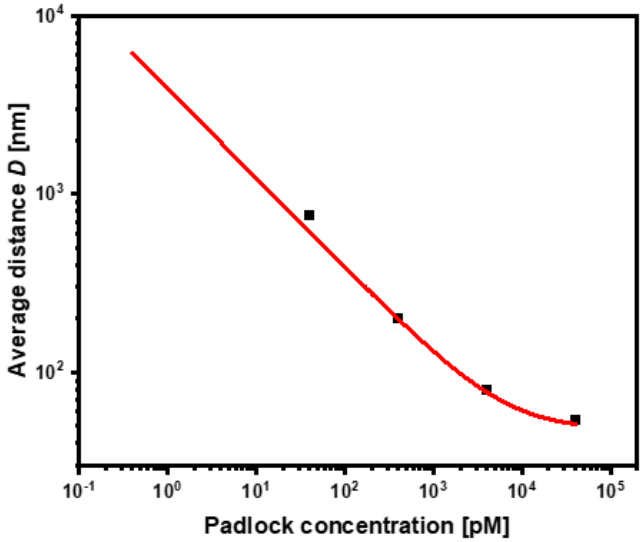

Figure 39: Correlation of c_{PLP} with the average distance D between the individual chains

6.3.2. Conformation of ssDNA chains at the surface

The PLP that was immobilized with capture sequences on the surface is used for the RCA reaction leading to anchoring of charged ssDNA. For the high concentration c_{PLP} associated with high density of tethering points at the surface (corresponding to short average distances *D*), densely packed ssDNA chains are assumed to facilitate chain stretching away from the sensor surface and taking a brush conformation. When reducing the concentration c_{PLP}, longer distances *D* between the chains occur, and a mushroom conformation can be expected for individually non-interacting chains.

From the average distance between the individual chains *D*, considerations about the structure of the chains can be made based on the polymer chain radius of gyration R_g. The R_g is an important value for quantifying the space volume it occupies, and different models for the calculation of the R_g value can be applied.

The free jointed chain model[132] is the simplest concept where a polymer coil, composed of a series of monomers, is only described by a random walk. Any possible interactions between the monomers are neglected. The polymer with a contour length *L* is conceptually divided into *N* monomers, each with a length l. This simple model does not consider steric hinderance and assumes completely free rotation of each monomer segment. Moreover, possible interactions with the solvent are also excluded[133] and the radius of gyration Rg can be expressed as the following function:

$$R_g = \sqrt{\frac{N \cdot l^2}{6}} \qquad (Eq. 8)$$

Literature reports about different values for ssDNA, varying from l = 0.43 nm[134] to 0.676[132,135]. The reason for the different values is the flexibility of the unpaired bases in single-strands, allowing elastic conformational changes. These properties are essential for processes happening in biological systems.[132]

Apart from the concept of the non-interacting chain, other models can be used that consider the non-free rotation of the polymer segments and the fact that the monomers have a defined volume. The Worm-like chain model[136] was first introduced by Kratky and Porod in the late 1940s. It mainly considers the stiffness of a polymer chain, which is introduced with the persistence length l_p. This concept is primarily suitable for charge carrying polymers like DNA.[137] The model describes the polymer chain as a flexible rod[138] with a persistence length of 50 nm for dsDNA, while for the more flexible ssDNA it ranges between 1 nm and 7 nm. Then, the gyration radius yields following expression for the Worm-like chain model:

$$R_g = \sqrt{\frac{2 \cdot l_p \cdot l \cdot N}{6}} \qquad (Eq. 9)$$

Additional theories about the excluded volume of a polymer have been established. They are suitable for polymers with finite volume and take into account the effect of a solvent.[139] According to interactions between the polymer and the solvent, swelling or shrinking can be induced.[140] The Flory-Huggins parameter χ gives information about the net interactions.[141] χ is large in case of a poor solvent, which results in a collapsed coil structure of the polymer. In a good solvent χ is small due to strong attractive interactions leading to expansion of the polymer coil. The theta solvent is called an environment where the interactions are equally balanced.[140] An approximation for the size of a polymer in a good solvent scales with the universal exponent $\boldsymbol{\nu}$ = 0.588. For a polymer in a poor solvent, this parameter is lower $\boldsymbol{\nu}$ = 0.33 and for the theta solvent it is set to $\boldsymbol{\nu}$ = 0.5.[142] This exponent $\boldsymbol{\nu}$ determines the gyration radius based on the following equation:

$$R_g = l \cdot N^{\nu} \qquad (Eq. 10)$$

In the experiments, the RCA reaction was carried out for one hour and the density of the grafted ssDNA chains from the sensor surface was varied by dilution of the PLP concentration in the solution (as discussed in Chapter 6.3.1.). The average distance between the individual chains *D* was determined by $Eq.7$ as described in Chapter 5.6. The sensor architecture for each PLP density was treated equally and was monitored by combined SPR and SPFS (see Figure 35 and Figure 36 for representative examples of the SPR and fluorescence signal kinetics). The fluorescence intensity associated to the generated ssDNA chains Δ*F* was recorded after 15 minutes of labelling with the Cy5/C2CA+ sequence. This fluorescence signal was measured for probing the sensor surface via surface plasmons with evanescent field reaching to distances of about 100 nm from the surface. The dependence of the fluorescence signal excited in this 100 nm thick slice ΔF_{PSP} on the average distance between the chains *D* is plotted in Figure 40. The data was measured for the ssDNA chains in contact with PBST that can be assumed as a good solvent. These data show a rapid decrease in fluorescence signal intensity with increasing the distance between tethering points *D* for the closely packed chains (*D* < 100 nm). For the distance range *D* = 100-300 nm, the dependence of fluorescence signal ΔF_{PSP} show a plateau and for long distances *D* > 300 nm it again rapidly decreases with *D*.

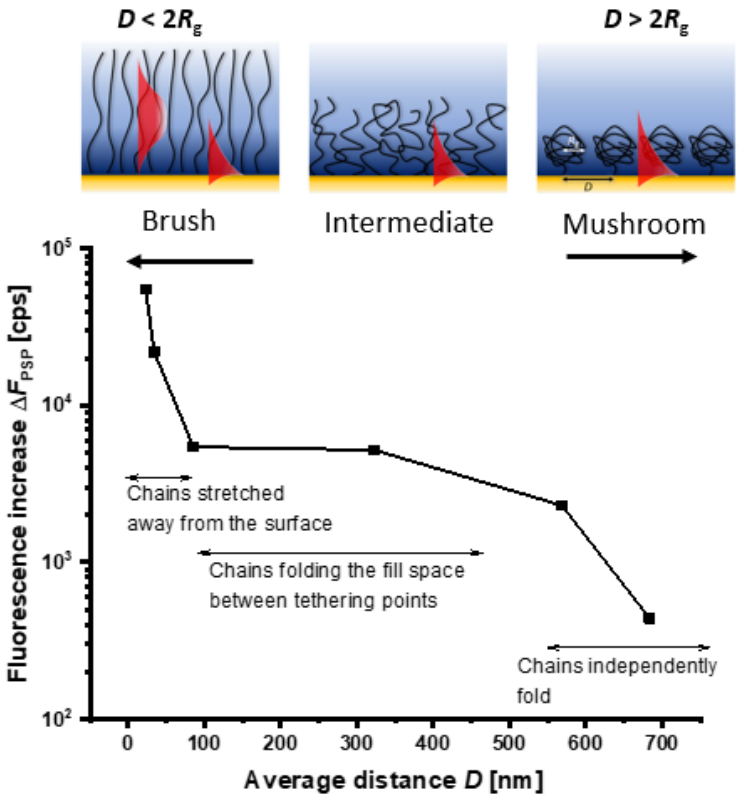

Figure 40: Conformation of RCA generated ssDNA depending on the average distance D by correlating the fluorescence intensity ΔF acquired from the angular reflectivity scans after hybridization with Cy5/C2CA+

This behavior shown in Figure 40 can be interpreted as a result of polymer chain conformation changes that are affected by surface density of ssDNA chains with a certain gyration radius R_g. Therefore, R_g values for the investigated ssDNA polymer chains was calculated with the use of the above models. For the used RCA reaction time of 60 min, the number of incorporated nucleotides N = 14100 by the polymerase was derived from the experimentally determined elongation speed of 235 nt/min reported in the previous work[131]. The respective values and other parameters are summarized in Table 5.

Table 5: Summary of parameters for calculation of the gyration radius R_g for ssDNA chains generated by RCA for reaction time of 60 min

number of bonds *N*	14100
length of indiv. Segments l	0.65 nm
persistence length of ssDNA l_p	1 nm - 7 nm

With the free jointed chain model ($Eq.8$), the R_g value of 32 nm was determined. However, since the ssDNA is a molecule with a certain stiffness, taking into account the respective persistence length by using the Worm-like chain model (*Eq.*9), leading to a higher value of R_g = 55 nm to 146.24 nm, taking into consideration the range of the reported values for l_p of ssDNA. With regards to assess the effect of the solvent, R_g is predicted to reach the value up to 179 nm by using the scaling law presented in $Eq.10$ and $\boldsymbol{\nu}$ = 0.588 for the good solvent.

At high densities represented by short $D < 2R_g$, the repulsive interaction between the negatively charged ssDNA can be assumed to force the chains to stretch away from the surface. In this regime, the chains take a brush conformation and increasing the average distance D will lead to lowering the fluorescence signal ΔF_{PSP}. This can be ascribed to the decreased number of chains that are present on the surface and thus a decrease in the emitters excited in the sensing volume occurs. At longer distances between the grafting points D comparable to $2R_g$, the ssDNA chains interaction weakens and a transition to mushroom conformation of individual polymers can be expected. This conformation occurs at average distances of $D > 2R_g$ and at further increased distances $D >> R_g$, the fluorescence signal ΔF_{PSP} again decreases with increasing the average distance D as the number of excited emitters on the non-interacting chains is proportional to the density of chains.

Indeed, the plateau region in the measured dependence Δ*F*(*D*) can be expected to occur at the transition between these two regimes, when the long ssDNA chains fill up the volume between the tethering points that is probed with the confined surface plasmon field. The RCA layer thickness in the brush regime is of several µm manifested as series of optical waveguide resonances in Figure 36. This length is much longer than the optically probed distance of 100 nm for the surface plasmons. Therefore, in the brush regime only a small fraction of the emitters attached to the ssDNA chains contribute to fluorescence signal ΔF_{PSP} as the majority of the chain segments is outside the probed distance. However, when diluting the anchoring points, the chains start experiencing weaker repulsion that allows them to be located closer to the surface within the sensing volume. There, they can contribute to the fluorescence signal ΔF_{PSP} and thus the effect of decreasing grafting density is compensated since more emitters per chain are present at the distances probed by surface plasmons. This effect is hypothesized to be responsible for the plateau in Δ*F(D)* occurring at *D* comparable to $2R_g$.

The models introduced before predict the $2R_g$ value in the range between 77 nm [for the random walk-based model $(Eq. 11)$] and 358 nm [for the Flory-Huggins model $(Eq. 10)$ with the exponent parameter for the good solvent $\boldsymbol{\nu}$ = 0.588]. The transition region observed is located between 100 and 300 nm and this suggests that the latter model matches better with the presented data. These observations confirm that models omit the repulsion between the chain segments associated with the charged backbone do not appropriately capture the characteristics of ssDNA chains tethered on the solid surface.

It should be noted that also other effects can affect the presented dependence in Figure 40. Firstly, the labelling sequences Cy5/C2CA+ may not be equally distributed throughout the ssDNA brush due to the hindered diffusion through the layer. Secondly, at very close distance to the surface (below 15 nm), quenching of the fluorescence signal occurs which was not taken into account in the discussion above. However, there can be assumed that this phenomenon will not affect the results since the gyration radius of the ssDNA coils in a good solvent is much higher compared to this distance.

The consideration about the conformation of the polymer chains and the dominant regime from brush to mushroom structure is important for the later approach to image single molecules with fluorescence microscopy (see Chapter 6.9.). In order to visualize individual chains, a coil-like conformation independent of neighbor strands is needed.

6.4. Conformation changes induced by interaction with ions

Since the utilization of evanescent wave optics for the probing of the ssDNA chains on the solid support is sensitive to the distance from the surface, the ability to control their conformation to the most sensitive region is of high importance when RCA is applied as an amplification method in sensor application. In the further experiments, the effect of molar concentration of $CaCl_2$ on the RCA-generated ssDNA chains was investigated as a function of ssDNA density. For this purpose, the RCA reaction was conducted on chips with varied padlock concentration similar to the previous Chapter 6.3.2. After labelling the RCA product with the complementary Cy5/C2CA+ sequence, $CaCl_2$ was flowed over the sensor surface and changes in the SPR and SPFS signal were monitored. In general, ssDNA has a negatively charged backbone and it strongly interacts with the positively charged Ca^{2+} ions by Coulombic forces resulting in possible crosslinking effects.

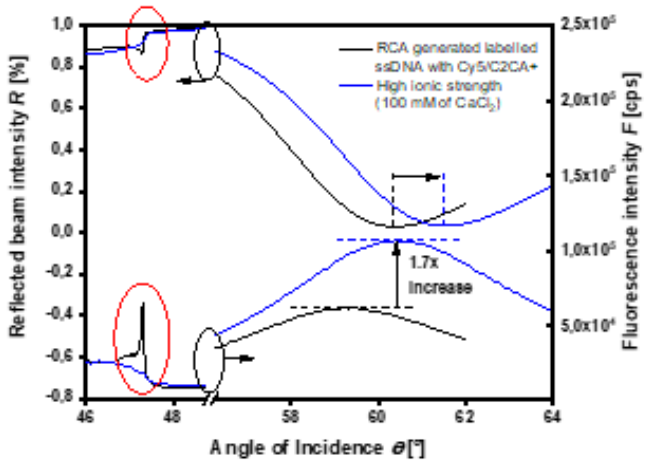

Figure 41: Angular reflectivity scans R(θ) and F(θ) after RCA (ssDNA labelled with Cy5/C2CA+, grown from c_{PLP} = 40 nM) and effect of Ca^{2+}

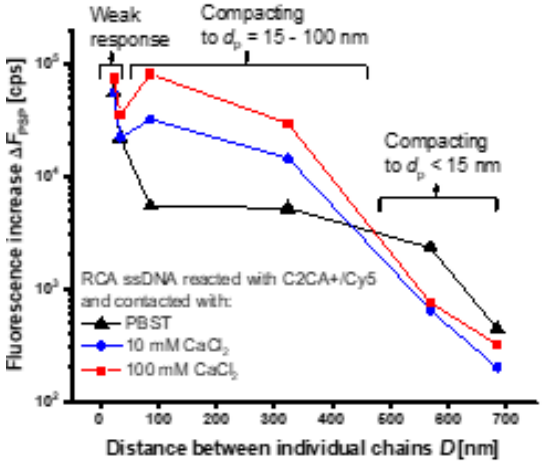

Figure 42: Effect of Ca^{2+} ions on the conformation of the ssDNA chains with different grafting densities

Obtained SPR / SPFS observations confirm that the presence of Ca^{2+} ions leads to a collapse of the ssDNA chains in a brush conformation when the distance *D* between the chains is low. As Figure 41 shows, the interaction with Ca^{2+} causes a decrease in the layer thickness d_p which is manifested in the angular reflectivity scan *R*(θ) as a disappearing of the optical waveguide feature, a shift of the SPR to higher angles and an increase in the peak surface plasmon-enhanced fluorescence signal ΔF_{PSP}. Interestingly, when increasing the average distance between the chains, the measured changes in surface plasmon-enhanced fluorescence signal ΔF_{PSP} due to the flow of Ca^{2+} ions show a complex behavior. The data presented in Figure 42 are derived from *F*(θ) of the plasmon mode (an example shown in Figure 41 for the highest

PLP concentration). The graph illustrates that the high ionic strength in the high-density brush regime does not have major effects on the fluorescence intensity ΔF_{PSP}. In case of short distances between the tethered strands $D < 30$ nm, the ssDNA stretches away from the sensor surface due to repulsion between the chains. In c = 100 mM $CaCl_2$ the response of the fluorescence intensity weakly increased by a factor of 1.35 for the highest density and 1.59 for the second highest density. This could be the result of already densely packed ssDNA chains, which do not have the space to further collapse (Figure 43). The polymeric network seems to be relatively rigid, which prevents the disturbance of the structure by high ionic strength.

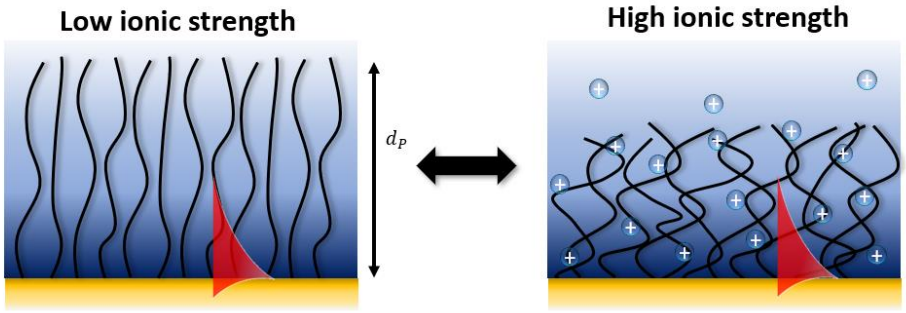

Figure 43: Schematic representation of the effect of Ca^{2+} ions on densely packed ssDNA brushes

When increasing the distance D between the chains into the range from 30 nm to 400 nm, the fluorescence intensity increase induced by the Ca^{2+} ions becomes much stronger. This can be explained by weaker Coulombic repulsion between the chains in the transition regime to mushroom conformation that offers volume which the chains can fill up. Thus, the ssDNA is placed closer to the surface, which leads to higher number of affinity-bound fluorophores located within the surface plasmon evanescent field ($d < 100$ nm). The most pronounced effect was observed for the intermediate states D = 85 nm and D = 323 nm, where the fluorescence intensity increased by a factor of 15 and 5.7 for the highest ion concentration of c = 100 mM. The brush thickness d_p of the collapsed polymer network is assumed to range between 15 nm to 100 nm. According to $Eq. 10$, considering the polymer coil in a poor solvent, R_g can be approximated with 15 nm.

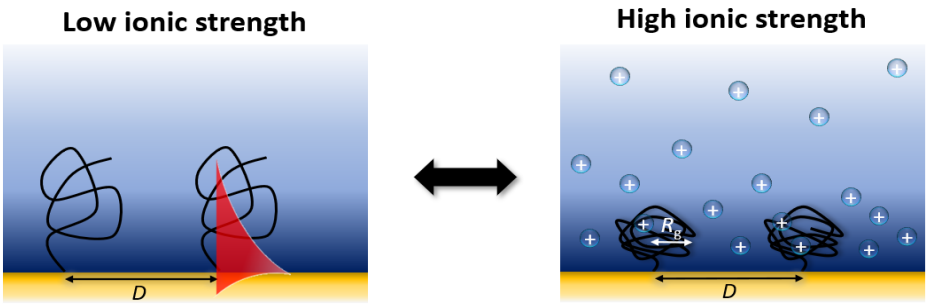

Figure 44: Schematic representation of the effect of Ca^{2+} ions on sparsely packed ssDNA mushrooms

Interestingly, when it comes to very sparsely tethered ssDNA chains with D > 400 nm, an opposite effect was observed. The fluorescence intensity ΔF_{PSP} was not enhanced but suddenly dropped by a factor of 0.28. In this regime, a mushroom-like structure was expected with a collapsed ssDNA thickness d_p of lower than 15 nm (Figure 44). This observation can be ascribed to the quenching of the fluorophores since the ssDNA chains were too close to the gold surface (the effect occurs in a distance d < 15 nm).

6.5. Conformation changes induced by interaction with ssDNA staples

Two approaches were tested for increasing the fluorescence signal detected per generated RCA chain. They can be used as amplification method in assays to achieve the strongest possible signal. The motivation is to manipulate the ssDNA to most efficiently improve the surface plasmon enhanced fluorescence for individual chains in order to be useful for ultrasensitive techniques. The evanescent field of SPs only reaches up to about 100 nm but the RCA product, forming high-density brushes, can have a thickness in micrometer range supporting the guidance of optical waves. But the highest sensitivity lies within the exponentially decaying field, while the waveguide modes cannot be observed when using low molar concentrations of the target analyte. Therefore, the majority part of the stretched ssDNA strands is not probed and do not contribute to the fluorescence signal. Hence, if more molecular mass and fluorophore binding sites can be placed in the right distance to the sensor surface, the fluorescence intensity ΔF_{PSP} will increase.

The first approach was to compact the polymer brush like DNA origami with the introduction of staples to the sensor architecture. This should lead to an orderly packed DNA structure, which will locate more dyes within the exponentially decaying field. The second approach is about tethering the replicated strands multiple times to the sensor surface with tethering

sequences since the long ssDNA strands are only attached to one anchor on the surface. The enhancement strategies are examined for the further implementation on a microarray.

6.5.1. Application of DNA staples

The plasmonic sensor can only detect molecules in a certain distance from the surface. In addition, waveguide modes are generated if the densely packed DNA layer exceeds a thickness of 1 µm. This case occurs by using a PLP concentration of c_{PLP} = 40 nM (used for all experiments in this chapter), in order to control the density, for the RCA on the chip, which shows that the DNA brushes are not fully probed in the plasmon mode due to the high thickness. To improve the sensitivity, more fluorescence dyes need to be located in the evanescent field. One way to achieve this is to densify the RCA product by using staples, which are employed in DNA origami. For this purpose, three different oligonucleotides were designed, called accordion probes. They were ordered in three distinct variations, in which one probe either has an additional fluorophore (Cy5) attached or a dideoxy modification. The accordions were designed to have two or more binding parts, which are complementary to the repeating sequences of the RCA-generated ssDNA strands. By this principle, the staple probes should hybridize to two distinct segments of the repeating ssDNA sequence, which should lead to the formation of multiple loops. Three accordions (BA shown in Figure 45, DC, DCBA) were designed for this purpose, which are affinity binding in the described manner. The BA+ accordion consists of the TS+ sequence, while the DC+ accordion includes the C2CA+ sequence.

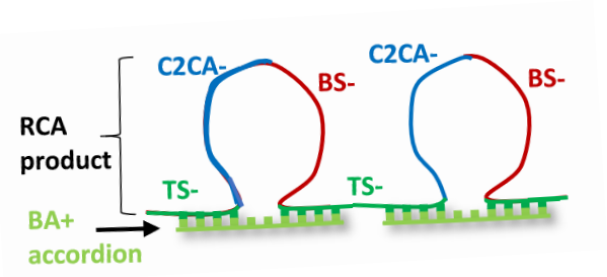

Figure 45: Hybridization of the BA+ staples to two distinct segments of the RCA product, inducing the formation of a loop, including the C2CA- and the BS- sequences

Furthermore, there is the possibility that no compaction occurs. The oligos could rather crosslink the RCA product, as shown in Figure 46. The result could be a hydrogel-like architecture, since the accordions might not diffuse further inside and stay on the outer strands, which could lead to inhomogeneity.

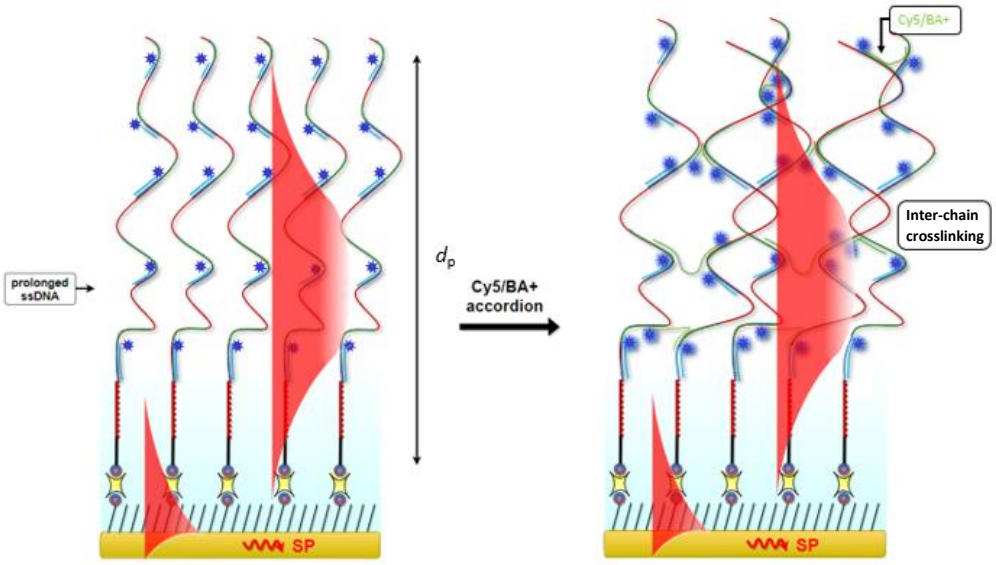

Figure 46: Schematic representation of the effect of Cy5/BA+ hybridization to the RCA product by inter-chain crosslinking

Figure 47 shows the impact of the accordions in comparison with regeneration steps in between (see Chapter 6.6). It can be observed that the Cy5/BA+ accordion achieves the highest fluorescence intensity ΔF_{PSP} = 1.1·10^5 cps and Cy5/C2CA+ the lowest intensity ΔF_{PSP} = 1.9·10^4 cps.

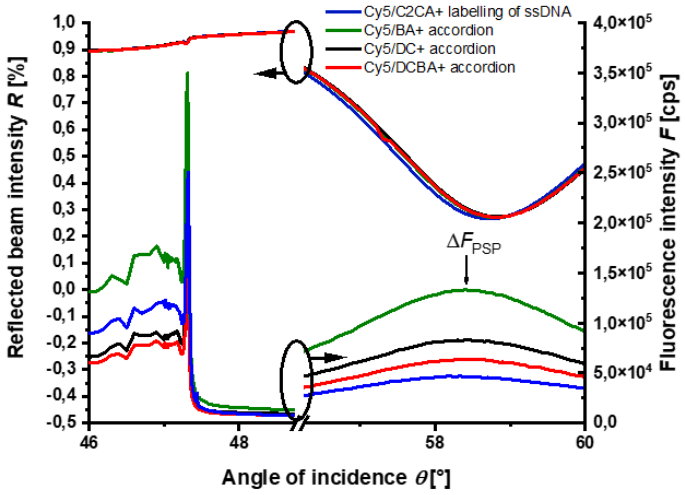

Figure 47: R(θ) and F(θ) for the comparison of fluorescence increase of Cy5/C2CA+ with different staple probes (BA+, DC+, DCBA+)

Effect on brush conformation

After running the RCA reaction for one hour, the ssDNA strands were labelled with Cy5/C2CA+ (*c* = 10 nM) for 15 minutes. Afterwards, the non-labelled accordion probe BA+ (*c* = 10 nM)

without any modifications was diffusing inside the brush for 15 minutes and binding to the polymer chains for crosslinking or compaction.

As it is shown in Figure 48, no change can be observed, indicating no condensation of the ssDNA brushes. Applying the staples did not influence the angular position of neither the surface plasmon dip nor the waveguide mode. Additionally, there is no increase in the fluorescence intensity ΔF_{PSP}, which would mean that more fluorophores are probed by the evanescent field of the SPs.

The fluorescence intensity by labelling with Cy5/C2CA+ was recorded with $\Delta F_{PSP} = 5.7 \cdot 10^4$ cps. It decreased by a factor of 0.85 after applying the same molar concentration of BA+ probe, which is probably only the result of bleaching. For this experiment a surface mass density of $\Gamma_{RCA} = 93.38$ ng/mm^2 was achieved, indicating that there are many binding sides, which can be vacant after only 15 minutes of rinsing the oligonucleotide solutions.

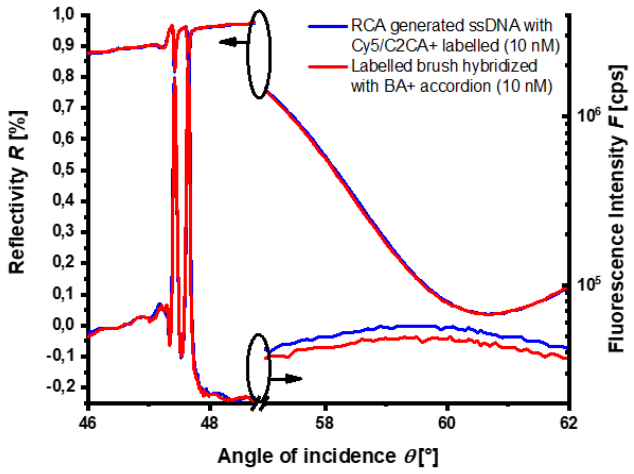

Figure 48: R(ϑ) and F(ϑ) showing no observed effect of using BA+ accordion on pre-labelled ssDNA brushes by Cy5/C2CA+; $c_{PLP} = 40$ nM

Additionally, the angular reflectivity scan $R(\theta)$ right after the RCA reaction was compared with the scan after labelling the RCA product with the Cy5/BA+ accordion (Figure 49). The fluorescence intensity reached $\Delta F_{PSP} = 1.04 \cdot 10^5$ cps after 15 minutes of labelling with the accordion. Therefore, it is confirmed that the staples are hybridizing to the RCA product. But since there is no shift of the plasmon dip of the reflectivity curve to higher angles observed, the compaction cannot be proven. There is a shift of the resonance dip of about 0.1° to lower angles, which probably is a result of washing away the rest of the polymerase.

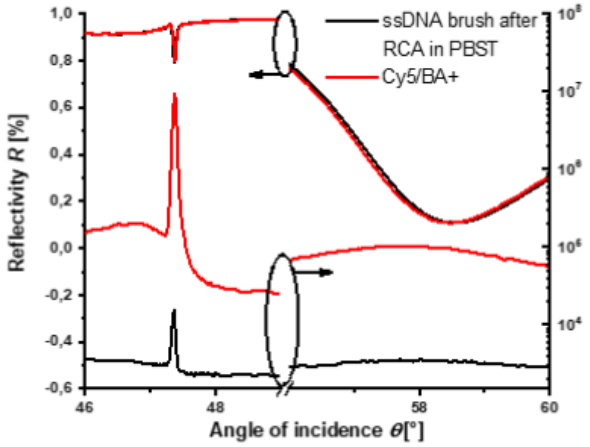

Figure 49: R(θ) and F(θ) for the proof of binding affinity of Cy5/BA+ accordion to RCA product by an increase in fluorescence intensity; c_{PLP} = 40 nM

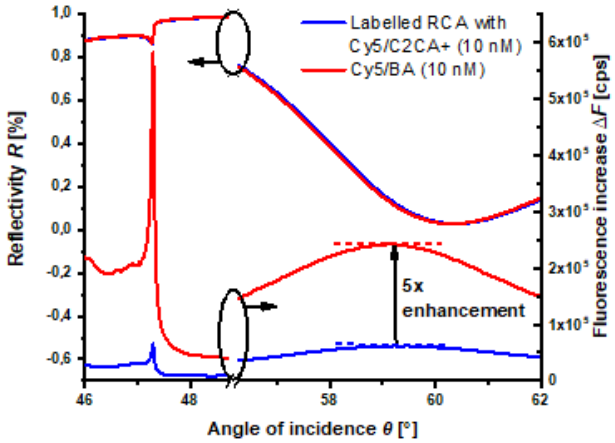

Figure 50: R(θ) and F(θ) for the comparison of fluorescence increase after hybridization of the ssDNA brushes with Cy5/C2CA+ and Cy5/BA+; c_{PLP} = 40 nM

With this method, no change of the SPR response *R*(t) could be achieved proving the compaction of the RCA product in the brush conformation. However, it was observed that the addition of the Cy5/BA+ accordion after labelling with Cy5/C2CA+ with the same conditions, showed a 5 times higher fluorescence intensity ΔF_{PSP} (Figure 50). Additionally, the features in the optical waveguide mode also increased. Thus, the hybridization of the staples occurred throughout the whole volume of the polymer architecture.

Effect of the addition of the accordion during the RCA

Two comparable experiments were set up with the exact same conditions. Only in one of the experiments the dideoxy modified accordion was added during the RCA reaction. The intention is to condense the strands right after they are produced by the polymerase.

Figure 51 shows, in comparison to the experiment without using accordion probes, a steep increase of the SPR response *R*(*t*) with the addition of *c* = 10 nM of dideoxy modified BA+ accordion at the start of the RCA. The angular reflectivity scans *R*(θ) and *F*(θ) reveal two waveguide features while there is only one waveguide mode in the comparative experiment observed (Figure 52). During the prolongation of the ssDNA strands, the accordions had the possibility to hybridize to the RCA product and bring the DNA closer to the surface, which is demonstrated by the steep increase in the SPR kinetic measurement *R*(t). After flushing with PBST in order to stop the amplification, the SPR response $\Delta R_{PBST\text{-}RCA}$ was 2.28 times higher for

the compacted polymer architecture. This indicates that the strands got orderly packed due to the addition of the BA+ accordion during the RCA reaction.

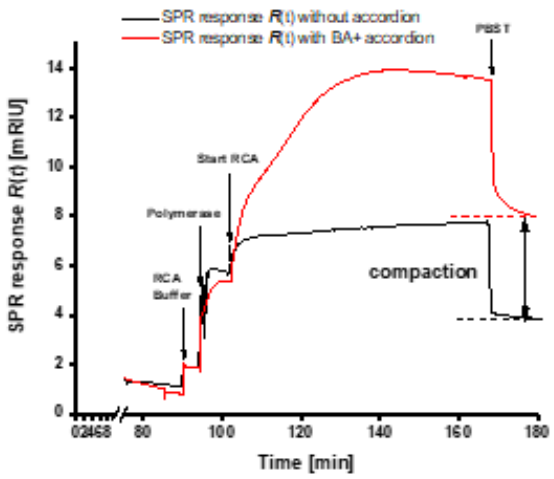

Figure 51: Comparison of kinetic measurements R(t) during the RCA reaction in the presence of BA+ probes (red) and the absence of staple probes (black) on a neutravidin coated sensor with an attached biotinylated BS- sequence layer

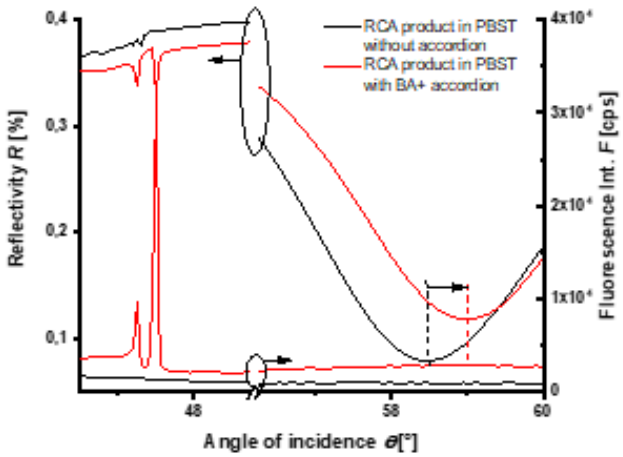

Figure 52: R(θ) and F(θ) for the comparison of the RCA generated ssDNA in the presence of BA+ probes (red) and the absence of staple probes (black) after the amplification reaction: c_{PLP} = 40 nM

After 1 hour of RCA reaction, the surface mass density was determined for the experiment without accordion probes with Γ = 21.90 ng/mm^2 and for the measurement with the dideoxy/BA+ staples with Γ = 128.10 ng/mm^2.

Nuclease-free water was flushed after the RCA in order to initiate the stretching of the brushes. In case the RCA product is compacted, they should not be able to stretch so far from the surface, which would be another indication for compaction. However, this does not seem to be the case, since the baseline of the SPR response $\Delta R_{RCA\text{-}NFW}$ is decreased after flushing with NFW by a factor of 0.17 and the second waveguide mode disappears (see Figure 53).

Furthermore, when the RCA product is labelled for 15 minutes with Cy5/C2CA+, the same fluorescence intensity ΔF_{PSP} = 6·10^4 cps is observed in both experiments. It can be assumed that due to flushing with NFW, the repulsion between the strands is stronger than the affinity interaction between the DNA bases. Therefore, the one segment of the compacting accordions could be ripped off and the ssDNA expands as in the previous experiment, since switching back to the original conditions in PBST showed that the swelling change was not reversible.

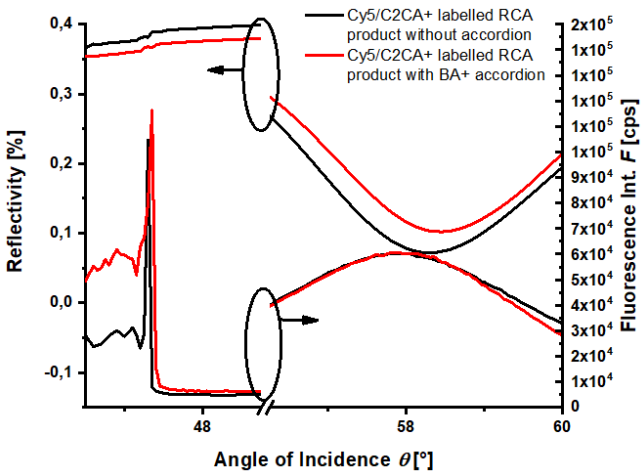

Figure 53: R(ϑ) and F(ϑ) for comparison of the RCA generated ssDNA in the presence of BA+ probes (red) and the absence of staple probes (black) after labelling with Cy5/C2CA+

The angular reflectivity scan $R(\theta)$ of the RCA product with the BA+ accordion shifted to $\Delta R(\theta) = 0.55°$ higher angle compared to the reference curve and $F(\theta)$ shows more waveguide modes. This is rather an indication that the RCA worked more efficiently in the experiment with the staples. It could be the result of the packing of the ssDNA strands and the reduced crosslinking (while this effect is dominant in the case of staple addition after RCA), which leads to a faster growth rate. If there are no staple probes during elongation, the strands entangle more easily, which could affect the growth of the ssDNA strands.

Effect of high ionic strength

The last approach, which has been investigated, includes change of the ionic strength in order to compare the behavior of the DNA strands without and with the addition of staples. For this purpose, $CaCl_2$ with molar concentrations of c = 1 mM, 10 mM and 100 mM were used.

The RCA product was labelled with c = 10 nM of Cy5/BA+ for 15 minutes in order to bind to the polymers, reaching $\Delta F_{PSP} = 7.8 \cdot 10^4$ cps. Afterwards, different concentrations of $CaCl_2$ were flowed over the surface for about 10 minutes. In between the three molar concentration steps, PBST buffer was rinsed. For comparison purposes, the same procedure was performed for the same polymer architecture labelled with Cy5/C2CA+ after regeneration with NaOH (further explained in Chapter 6.6.) and reaching $\Delta F_{PSP} = 1.7 \cdot 10^5$ cps (see Figure 54).

While the ssDNA brushes are exposed to c = 100 mM $CaCl_2$ a strong shift of the surface plasmon resonant angle to higher angles was observed. By fitting of the reflectivity curves $R(\theta)$ a collapse of factor 65 could be determined for the brush modified with Cy5/BA+. This change

is stronger than the collapse of factor 26, which was observed for the polymer architecture with Cy5/C2CA+. Additionally, when rinsing again with PBST buffer, the Cy5/BA+ hybridized brush partially preserved the angular shift (Figure 55) while for the Cy5/C2CA+, the ssDNA polymers returned to the original state (Figure 54). What is more, the fluorescence intensity in the plasmon mode increases by a factor of 2.7 for the modified ssDNA brush with staples in PBST whereas the signal decreased by 1.33 for Cy5/C2CA+. Therefore, the altered behavior with the application of accordions can be ascribed to the compacting and cross-linking effect.

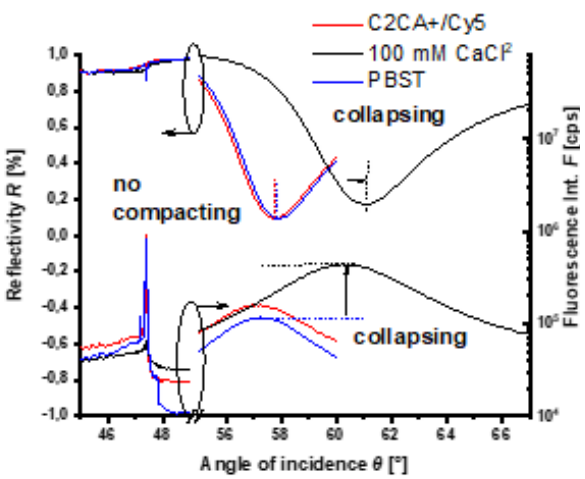

Figure 54: R(θ) and F(θ) as control experiment with Cy5/C2CA+ hybridized to the RCA product

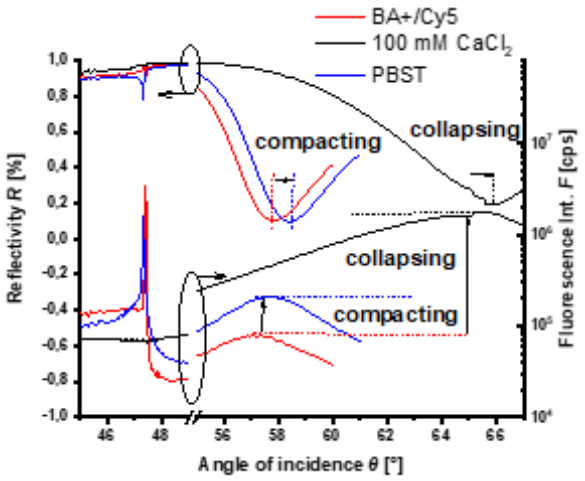

Figure 55: R(θ) and F(θ) of the effect of collapsing the ssDNA with Ca^{2+} ions after the hybridization of Cy5/BA+ staples

The inflexible conformation of densely packed brushes might prevent the hybridization of the short oligonucleotides with the second segment of the sequence to a distinct part of the RCA product for the compaction to be achieved. Since probably only one part is binding to the ssDNA, the staples rather function as a label. Therefore, no change in the angular reflectivity scans could be observed. By applying a solution with high ionic strength, the ssDNA is reversely condensed, which leads to denser packed brushes on the surface. The strands get closer together, giving the accordion probes the possibility to hybridize with their free end-segment to a distinct part of the RCA product (Figure 56). The outcome is irreversible compaction, which should lead to higher amount of molecular mass located within the evanescent field and an increase in fluorescence intensity ΔF_{PSP}.

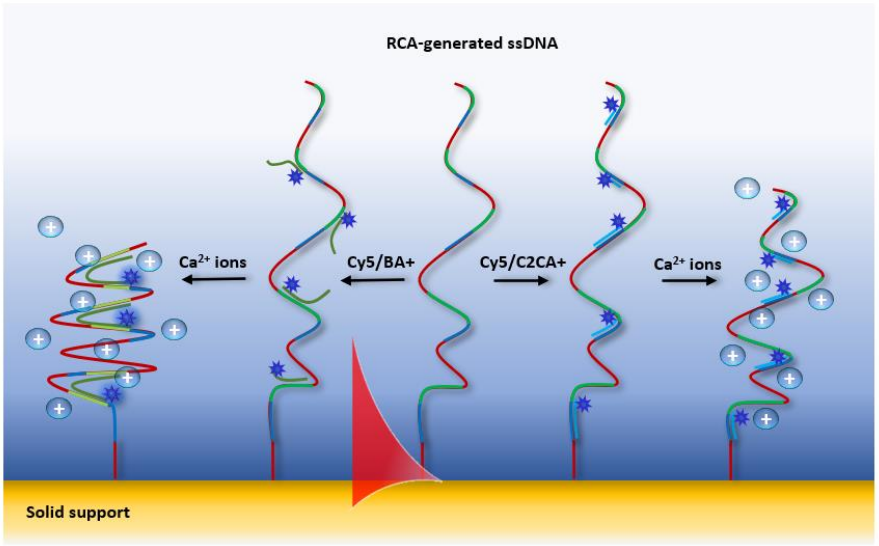

Figure 56: Schematic drawing of the effect of Cy5/BA+ and Cy5/C2CA+ hybridized RCA product when collapsed with high ionic strength

To sum up, the ssDNA architecture in the brush regime is relatively robust since the repulsion between the chains are quite strong, which does not allow much change of the conformation. Only in conjunction with using staple strands and high ionic strength, it was possible to induce compaction manifested as an increase in the fluorescence intensity ΔF_{PSP} and the shift of the plasmon dip to higher angles.

6.5.2. Guiding of ssDNA on the surface with tethering sequences

The elongated ssDNA strands can become microns long during the RCA reaction. The high-density brush layer features multiple waveguide modes. However, only about 100 nm from the surface are probed within the evanescent field of SPs. When decreasing the density and thickness of the polymer layer, neither waveguide modes can be observed, nor a significant shift in the surface plasmon resonance angle of the angular reflectivity scans $R(\theta)$. This limitation should be overcome by tethering the long ssDNA strands multiple times to the sensor surface by introducing a short complementary sequence in order to bring more segments attached to the complementary labelled Cy5/C2CA+ sequence within the exponentially decaying field (Figure 57). The tethering strands are affinity bound via the neutravidin-biotin system to the sensor surface. The aim is guiding the long ssDNA chains in an optimum distance to the surface for the enhancement of the fluorescence intensity ΔF_{PSP}.

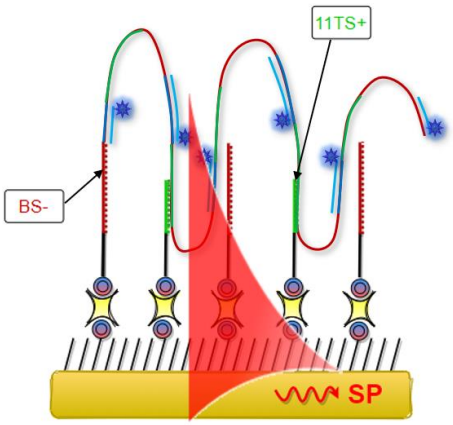

Figure 57: Schematic representation of guiding of the long on one end tethered ssDNA in close vicinity to the sensor surface by short guiding strands (11TS+)

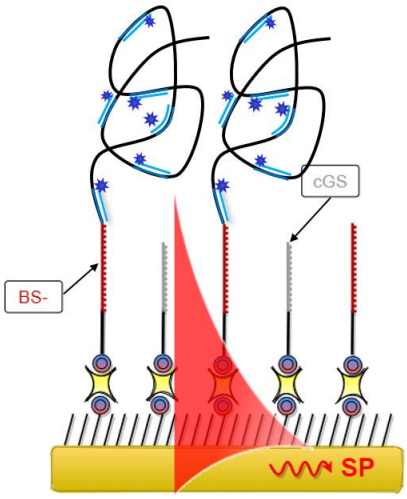

Figure 58: Schematic representation of the non-guiding effect of ssDNA with randomized oligonucleotide strands (cGS)

Bernadette Lechner tested the tethering approach with a tethering sequence of 32 nucleotides, which is complementary to the repeating TS- sequence of the RCA product.[131] The outcome of her experiments showed that the RCA could be influenced due to the high affinity interaction strength with the tethering strands. Hence, in order to prevent this effect, the tethering sequence was shortened to 9, 10 and 11 bases of the TS+ sequence. They were designed similarly as the biotinylated capture sequence (biotin/20T/BS-) and were also composed of a 20 nt thymine spacer with an attached biotin group. Their short and dynamic structure provides the possibility of reversible attachment of the elongated ssDNA.

The surface interface was composed of a neutravidin layer attached to the biotin groups of the SAM, as described in Chapter 5. The short tethering sequence with the 11 bases of sequence TS+ was introduced to the sensor surface in the same solution as biotin/20T/BS- in a ratio of 1:1. After conducting the RCA for one hour from c_{PLP} = 40 nM, waveguide modes observed as dips in the reflectivity curve $R(\theta)$ proved the success of the amplification process (Figure 59). A surface mass density of Γ = 98.27 ng/mm^2 and the fluorescence intensity of ΔF_{PSP} = 5.94·10^4 cps were achieved by using the biotin/20T/11TS+ sequence. Therefore, it can be concluded that the RCA reaction was not stopped by the introduction of the short tethering sequences due to less complementarity. It can be assumed that the optimum size of the tethering sequence lies higher than 11 nt but lower than 32 nt.

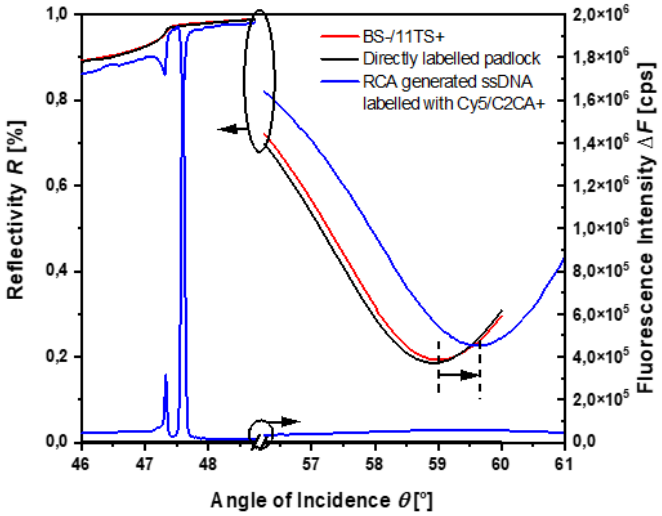

Figure 59: R(ϑ) and F(ϑ) after the successful growth of ssDNA strands by RCA reaction in presence of the guiding strands 11TS+ in the brush regime; c_{PLP} = 40 nM

It is assumed that the RCA reaction happens so fast, producing brushes with high densities and long-stretched strands, that the ssDNA strands do not have the space to attach to the tethering sequences on the surface. Therefore, $CaCl_2$ is used to reduce the repulsive forces between the polyelectrolytic chains, which might be responsible for the reduced hybridization efficiency with the shortened TS+ sequences. However, no significant change in the SPR response R(t) or in the fluorescence intensity ΔF_{PSP} was observed. Further considerations are the high-density brushes, which might hinder the attachment. Thus, the padlock probe was diluted 1:10, 1:100, 1:1000 and 1:10000 after the ligase reaction with c = 40 nM of TS- and the Exonuclease I treatment. The goal is to produce rather well-separated polymers instead of a tightly packed polymer architecture.

The fluorescence intensities ΔF_{PSP}, which were extracted from the angular reflectivity scans R(θ) and F(θ), from the ssDNA chains in the presence of Ca^{2+} ions and after flowing $CaCl_2$ are presented in Figure 60 and Figure 61 as ratio of the fluorescence data from the fluorophore labelled RCA product. The use of high ionic strength leads to the collapse of the ssDNA strands and thus to the increase of the fluorescence intensity ΔF_{PSP}. After the high salt concentration (c = 10 mM or c = 100 mM $CaCl_2$), the surface was flushed with PBST again.

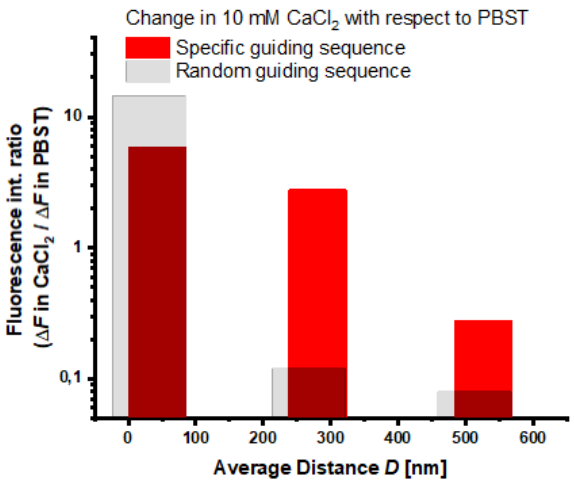

Figure 60: Change of the fluorescence intensity while changing the ionic environment (10 mM $CaCl_2$) after growth of ssDNA; red bars: biointerface with guiding strands, grey bars: biointerface with randomized oligonucleotides

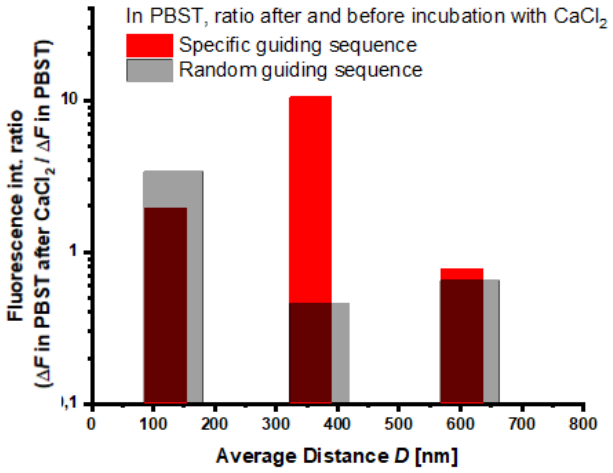

Figure 61: Change of the fluorescence intensity in PBST after flowing Ca^{2+}solution (10 mM); red bars: biointerface with guiding strands, grey bars: biointerface with randomized oligonucleotides

It can be observed that the fluorescence intensity ΔF_{PSP} increases while applying the highest salt concentration on high-density brushes by a factor of 1.5. For short distances between the individual chains *D*, there is no effect observed, which could indicate the tethering of the strands. The fluorescence intensity ratio decreases in PBST after using high ionic strength. The ssDNA strands are probably too tightly packed, preventing the attachment of the complementary sequences.

In comparison, at *D* ~ 320 nm the factors 10.48 after *c* = 10 mM $CaCl_2$ and 8.37 after *c* = 100 mM $CaCl_2$ in PBST were determined. In this case, the ssDNA chains were successfully guided on the surface, as can be seen from the higher fluorescence intensity ratios in Figure 61 (red bars). The $CaCl_2$ was able to bring the strands close to the sensor surface to provide a higher chance to hybridize to the tethering sequences.

Interestingly, during flushing with the high ionic strength solution, the fluorescence intensity ratio increases with the factor 2.79 with *c* = 10 mM and 5.67 with *c* = 100 mM, which is lower than the observed intensity in PBST. As previous experiments already proved (Chapter 6.3.2.), the ssDNA strands reversely collapse, which enhances the fluorescence intensity ΔF_{PSP}. The lowered density of the brush architecture could have the effect of quenching during the collapse with $CaCl_2$. This is observed for *D* > 320 nm. However, this allows the RCA product to hybridize to the tethering sequences attached to the sensor surface, which are not subject to quenching anymore after changing to PBST.

As control experiment, the 11TS+ sequence was replaced with a random sequence (biotin/20T/random) with 19 bases and the same conditions were tested (grey bars in Figure 60 and Figure 61). During the application of $CaCl_2$ the fluorescence intensity ΔF_{PSP} decreased due to the quenching effect as it was already observed in the tethering approaches. However, in PBST the fluorescence intensity ratio was reduced by a factor of 0.45 after c = 10 mM and 0.41 times after c = 100 mM for D ~ 320 nm, which only represents the bleaching of the dyes.

At high distances between the chains D > 570 nm, the tethering effect cannot be proven with the irreversible fluorescence enhancement after the high ionic strength solutions. On the opposite, the fluorescence intensity ratio in PBST was determined with 0.78 after c = 10 mM $CaCl_2$ and 0.49 after c = 100 mM $CaCl_2$. However, the tethering effect could still have occurred but already during the RCA reaction due to the very low density. In comparison, the control experiment shows similar responses. Therefore, it can be assumed that the mushroom architecture and the orderly guided ssDNA chains give similar results since the number of fluorophores within the evanescent field might be identical.

6.6. Regeneration of the RCA product

The performed experiments are time consuming and laborious. Additionally, since many substances are used, they can be expensive. Therefore, it is advantageous to achieve a partial regeneration of the sensor surface for providing the possibility to test different conditions on the ssDNA brushes.

For the denaturation of DNA, heating up the solution higher than the melting temperature is most effective. Reagents like formamide or DMSO can be used to reduce the melting temperature. Furthermore, acidic or alkaline agents influence the hydrogen bonding of double-stranded DNA. The denaturing effect of NaOH on DNA comes from the increase of hydroxide ions in the solution. OH^- interacts with the H^+ of the nucleotides guanine and thymine, resulting in the disruption of the H-bonds in the double-stranded DNA.[143]

Biacore™ recommends in their handbook to mainly use c = 10 mM glycine-HCl for protein disruption and c = 50 mM NaOH with the addition of either c = 1 M NaCl or 0,2%-0,5% SDS for removing proteins from nucleic acid. For disrupting double-stranded nucleic acid one should use c = 1 mM HCl.[144]

All experiments described in this chapter were conducted on a biointerface with c_{PLP} = 40 nM. After running the RCA on the chip, the product is usually labelled with c = 10 nM of Cy5/C2CA+. The sequence is complementary to the C2CA- sequences of the RCA product and hybridizes with 21 bp to the DNA brushes, which results in the detectable fluorescence signal. The complementary sequences can be removed by disrupting the interaction between the basepairs. This provides efficient clearing of fluorophores off the RCA product, which can then be used as further playground for additional experiments. It is utilized for testing the accordion probes, which are described in Chapter 6.5.1. For this purpose, c = 10 mM NaOH and c = 1 mM HCl were tested.

HCl

To test the regeneration with c = 1 mM HCl, the sensor surface was modified with a mixed thiol-SAM of biotin- to OH-groups with the ratio 1:10 and c = 18.6 nM of neutravidin in-situ for 15 minutes. After labelling of the RCA product with Cy5/C2CA+ the angular reflectivity scan showed a fluorescence intensity of ΔF_{PSP} = 3.9·10^4 cps (see Figure 62). For regenerating the surface, c = 1 mM HCl was flushed over the surface for about 5 minutes. The fluorescence intensity was reduced to about ΔF_{PSP} = 2.5·10^3 cps, but the plasmon dip of the angular reflectivity curve $R(\theta)$ shifted to higher angles $\Delta\theta$ = 0.25°. Therefore, it seems that the short oligonucleotides were successfully removed, but it can be assumed that the acid damaged the surface, since the SPR signal did not return to the baseline.

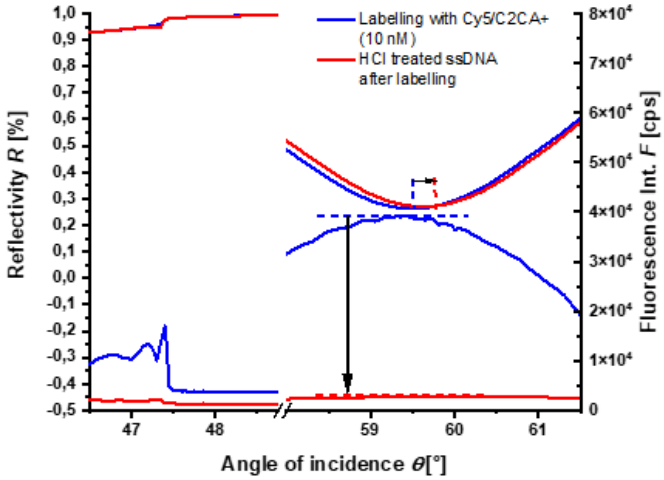

Figure 62: R(θ) and F(θ) showing the effect of HCl on Cy5/C2CA+ labelled ssDNA strands; c_{PLP} = 40 nM

NaOH

For testing the regeneration with c = 10 mM NaOH, the RCA product was labelled with the Cy5/DC+ accordion. The first time the Cy5/DC+ strands were rinsed (Cy5/DC_1 in Figure 63), a waveguide mode appeared in the angular reflectivity scan. NaOH (c = 10 mM) was flushed over the surface for 5 minutes in order to remove the labelled strands attached to the RCA product. The angular reflectivity scans $R(\theta)$ show a shift to lower angles of the plasmon dip $\Delta\theta = 0.3°$ and yielding a fluorescence intensity of $\Delta F_{PSP} = 1.3 \cdot 10^4$ cps after the first regeneration step measured in PBST.

In order to test how NaOH influenced the biointerface of the surface and to investigate if the result is reproducible, Cy5/DC+ is rinsed over the surface again (Cy5/DC_2 in Figure 63). The reflectivity curve in the plasmon mode shifted to lower angles compared to the first time, as it was already observed in the angular reflectivity scan $R(\theta)$ after NaOH. However, the fluorescence intensity only reached $\Delta F_{PSP} = 8.0 \cdot 10^4$ cps, which means it decreased by the factor 0.56. It can be observed that the waveguide mode at the critical angle becomes sharper and reaches a higher fluorescence value ΔF_W. The intensity of the waveguide mode increased by the factor 1.85, which was also already observed in the angular reflectivity scan $R(\theta)$ after regeneration. Additionally, the ratio of the value obtained for the plasmon mode ΔF_{PSP} to the waveguide mode ΔF_W is 1.58 for the first application of Cy5/DC+ and decreases to 0.48 after using NaOH. This is an indication that the thickness of the DNA layer increased but the conformation changed. The ssDNA strands are stretching away from the surface, which leads to less amount of fluorophores within the evanescent field of SPs.

Moreover, this procedure was repeated for one more time (Cy5/DC_3 in Figure 63). The result of the angular reflectivity scan $R(\theta)$ and $F(\theta)$ were quite similar to the outcome after the first regeneration step.

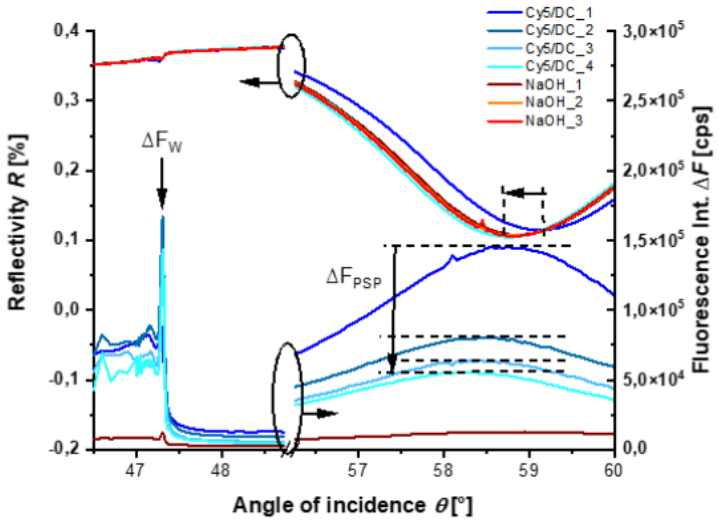

Figure 63: R(ϑ) for the investigation of repeatedly using NaOH on ssDNA strands by hybridizing Cy5/DC accordions after each regeneration step under identical conditions; c_{PLP} = 40 nM

The sensor chip was kept overnight in PBST at a lower flow rate (10.04 µL/min). The Cy5/DC+ accordion was again flushed to determine the change after about 12 hours (Cy5/DC_4 in Figure 63). The plasmon dip in the reflectivity curve $R(\theta)$ slightly shifted to lower angles $\Delta\theta$ = 0.1° and showed a fluorescence intensity of $\Delta F_{PSP} = 5.5 \cdot 10^4$ cps. Since the change was similar to the observations before, the chip was used for further experiments.

The background signal, which remained after each regeneration process, was deducted from the fluorescence intensity $\Delta F(\theta)$ of the Cy5/DC+ labelling. It can be concluded that the results are relatively reproducible only after rinsing with NaOH for the first time. The mean value and the standard deviation for the Cy5/DC+ could be determined for 3 repetitions in the waveguide mode as $\Delta F_W = 1.5 \cdot 10^5 \pm 1.4 \cdot 10^4$ cps, in the plasmon mode as $\Delta F_{PSP} = 6.6 \cdot 10^4 \pm 1.3 \cdot 10^4$ cps and for the ratio 0.43 ± 0.05 by excluding the data from the first labelling step (see Table 6). However, when introducing NaOH to the system after the first time, the baseline of the SPR response decreases slightly and the fluorescence value for the background increases after every step. This means that not all oligonucleotides are fully removed within 5 minutes.

Table 6: Summary of acquired data from angular reflectivity scans and calculation of mean and standard deviation

Number of Cy5/DC	**Waveguide mode ΔF_W [cps]**	**Plasmon mode ΔF_{PSP} [cps]**	**Ratio**
1	$9.1 \cdot 10^4$	$1.4 \cdot 10^5$	1,58
2	$1.7 \cdot 10^5$	$8 \cdot 10^4$	0,48
3	$1.4 \cdot 10^5$	$6.4 \cdot 10^4$	0,44
4	$1.5 \cdot 10^5$	$5.5 \cdot 10^4$	0,38
mean	$1.5 \cdot 10^5$	$6.6 \cdot 10^4$	0,43
Standard deviation	$1.4 \cdot 10^4$	$1.3 \cdot 10^4$	0,05

Particularly, with a large quantity of fluorescent dyes bound to the ssDNA strands, rinsing with NaOH for 5 minutes is not sufficient. It can be improved by prolonging the regeneration time. However, it should be noted that the surface is not completely regenerable after the chip has been used several times for different purposes. Therefore, the chip history needs to be considered.

6.7. Implementation of RCA to surface plasmon enhanced fluorescence

The padlock probe is circularized in the presence of the target analyte in the solution. It can then be captured by pre-immobilized complementary sequences on the surface. Subsequently, the RCA reaction is started in order to amplify the signal and improve the sensitivity of the plasmonic sensor. The PLP can be labelled with the Cy5/C2CA- sequence beforehand *ex-situ* since the molecular mass is often too small to create a shift in the angular reflectivity scans $R(\theta)$. The fluorescence intensity ΔF_{PSP} after immobilizing the PLP can be compared with the enhanced signal after the RCA reaction.

The different molar concentration of the PLP, which was labelled *ex-situ* with c = 10 nM Cy5/C2CA-, was flowed over the sensor surface after the attachment of the capturing sequence (biotin/20T/BS-) for 40 minutes. Afterwards, PBST was flushed and an angular reflectivity scan $R(\theta)$ was conducted. The RCA conditions were kept the same for all experiments and the RCA product was labelled with c = 10 nM of Cy5/C2CA+ for 15 minutes. The fluorescence intensity ΔF_{PSP} at the surface plasmon resonance dip of the angular reflectivity scans $R(\theta)$ after PLP addition and labelling of the ssDNA strands are compared (see Figure 64).

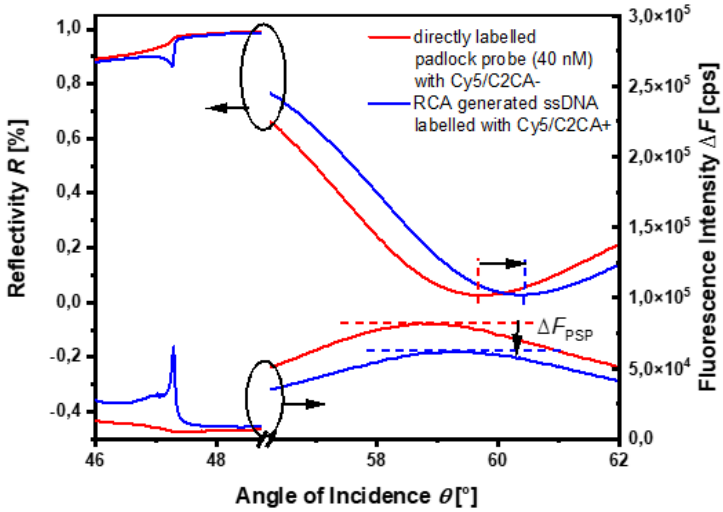

Figure 64: R(ϑ) after the incubation with the Cy5/C2CA- pre-labelled padlock probe (c_{PLP} = 40 nM) captured by the biotinylated BS- sequence on the surface in comparison to the RCA generated ssDNA chains labelled with Cy5/C2CA+

For the directly labelled PLP reacted with the surface from the solution with c_{PLP} = 40 nM and c_{PLP} = 4 nM, the fluorescence intensity ΔF_{PSP} is significantly higher than for the Cy5/C2CA+ labelled RCA product (see Figure 65). At lower molar concentrations, the labelling of the long ssDNA strands has a greater effect. It seems the concentration with c_{PLP} = 400 pM is the turning point at which the fluorescence intensity ΔF_{PSP} for the PLP and the RCA product are similar. Higher molar concentrations reduce the effectiveness of the amplification while at lower molar concentrations than c_{PLP} = 400 pM, the amplification improves the sensitivity of the sensor. This fact proves that the RCA reaction is effectively improving the detection limit of the assay.

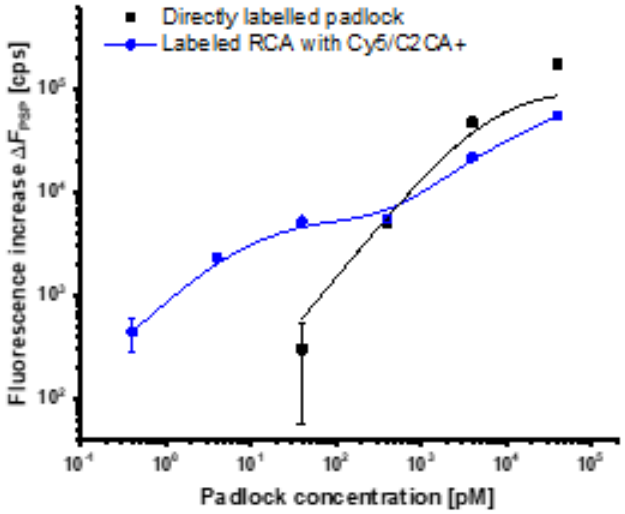

Figure 65: Comparison of fluorescence intensity at different padlock concentrations for the directly labelled padlock probe with Cy5/C2CA- (black) and the RCA generated ssDNA chains labelled with Cy5/C2CA+ (blue), data points extracted from the surface plasmon mode

The results illustrated in Figure 65 for high molar concentrations of PLP can be explained by the fact that the PLP with the diameter of about 10 nm is closer to the surface and thus in the region of the exponentially decaying field with stronger field intensity. The high sensor response is probably the result of that the PLP with dyes are located at the right distance. The RCA product takes the brush conformation at high PLP concentrations, of which the PSP field probes only a small part. In addition, it makes it harder for the Cy5/C2CA+ oligonucleotides to diffuse inside the polymer structure leading to an uneven distribution of the fluorophores within the ssDNA layer. Hence, many hybridization sequences are vacant, especially close to the surface. Furthermore, it needs to be considered that the labelling sequence is only applied for 15 minutes and is usually far from saturation in the brush regime. However, the region of interest is the low-density regime, which need to be investigated for sensitive techniques. At

lower molar concentrations, the density of the RCA product decreases and the brushes probably adapt a rather mushroom-like structure according to the sparser packed ssDNA strands (see Figure 66). In this conformation there are more dyes located below 100 nm, within the strong evanescent field.

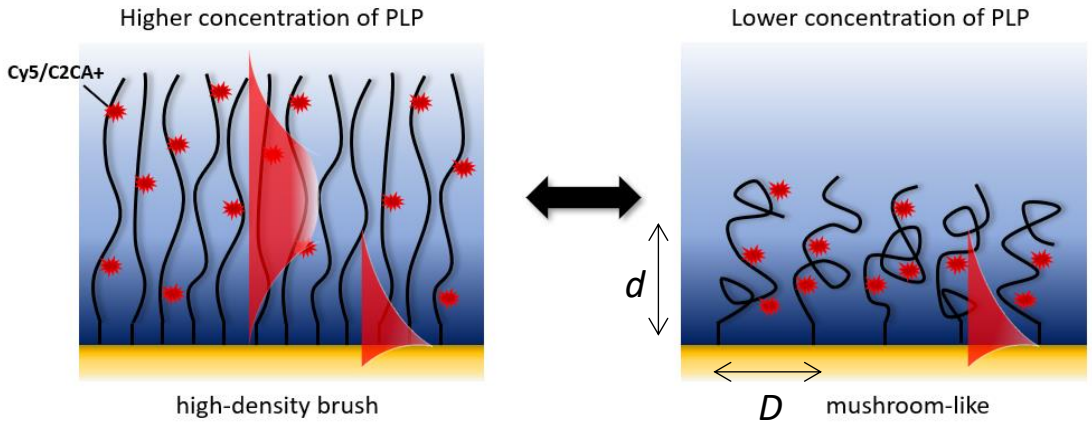

Figure 66: Schematic drawing of closely and sparsely packed fluorophore labelled ssDNA

The padlock sequence has a length of 52.65 nm with 0.65 nm per nucleotide and 81 bases. Therefore, the stretched strand of a brush of a high-density architecture has the possibility to bind to Cy5/C2CA+ about 2 times below 100 nm. However, it is assumed that due to diffusion and high density many of the binding sides are empty. This results in less intense fluorescence ΔF_{PSP}, even though the brush can have a thickness in micrometer range, which can be seen in the waveguide feature. Since ssDNA strands with lower density, have space to fold to some extent closer towards the surface and do not hinder the dye to diffuse inside the polymer structure, more fluorescent dyes are located within the evanescent field.

6.8. Implementation of RCA to microarrays with fluorescence readout

The assay for the detection of the padlock probe can be implemented in a microarray format to subsequently achieve simultaneous detection of multiple samples. This changes the *in-situ* assay with a constant flow for detecting one spot to a static microarray with spotted probes and washing and drying steps between the immobilization procedures.

The initial experiment was conducted to test the optimal molar concentration $c_{biotin/20T/TS-}$ of the capture oligonucleotide (biotin/20T/TS-) functionalized on the microarray, which was reacted to PLP for RCA. It was found that the optimum density was achieved by using molar concentrations $c_{biotin/20T/TS-}$ between 75 nM and 600 nM, which was optimized by Yasaman Ahmadi. For this purpose, a dilution series starting with $c_{biotin/20T/TS-}$ = 10 µM by the factor 1:2

was tested until $c_{biotin/20T/TS-}$ = 9 nM with 7-15 pmol and 35-83 pmol of circular padlock probe. Interestingly, spotted $c_{biotin/20T/TS-}$ > 600 nM showed a gradually decreasing lower fluorescence intensity Δ*F* after amplification by RCA and simultaneous labelling. Thus, it can be concluded that the binding must be sterically hindered.

The previously tested affinity interaction approaches, which were tested on the plasmonic sensor for enhancement purposes, for different amount of padlock probe were investigated. Therefore, the guiding sequence Biotin/20T/11TS+ and the capture sequence Biotin/20T/BS- were affinity bound via the neutravidin-biotin system in a ratio of 1:1 and a molar concentration of 150 nM. As comparison, experiments with the randomized guiding sequence (*c* = 150 nM) and only the capture sequence ($c_{biotin/20T/BS-}$ = 150 nM) were conducted. Additionally, the labelling of the RCA product with Cy3/C2CA+ oligos and the compaction with Atto532/BA+ were studied. The hybridization of the fluorophore bound oligonucleotides were applied during the 1.5 hours of the enzymatic reaction.

The control experiment was the hybridization of Cy3/TS+ to the complementary biotin/20T/TS-, which were bound to the microarray. In addition, a biointerface modified with biotin/20T/BS- and spotted with different PLP concentrations, was used as control for the RCA reaction since no polymerase was added to the chamber.

The ligated and exonuclease treated padlock probe with a molar concentration of c_{PLP} = 40 nM was diluted, from which 0.5 µL were spotted on a modified gold surface. After the RCA reaction, the microarray slide was imaged in the green channel (see Figure 67). The minimum amount of padlock probe, which showed a fluorescence intensity Δ*F* was n_{PLP} = 2 fmol.

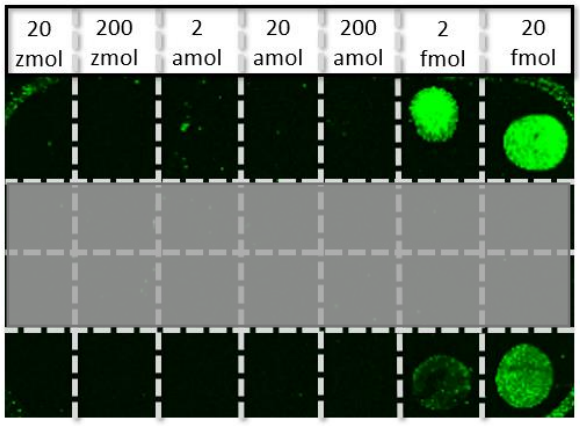

Figure 67: Imaged microarray after RCA with different padlock probe concentrations for the surface coated with biotin/20T/BS-, ssDNA labelled with Cy3/C2CA+; the first and last row are repetitive

Figure 68 represents the acquired fluorescence intensities for all tested biointerfaces by the software program ImageJ. Interestingly, the modified interface with the randomized guiding sequence showed the highest response for n_{PLP} = 20 fmol. In this case, only half of the attached oligonucleotides were prolonged by the polymerase, indicating that due to steric hinderance, the RCA worked more efficiently. Therefore, lower concentrations of biotin/20T/BS- probably ends up in a higher fluorescence intensity Δ*F*, since more binding sites are available for the PLP and the steric blocking is eliminated. However, the addition of Atto532/BA+ and the tethering sequence 11TS+ were not able to enhance the fluorescence intensity Δ*F*, as was the case on the plasmonic sensor.

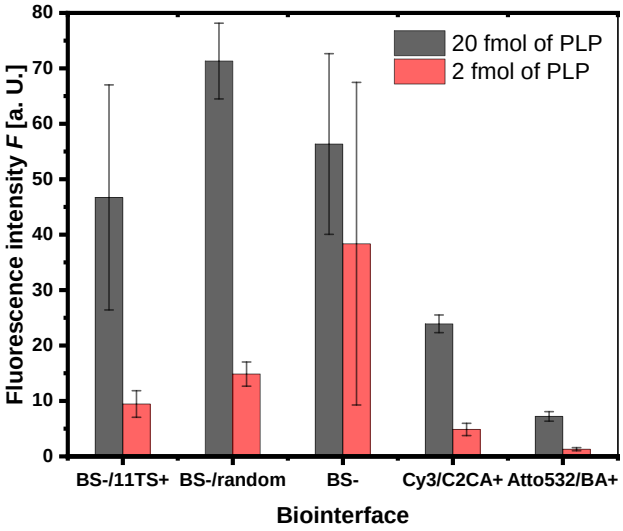

Figure 68: Comparison of the fluorescence intensity from different biointerfaces, tested on microarrays, for cPLP = 20 fmol (grey bars) and cPLP = 2 fmol (red bars)

The spotted areas are approximately 2 mm in size. Hence, the theoretical distances of the individual ssDNA chains can be derived for n_{PLP} = 20 fmol with D = 17.3 nm and for n_{PLP} = 2 fmol with D = 54.8 nm.

6.8.1. Drying and reswelling of DNA brushes

The microscope slides were spotted with different molar concentrations of biotin/20T/TS- by Yasaman Ahmadi. The slides were incubated with two different concentrations of PLP overnight, respectively. After the RCA reaction, the microarrays were washed two times in PBST, shortly with NFW and dried for 4 minutes with a centrifuge. Then the slides were imaged with the confocal fluorescence microscope in contact with air and in the swollen state in water. The images for the $c_{biotin/20T/TS-}$ = 1.25 µM, 2.5 µM and 5 µM are shown in Figure 69,

which is an imaged microarray chip with RCA grown ssDNA. It shows bright individual spots in case of the dried chip, which might be the result of agglomerates.

The acquired image of the RCA-generated strands in an aqueous environment shows an 11 times higher fluorescence intensity ΔF for the n_{PLP} = 35-83 pmol than in contact with air after the deduction of the background noise. For n_{PLP} = 7-15 pmol this factor increases to 50-84 times. The pictures of the dried ssDNA strands with lower concentration of PLP, show only very low fluorescence due to the decreased density of the brushes, resulting in less agglomerates compared to the high number of PLP. Therefore, the fluorescence of the swollen brushes has a higher enhancement factor. The fluorophores are quenched, when the chip is in contact with air, due to the collapse of the ssDNA to a thin layer while drying. The brushes are forced to stretch away from the sensor surface, gaining enough distance to avoid the quenching effect.

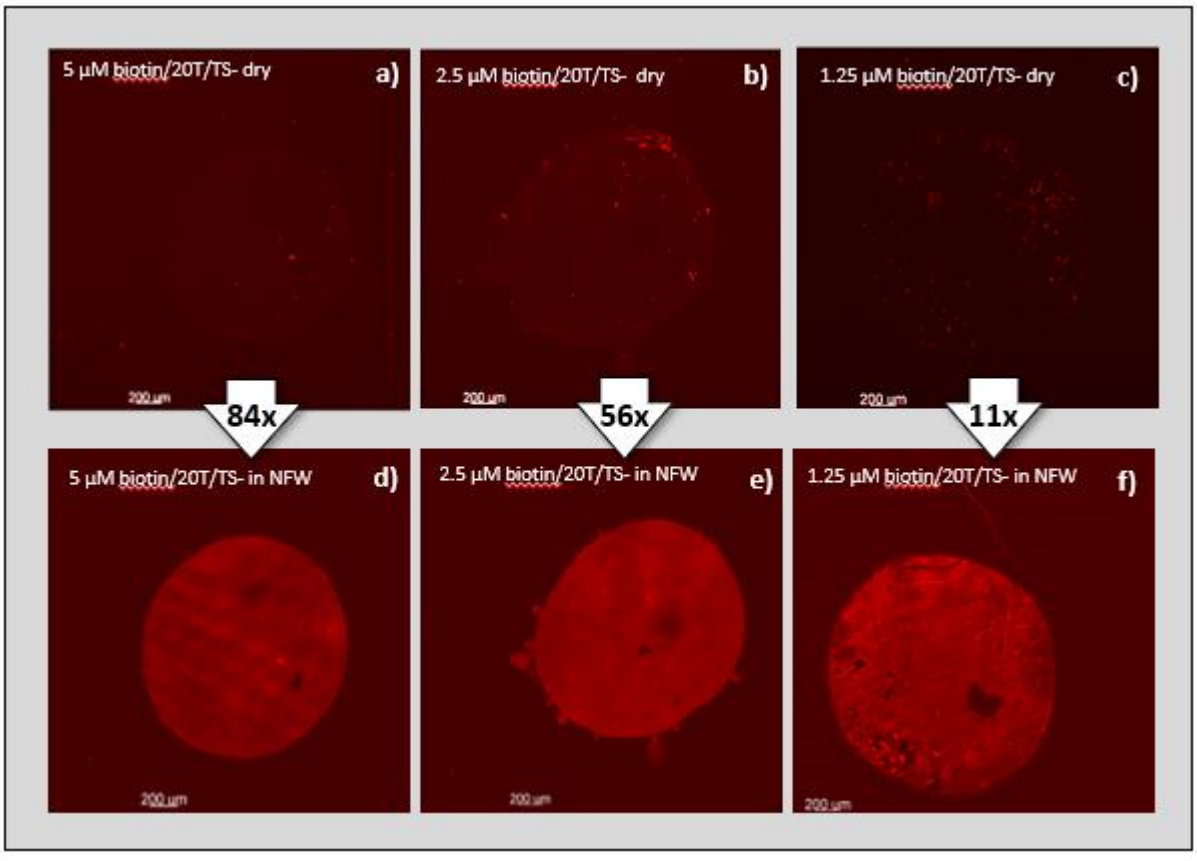

Figure 69: Images of the microarray acquired from the confocal fluorescence microscope with 35-83 pmol of PLP a)-c) chip in contact with air; d)-f) in contact with water

6.9. Implementation of RCA to fluorescence microscopy

Single molecule detection systems are usually based on the compartmenting for providing individual reaction chambers. The RCA reaction from one end tethered ssDNA strands eliminates the need of the tedious work to create separate chambers. In order to achieve the imaging of individual spots, establishing the mushroom regime of the polymer chains is necessary.

The high amount of padlock probes used for the plasmonic sensor results in a thick polymer layer (d_{ssDNA} > 1 µm), which has already been shown (Chapter 6.2.). This probably highly entangled network can already support multiple waveguide modes after only 1 hour of amplification reaction. The sensor surface has been investigated with a confocal fluorescence microscope after the growth of the brushes and the hybridization to Cy5/C2CA+.

Figure 70 shows the ssDNA structure after drying in contact with air in the red fluorescence channel and as comparison with white light. The used padlock concentration was 40 pM. The image acquired in the white light (Figure 70) b) shows many crystal structures, which is a result of dried PBST. Nevertheless, the fluorescence channel reveals the fluorescent labelled DNA structure, which is only present in the chamber and not where the gasket was placed (Figure 70)a). As can be seen from the 40x magnified Figure 70) c), the ssDNA forms an interconnected layer, where one area has been torn out (due to removing the chamber) and overlaps with another area. The flow also seems to influence the growth of the strands, since there is no fluorescence detected in the middle of the chamber where the flow should be the highest.

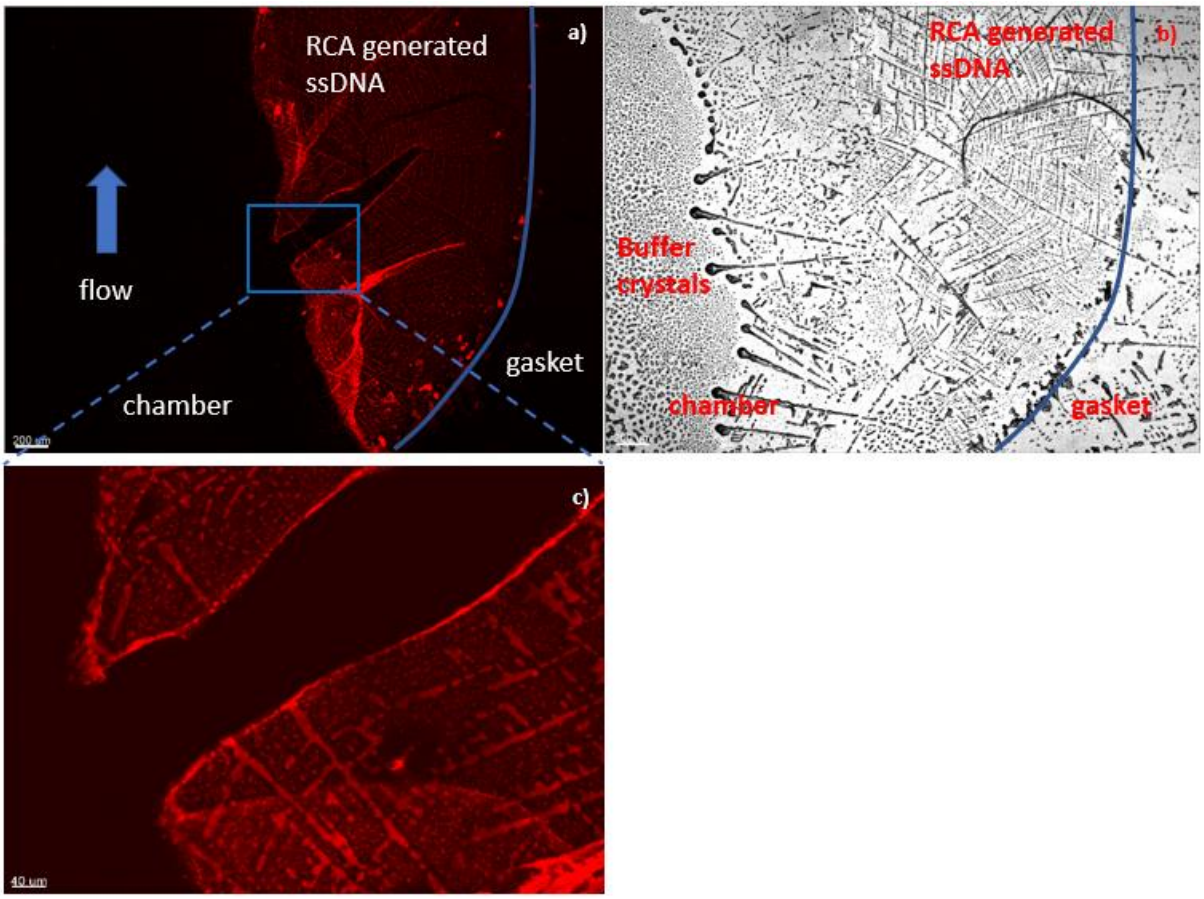

Figure 70: RCA generated ssDNA from c_{PLP} = 40 pM in contact with air after labelling with Cy5/C2CA+; a) 4 times magnification of chamber and gasket in the red fluorescent channel; b) 4 times magnification of the same spot of sensor surface as in image a) in white light; c) 40 times magnification of chamber

The molar concentration of the PLP has been further reduced, to the regime where the individual chains should not influence each other anymore. The individual chains are standing alone, leading to a coiled conformation. In order to prevent the formation of salt crystals, the sensor chip, after the growth of the ssDNA chains, was not dried but immediately imaged with the fluorescence microscope in PBST with a cover slide.

Images are shown in Figure 71 a) – d) for molar concentrations of c_{PLP} = 40 pM to c_{PLP} = 40 fM. As already discussed before, the highest concentration has a high density, forming a network where no individual chains can be observed. The images show that the structure is formed in the direction of the flow, indicating a rather soft gel-like conformation.

By reducing the molar concentration, individual spots appear. There are locally confined dyes, which enhances the intensity of the spot. The direction of the flow can be seen in each image from the tendency of the collective stretching of the ssDNA in a certain direction. Some spots are more spread, leading to a reduced brightness. It also needs to be considered, that the length of the ssDNA is calculated with 14100 nt for 1 hour of RCA reaction. However, the actual

size varies over a certain size range. Therefore, some spots might be less bright than others due to a smaller number of binding sides available for the complementary sequence with the fluorescence dye.

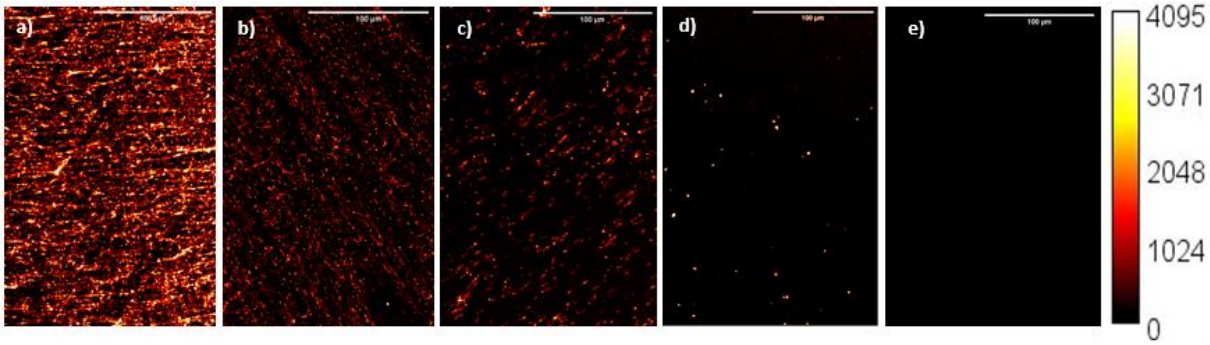

Figure 71: Fluorescence images from the red channel acquired by confocal fluorescence microscopy after RCA and labelling with Cy5/C2CA+ and Cy5/BA+ for a) c_{PLP} = 40 pM; b) c_{PLP} = 4 pM; c) c_{PLP} = 400 fM; d) c_{PLP} = 40 fM; e) control without PLP (scale bar for 100 µm)

The images acquired from the fluorescence microscope (Figure 72) a) were processed with the ImageJ software. Firstly, the threshold was adjusted in order to set the intensity of each spot with a high enough brightness to the same level (Figure 72) b). Then all spots were counted by the program (Figure 72) c). Spots with a larger area than 10 µm² were excluded. The process is shown for the RCA generated ssDNA chains with c_{PLP} = 400 fM.

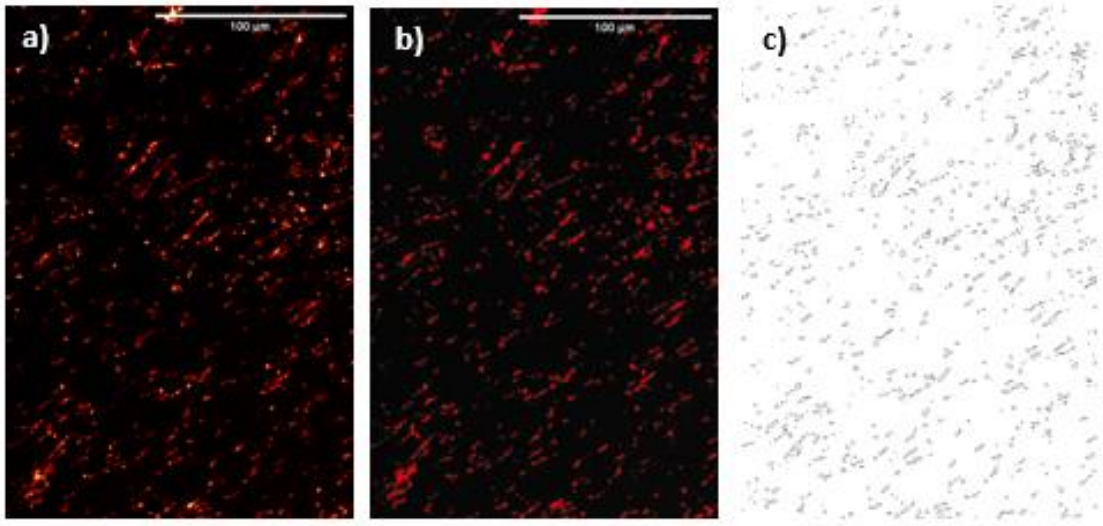

Figure 72: ImageJ analysis by a) using the original file for b) determining the colour threshold and c) counting the single particles of RCA generated ssDNA from c_{PLP} = 400 fM (scale bar for 100 µm)

By dividing the measured size of the image excerpt by ImageJ with the number of counted spots, a radial area of each individual spot could be determined. The average distance between the individual chains could be derived from the root of the spot area. The results are matching with the previous acquired data from the SPR and SPFS measurements (see Figure 73). For c_{PLP} = 4 pM the average distance was calculated with D = 3.2 µm, for c_{PLP} = 400 fM with D = 6 µm and for c_{PLP} = 40 fM with D = 2.6 µm.

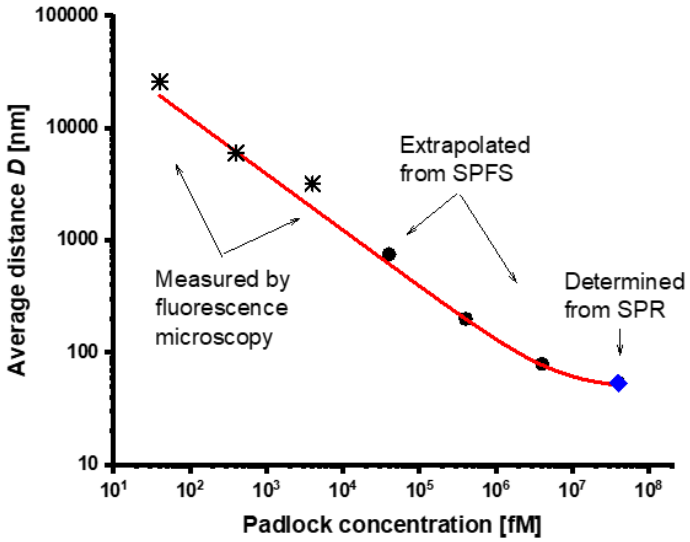

Figure 73: Overall summary of results, showing the measurable padlock concentrations for SPR (blue dot), SPFS (black dots) and the confocal fluorescence microscope (black stars)

Measurements with the PEF method demonstrated, that the directly labelled padlock probe with the complementary sequence showed a detectable fluorescence intensity ΔF_{PSP} for only approximately $c_{PLP} > 40$ pM. The sensitivity can be improved by increasing the molecular mass on the sensor surface and the number of available labeled sites by the RCA reaction, reaching a limit at about $c_{PLP} > 4$ pM.

The calibration curve (black curve in Figure 74), showing the data for the direct labelled padlock probe, saturates at a molar concentration of $c_{PLP} > 40$ nM. By the intersection with the 3 times standard deviation of the baseline noise $3*\sigma(F_{PSP})$ = 200 cps, the limit of detection LOD = 13 pM could be determined. After the amplification process of the anchored ssDNA and the hybridization to the labelling sequences, the calibration shows a rather peculiar progression, indicating a more complicated behavior (Figure 65).

From Figure 74 it can be concluded that the tethering approach does not have an effect in the higher density regime of the brush (red squares) with molar concentration of the padlock probe $c_{PLP} > 0.1$ nM. Due to the densely packed network, it is not possible for the ssDNA to hybridize to the guiding strands on the surface since they are stretched too far away. The direct labelling of the circular padlock produces a higher surface plasmon enhanced fluorescence intensity ΔF_{PSP}. However, in the dense brush-regime, an additional feature ascribed to an optical waveguide at the position of the critical angle was observed.

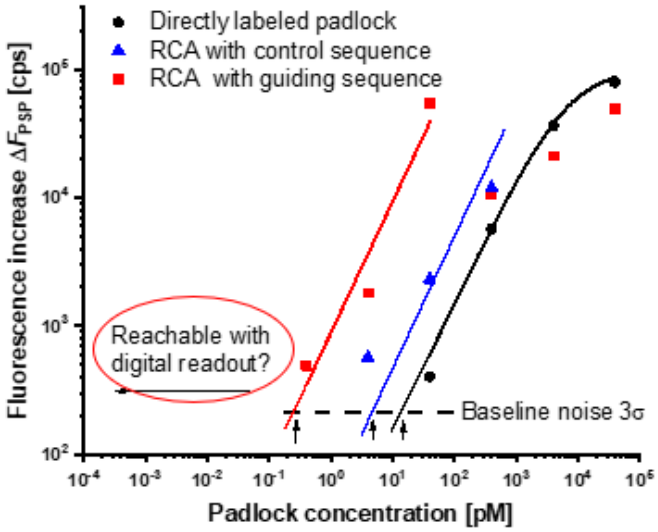

Figure 74: Comparison of detected fluorescence intensities acquired from the angular reflectivity scans of biointerfaces with randomized oligonucleotide (blue), guiding sequence (red) and the directly labelled padlock probe (black)

At lower molar concentration of the padlock probe c_{PLP} < 0.1 nM the fluorescence intensity ΔF_{PSP} is substantially higher for the RCA generated ssDNA than the response obtained after the direct labelled PLP. This observation can be ascribed to the preferred mushroom-like conformation at lower densities. From the experimentally obtained amplification rate, the RCA strand should be 14100 nt long after 60 minutes. Since the padlock probe contains 81 nt, there should be 174 binding sides available for the Cy5/C2CA+ to hybridize and to attach to the surface via the guiding oligos. Therefore, the fluorescence intensity ΔF_{PSP} is estimated to be enhanced maximum 174 times compared to the direct hybridization of the circular padlock. However, the ideal case is not probable due to steric hinderance or the fact that not all binding sites will be occupied. The stretching of the long ssDNA chains can also have an influence on this factor. Therefore, the amplification improved the fluorescence intensity only by a factor of 50. This effect can be ascribed to the optimum position of the emitters towards the gold surface due to the guiding of the strands along the interface. The fluorophores are strongly enhanced by the high intensity of the evanescent field, but the distance to the gold is high enough in order to prevent the quenching effect.

Overall, it can be concluded that the guiding of the ssDNA on the surface improves the sensitivity and allows a lower limit of detection of LOD = 260 fM. By imaging the sensor surface with a confocal fluorescence microscope for counting of individual spots, the LOD can be pushed even further to lower molar concentrations below pM. This implementation allows the combination of a digital read-out system.

7. Summary and Outlook

Rolling circle amplification (RCA) has paved the way towards several ultrasensitive fluorescence-based methods serving for the analysis of trace amounts of molecular analytes.[48] Over last years, there has been dominantly utilized fluorescence-based detection of the RCA-generated long ssDNA strands that are employed as tags associated with the presence of target molecule in the analyzed sample. The fact that these long ssDNA chains can be decorated with high number of fluorophore labels per target analyte allowed for facile discriminating of individual binding events of target analyte molecules on the surface and establishing of the Poisson statistics-based readout referred to as 'digital assays'. These platforms were implemented for both immunoassays[58] as well as for nucleic acid assays[145]. In general, such operation mode based on the counting of the individual molecules requires a well-controlled conformation of long ssDNA chains. They fold to generate compacted spots and thus enable clear discrimination of individual binding events.[145]

This thesis deals with several approaches to manipulate the up to 14 kb long RCA-generated ssDNA chains that are subsequently reacted with short fluorophore-labelled complementary sequences. The growth of the chains is *in situ* monitored by a combined SPR and SPFS read-out in order to investigate growth and conformation of long ssDNA chains altered by increasing the inter-chain distance, showing a transition from brush architecture to individual coiled DNA strands. When applied for the amplification of an assay where circular padlocks served as a model analyte, the fluorescence calibration curve with dual amplification (optical based on surface plasmon enhanced fluorescence – SPFS and enzymatic utilizing rolling circle amplification – RCA) was established. It revealed more complex dependence of the output optical signal on the analyte concentration compared to the regular SPFS format without the RCA enhancement step. This complex behavior was explained based on the conformation changes of several µm long ssDNA chains tethered to the surface taking either dense brush architecture (for high analyte concentration) or mushroom conformation (for low analyte concentrations). Importantly, in the low analyte concentration regime the ssDNA chains did only weakly interact with each other and were allowed to be located closer to the surface to distances matching the surface plasmon probing depths of about 100 nm. Indeed, the folding of ssDNA chains generated by RCA to then optimum distance range was possible to be controlled by using calcium ions leading to either the increase or decrease in the respective

fluorescence signal. When the chains are located at the distance of about 10-100 nm, the fluorescence signal can be efficiently enhanced by the coupling with the strong intensity of surface plasmon electromagnetic field. However, when the distance is pushed below 10 nm, the fluorescence signal is quenched. In addition, the possible manipulating of the chains by specific short ssDNA sequences serving as staples or surface anchors was explored for further compacting the ssDNA in the distance range that can be efficiently probed with confined surface plasmon field.

The efficient RCA reaction allowed for increasing the fluorescence signal associated with the affinity capture of ensemble of padlock molecules to the surface (with SPFS) as well as for the interrogation of individual sparsely attached ssDNA chains (with fluorescence microscopy). The possible analytical performance of SPFS for detection of the (model) analyte represented by the padlock was compared for direct labelling approach with the signal created by the RCA. The readout with SPFS method allowed to reach 13 pM limit of detection (LOD) for the direct labelling and by RCA improving it to 4 pM through the higher number of fluorophores present at the surface per captured analyte molecule. Moreover, advanced affinity-based plasmonic sensors were accomplished by using short DNA strands or pre-immobilized anchor sequences on the surface Through the effect of guiding the long ssDNA along the sensor surface by specific ssDNA staples, the LOD of the SPFS read-out was improved to 0.26 pM. Furthermore, we demonstrate that the sensitivity of the methods relying on ensemble detection can be advanced by spatially resolved detection. The counting of individual molecules has opened the door for achieving LOD at low fM concentrations when fluorescence microscopy is employed.

Merging the RCA with platforms offering plasmonic enhancement of fluorescence and imaging[146] represent future steps to new generation of fast *in situ* assays with digital readout that does not rely on multistep protocol. The developed means to control RCA on the metallic sensor surface holds great potential to serve as high throughput format supporting multiplexed assays. A possible implementation is sketched in Figure 75. The target sequence of the padlock probe can be exchanged with a marker sequence for detecting antibiotic resistance. Then, the padlock probe can be circularized by the presence of the target gene $bla_{\text{OXA-48}}$ in the patient sample, which marks the presence of the *β*-lactamase gene (as used in this work). Subsequently, it is introduced to the plasmonic sensor surface, which is

functionalized with respective capture sequences, and followed by the amplification with RCA reaction and the affinity binding of short oligonucleotide strands carrying fluorophore labels.

In general, the frequently occurring resistance genes represent a rising global threat to public health. Therefore, a rapid medical diagnosis is essential for the appropriate choosing of the adequate treatment of the patient. Conventional methods are laborious and time consuming which does not allow for obtaining results within a meaningful time. However, RCA - powered detection of target analytes represent a way to fulfil the requirement for both ultrasensitive and rapid analysis holding potential to address in part this increasingly important challenge.

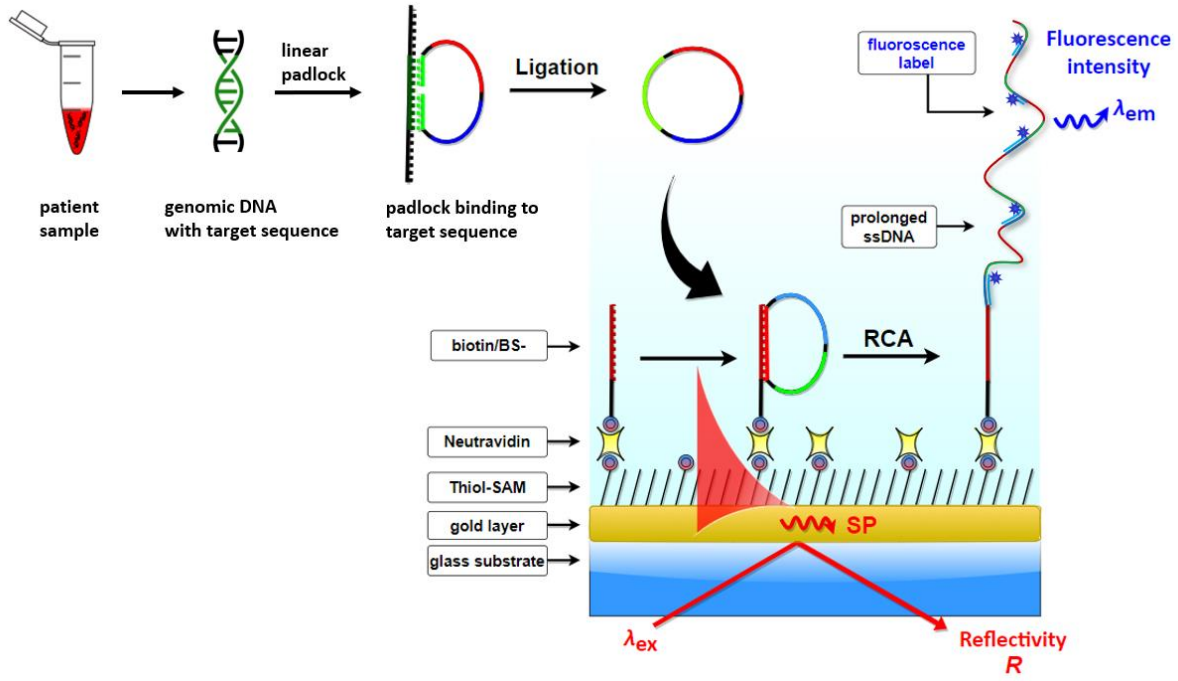

Figure 75: Concept for the use of the plasmonic biosensor for the detection of antibiotic resistant genes

Literature

1. Houdebine, L.-M. Transgenic Animal Models in Biomedical Research. *Methods in molecular biology (Clifton, N.J.)* **360**, 163–202 (2007).

2. Breaker, R. R. & Joyce, G. F. A DNA enzyme that cleaves RNA. *Chemistry & Biology* **1**, 223–229 (1994).

3. Rothemund, P. W. K. Folding DNA to create nanoscale shapes and patterns. *Nature* **440**, 297–302 (2006).

4. Barišić, I. *et al.* Multiplex detection of antibiotic resistance genes using padlock probes. *Diagnostic Microbiology and Infectious Disease* **77**, 118–125 (2013).

5. Wolff, N., Hendling, M., Schönthaler, S., Geiss, A. F. & Barišić, I. Low-cost microarray platform to detect antibiotic resistance genes. *Sensing and Bio-Sensing Research* **23**, 100266 (2019).

6. Pulido, M. R., García-Quintanilla, M., Martín-Peña, R., Cisneros, J. M. & McConnell, M. J. Progress on the development of rapid methods for antimicrobial susceptibility testing. *Journal of Antimicrobial Chemotherapy* **68**, 2710–2717 (2013).

7. Poon, L. L. *et al.* Sensitive and Inexpensive Molecular Test for Falciparum Malaria: Detecting Plasmodium falciparum DNA Directly from Heat-Treated Blood by Loop-Mediated Isothermal Amplification. *Clinical Chemistry* **52**, 303–306 (2006).

8. Mullis, K. *et al.* Specific Enzymatic Amplification of DNA In Vitro: The Polymerase Chain Reaction. *Cold Spring Harb Symp Quant Biol* 51: 263-273 (1986) doi:10.1101/SQB.1986.051.01.032.

9. Carter, I. *et al.* PCR Methodology. in *PCR for Clinical Microbiology: An Australian and International Perspective* (eds. Schuller, M., Sloots, T. P., James, G. S., Halliday, C. L. & Carter, I. W. J.) 11–47 (Springer Netherlands, 2010). doi:10.1007/978-90-481-9039-3_2.

10. Aaij, C. & Borst, P. The gel electrophoresis of DNA. *Biochimica et Biophysica Acta (BBA) - Nucleic Acids and Protein Synthesis* **269**, 192–200 (1972).

11. Essentials of Real-Time PCR. *ThermoFisher Scientific* https://www.thermofisher.com/at/en/home/life-science/pcr/real-time-pcr/real-time-pcr-learning-center/real-time-pcr-basics/essentials-real-time-pcr.html.

12. Basic Principles of RT-qPCR. *ThermoFisher Scientific* https://www.thermofisher.com/at/en/home/brands/thermo-scientific/molecular-biology/molecular-biology-learning-center/molecular-biology-resource-library/spotlight-articles/basic-principles-rt-qpcr.html.

13. Ali, M. M. *et al.* Rolling circle amplification: a versatile tool for chemical biology, materials science and medicine. *Royal Sociatey of Chemistry* (2013) doi:10.1039/c3cs60439j.

14. Zhao, W., Ali, M. M., Brook, M. A. & Li, Y. Rolling Circle Amplification: Applications in Nanotechnology and Biodetection with Functional Nucleic Acids. *Angewandte Chemie International Edition* **47**, 6330–6337 (2008).

15. Jarvius, J. *et al.* Digital quantification using amplified single-molecule detection. *Nature Methods* **3**, 725–727 (2006).

16. Hatch, A., Sano, T., Misasi, J. & Smith, C. L. Rolling circle amplification of DNA immobilized on solid surfaces and its application to multiplex mutation detection. *Genetic Analysis: Biomolecular Engineering* **15**, 35–40 (1999).

17. Cheglakov, Z., Weizmann, Y., Braunschweig, A. B., Wilner, O. I. & Willner, I. Increasing the Complexity of Periodic Protein Nanostructures by the Rolling-Circle-Amplified Synthesis of Aptamers. *Angewandte Chemie International Edition* **47**, 126–130 (2008).

18. Ke, R. *et al.* In situ sequencing for RNA analysis in preserved tissue and cells. *Nature Methods* **10**, 857–860 (2013).

19. Ng, P. C. & Kirkness, E. F. Whole Genome Sequencing. *Springer Link* **Genetic Variation**, 215–226 (2010).

20. Zankari, E. *et al.* Genotyping using whole-genome sequencing is a realistic alternative to surveillance based on phenotypic antimicrobial susceptibility testing. *Journal of Antimicrobial Chemotherapy* **68**, 771–777 (2013).

21. van El, C. G. *et al.* Whole-genome sequencing in health care. *European Journal of Human Genetics* **21**, 580–584 (2013).

22. Jackson, C. L. & Mehta, S. 29 - Molecular diagnostics in hematopathology. in *Rodak's Hematology (Sixth Edition)* (eds. Keohane, E. M., Otto, C. N. & Walenga, J. M.) 495–524 (Content Repository Only!, 2020). doi:10.1016/B978-0-323-53045-3.00038-6.

23. *Next-Generation Sequencing (NGS)*. https://www.thermofisher.com/at/en/home/life-science/sequencing/next-generation-sequencing.html.

24. Nanopore DNA sequencing. *Oxford Nanopore Technologies* https://nanoporetech.com/applications/dna-nanopore-sequencing.

25. Rampal, J. B. *Microarrays: Volume I: Synthesis Methods*. (Humana Press).

26. Munir, A. *et al.* Modeling Hybridization Kinetics of Gene Probes in a DNA Biochip Using FEMLAB. *Microarrays* (2017) https://doi.org/10.3390/microarrays6020009.

27. Miller, S., Karaoz, U., Brodie, E. & Dunbar, S. Solid and Suspension Microarrays for Microbial Diagnostics. in *Current and Emerging Technologies for the Diagnosis of Microbial Infections* vol. Chapter 11 395–431 (Elsevier Ltd., 2020).

28. Edwards, M. C. & Gibbs, R. Multiplex PCR: advantages, development, and applications. *PCR methods and applications* **3 4**, S65-75 (1994).

29. Banks, P. *Multiplexed Assays in the Life Sciences*. https://www.biotek.com/resources/white-papers/multiplexed-assays-in-the-life-sciences/ (2010).

30. Earley, M. C. *et al.* Report from a workshop on multianalyte microsphere assays. *Cytometry* **50**, 239–242 (2002).

31. *xMAP® – The World's Most Used Multiplexing Technology*. https://www.luminexcorp.com/xmap-technology/#overview.

32. *QUANSYS Q-Plex™ Array Technology*. https://www.oxfordbiosystems.com/Applications/Immunology/Quansys.

33. Elshal, M. F. & McCoy, J. P. Multiplex bead array assays: performance evaluation and comparison of sensitivity to ELISA. *Methods* **38**, 317–323 (2006).

34. Tighe, P. J., Ryder, R. R., Todd, I. & Fairclough, L. C. ELISA in the multiplex era: potentials and pitfalls. *Proteomics Clin Appl* **9**, 406–422 (2015).

35. Kingsmore, S. F. & Patel, D. D. Multiplexed protein profiling on antibody-based microarrays by rolling circle amplification. *Current Opinion in Biotechnology* **14**, 74–81 (2003).

36. Schweitzer, B. *et al.* Immunoassays with rolling circle DNA amplification: A versatile platform for ultrasensitive antigen detection. *Proc Natl Acad Sci USA* **97**, 10113 (2000).

37. Barišić, I. *et al.* Multiplex characterization of human pathogens including species and antibiotic-resistance gene identification. *J Med Microbiol* . 65(1):48–55. (2016) doi:10.1099/jmm.0.000192.

38. Zhang, Y. & Noji, H. Digital Bioassays: Theory, Applications, and Perspectives. *Anal. Chem.* **89**, 92–101 (2017).

39. Basu, A. S. Digital Assays Part I: Partitioning Statistics and Digital PCR. *SLAS TECHNOLOGY: Translating Life Sciences Innovation* **22**, 369–386 (2017).

40. Teh, S.-Y., Lin, R., Hung, L.-H. & Lee, A. P. Droplet microfluidics. *Lab Chip* **8**, 198–220 (2008).

41. Rondelez, Y. *et al.* Microfabricated arrays of femtoliter chambers allow single molecule enzymology. *National Center for Biotechnology Information* **Natur Biotechnology**, 23(3):361–5 (2005).

42. Ottesen, E. A., Hong, J. W., Quake, S. R. & Leadbetter, J. R. Microfluidic Digital PCR Enables Multigene Analysis of Individual Environmental Bacteria. *Science* **314**, 1464 (2006).

43. Tachibana, H. *et al.* Self-propelled continuous-flow PCR in capillary-driven microfluidic device: Microfluidic behavior and DNA amplification. *Sensors and Actuators B: Chemical* **206**, 303–310 (2015).

44. Baker, M. Digital PCR hits its stride. *Nature Methods* **9**, 541–544 (2012).

45. Kühnemund, M. *et al.* Sensitive and inexpensive digital DNA analysis by microfluidic enrichment of rolling circle amplified single-molecules. *Nucleic Acids Research* **45**, e59–e59 (2017).

46. Ciftci, S. *et al.* Digital Rolling Circle Amplification–Based Detection of Ebola and Other Tropical Viruses. *The Journal of Molecular Diagnostics* **22**, 272–283 (2020).

47. Henriksson, S. *et al.* Development of an in situ assay for simultaneous detection of the genomic and replicative form of PCV2 using padlock probes and rolling circle amplification. *Virol J* **8**, 37–37 (2011).

48. Lizardi, P. *et al.* Mutation detection and single-molecule counting using isothermal rolling-circle amplification. *Nature genetics* **19**, 225–232 (1998).

49. Kühnemund, M., Witters, D., Nilsson, M. & Lammertyn, J. Circle-to-circle amplification on a digital microfluidic chip for amplified single molecule detection. *Lab Chip* **14**, 2983–2992 (2014).

50. Krzywkowski, T., Kühnemund, M., Wu, D. & Nilsson, M. Limited reverse transcriptase activity of phi29 DNA polymerase. *Nucleic Acids Research* **46**, 3625–3632 (2018).

51. Hamidi, S. V., Ghourchian, H. & Tavoosidana, G. Real-time detection of H5N1 influenza virus through hyperbranched rolling circle amplification. *Analyst* **140**, 1502–1509 (2015).

52. Garbarino, F., Minero, G. A. S., Rizzi, G., Fock, J. & Hansen, M. F. Integration of rolling circle amplification and optomagnetic detection on a polymer chip. *Biosensors and Bioelectronics* **142**, 111485 (2019).

53. *Sandwich ELISA Protocol*. https://www.leinco.com/sandwich-elisa-protocol/.

54. *Scientific Principle of Simoa™ (Single Molecule Array) Technology*. 2 https://pathbio.med.upenn.edu/hic/site/wp-content/uploads/2017/08/Simoa-Technologyl.pdf.

55. Basu, A. S. Digital Assays Part II: Digital Protein and Cell Assays. *SLAS TECHNOLOGY: Translating Life Sciences Innovation* **22**, 387–405 (2017).

56. Rissin, D. M. *et al.* Single-molecule enzyme-linked immunosorbent assay detects serum proteins at subfemtomolar concentrations. *Nature biotechnology* **28**, 595–599 (2010).

57. Akama, K. *et al.* Wash- and Amplification-Free Digital Immunoassay Based on Single-Particle Motion Analysis. *ACS Nano* **13**, 13116–13126 (2019).

58. Pérez-Ruiz, E. *et al.* Digital ELISA for the quantification of attomolar concentrations of Alzheimer's disease biomarker protein Tau in biological samples. *Analytica Chimica Acta* **1015**, 74–81 (2018).

59. *Overview - Antibiotics*. https://www.nhs.uk/conditions/antibiotics/ (2019).

60. Levy, S. *The Antibiotic Paradox*. (Perseus Publishing, 2002).

61. Fleming, A. On the Antibacterial Action of Cultures of a Penicillium, with Special Reference to Their Use in the Isolation of B. influenzae. *Reviews of Infectious Diseases* **2**, 129–139 (1980).

62. Gould, K. Antibiotics: from prehistory to the present day. *Journal of Antimicrobial Chemotherapy* (2016) https://doi.org/10.1093/jac/dkv484.

63. *Antibiotic resistance - Antibiotics*. https://www.nhs.uk/conditions/antibiotics/antibiotic-antimicrobial-resistance/ (2019).

64. *Antibiotic resistance*. https://www.who.int/news-room/fact-sheets/detail/antibiotic-resistance (2020).

65. Bush, K. & Jacoby, G. A. Updated Functional Classification of β-Lactamases. *American Society for Microbiology - Antimicrobial Agents and Chemotherapy* (2010) doi:10.1128/AAC.01009-09.

66. Tooke, C. L. *et al.* β-Lactamases and β-Lactamase Inhibitors in the 21st Century. *Journal of Molecular Biology* (2019) doi: 10.1016/j.jmb.2019.04.002.

67. *Antibiotic / Antimicrobial Resistance (AR / AMR) - How Antibiotic Resistance Happens*. https://www.cdc.gov/drugresistance/about/how-resistance-happens.html (2020).

68. van Belkum, A. *et al.* Developmental roadmap for antimicrobial susceptibility testing systems. *Nature Reviews Microbiology* **17**, 51–62 (2019).

69. Bauer, K. A., Perez, K. K., Forrest, G. N. & Goff, D. A. Review of Rapid Diagnostic Tests Used by Antimicrobial Stewardship Programs. *Clinical Infectious Diseases* **Volume 59, Issue suppl_3**, 134–145 (2014).

70. Reller, L. B., Weinstein, M., Jorgensen, J. H. & Ferraro, M. J. Antimicrobial Susceptibility Testing: A Review of General Principles and Contemporary Practices. *Clinical Infectious Diseases* **Volume 49 Issue 11**, 1749–1755 (2009).

71. Case, R. J. *et al.* Use of 16S rRNA and rpoB Genes as Molecular Markers for Microbial Ecology Studies. *American Society for Microbiology - Applied and Environmental Microbiolgy* (2006) doi:10.1128/AEM.01177-06.

72. Optical Biosensors. in *Introduction to Biophotonics* 311–356 (John Wiley & Sons, Ltd, 2003). doi: 10.1002/0471465380.ch9.

73. Banica, F.-G. *Chemical Sensors and Biosensors: Fundamentals and Applications*. (A John Wiley & Sons, Ltd., Publication, 2012).

74. Yüce, M. & Kurt, H. How to make nanobiosensors: surface modification and characterisation of nanomaterials for biosensing applications. *RSC Adv.* **7**, 49386–49403 (2017).

75. Diamond, D. Principles of Chemical and Biological Sensors. *John Wiley & Sons* (1998).

76. Erkey, C. Chapter 4 - Thermodynamics and Dynamics of Adsorption of Metal Complexes on Surfaces from Supercritical Solutions. in *Supercritical Fluid Science and Technology* (ed. Erkey, C.) vol. 1 41–77 (Elsevier, 2011).

77. 6 - Studying molecular-scale protein–surface interactions in biomaterials. in *Characterization of Biomaterials* (eds. Jaffe, M., Hammond, W., Tolias, P. & Arinzeh, T.) 182–223 (Woodhead Publishing, 2013). doi:10.1533/9780857093684.182.

78. Keil, R. G. & Mayer, L. M. 12.12 - Mineral Matrices and Organic Matter. in *Treatise on Geochemistry (Second Edition)* (eds. Holland, H. D. & Turekian, K. K.) 337–359 (Elsevier, 2014). doi:10.1016/B978-0-08-095975-7.01024-X.

79. T., V. D. & B., C. Biosensors and Biochips: Advances in Biological and Medical Diagnostics. *Fresenius J Anal Chem* 540–551 (2000) http://doi.org/10.1007/s002160051549.

80. Ratner, B. D. & Hoffman, A. S. Chapter I.2.12 - Physicochemical Surface Modification of Materials Used in Medicine. in *Biomaterials Science (Third Edition)* (eds. Ratner, B. D., Hoffman, A. S., Schoen, F. J. & Lemons, J. E.) 259–276 (Academic Press, 2013). doi:10.1016/B978-0-08-087780-8.00027-9.

81. Holzinger, M., Le Goff, A. & Cosnier, S. Nanomaterials for biosensing applications: a review. *Frontiers in Chemistry* **2**, 63 (2014).

82. Avidin, NeutrAvidin and Streptavidin Conjugates—Section 7.6. *ThermoFisher Scientific* https://www.thermofisher.com/at/en/home/references/molecular-probes-the-handbook/antibodies-avidins-lectins-and-related-products/avidin-streptavidin-neutravidin-and-captavidin-biotin-binding-proteins-and-affinity-matrices.html.

83. García-Aljaro, C., Muñoz, F. X. & Baldrich, E. Captavidin: a new regenerable biocomponent for biosensing? *Analyst* **134**, 2338–2343 (2009).

84. MORAG, E., BAYER, E. A. & WILCHEK, M. Reversibility of biotin-binding by selective modification of tyrosine in avidin. *Biochemical Journal* **316**, 193–199 (1996).

85. Kim, M., Schmitt, S. K., Choi, J. W., Krutty, J. D. & Gopalan, P. From Self-Assembled Monolayers to Coatings: Advances in the Synthesis and Nanobio Applications of Polymer Brushes. *Polymers* **7(7)**, 1346–1378 (2015).

86. Sweat, D. P., Kim, M., Yu, X. & Gopalan, P. A single-component inimer containing cross-linkable ultrathin polymer coating for dense polymer brush growth. *Langmuir* 29(11):3805–12 (2013) doi:10.1021/la305060z.

87. Matyjaszewski, K., Dong, H., Jakubowski, W., Pietrasik, J. & Kusumo, A. Grafting from Surfaces for "Everyone": ARGET ATRP in the Presence of Air. *Langmuir* **23**, 4528–4531 (2007).

88. Rastogi, A., Paik, M. Y., Tanaka, M. & Ober, C. K. Direct patterning of intrinsically electron beam sensitive polymer brushes. *ACS Nano* **4(2):771-80**, (2010).

89. Wattendorf, U. & Merkle, H. P. PEGylation as a tool for the biomedical engineering of surface modified microparticles. *Journal of Pharmaceutical Sciences* **97**, 4655–4669 (2008).

90. Zadegan, R. M. & Norton, M. L. Structural DNA Nanotechnology: From Design to Applications. *International Journal of Molecular Sciences* **13**, (2012).

91. Clausson, C.-M. *et al.* Compaction of rolling circle amplification products increases signal integrity and signal-to-noise ratio. *Scientific Reports* **5**, 12317 (2015).

92. Masel, R. I. *Principles of Adsorption and Reaction on Solid Surfaces*. (Wiley, 1996).

93. Biacore Assay Handbook 29-0194-00 Edition AA. (2015).

94. Regeneration strategies for Streptavidin biosensors on the Octet platform - Developing a successful regeneration protocol.

95. Price, N., Dwek, R., Ratcliffe, R. & Wormald, M. *Principles and Problems in Physical Chemistry for Biochemists*. (Oxford University Press, 2001).

96. Paschotta, R. *Refractive Index*. https://www.rp-photonics.com/refractive_index.html.

97. Parry-Hill, M. J., Sutter, R. T., Fellers, T. J. & Davidson, M. W. *Refraction of Light*. https://www.olympus-lifescience.com/en/microscope-resource/primer/lightandcolor/refractionhome/.

98. *Optical Fiber Working and Its Applications*. https://www.elprocus.com/optical-fiber-working-and-its-applications/.

99. Moreno, I., Paez, G. & Strojnik, M. Dove Prism with Increased Throughput for Implementation in a Rotational-Shearing Interferometer. *Applied optics* **42**, 4514–21 (2003).

100. Prasad, P. N. *Nanophotonics*. (Wiley-Interscience, 2004).

101. Obodovskiy, I. Chapter 12 - Luminescence. in *Radiation* (ed. Obodovskiy, I.) 207–220 (Elsevier, 2019). doi:10.1016/B978-0-444-63979-0.00012-4.

102. Albani, J. R. Chapter 2 - Fluorescence: Principles and Observables. in *Structure and Dynamics of Macromolecules: Absorption and Fluorescence Studies* (ed. Albani, J. R.) 55–98 (Elsevier Science, 2004). doi:10.1016/B978-044451449-3/50002-2.

103. Characteristics of Fluorescence Emission. in *Molecular Fluorescence* vol. Molecular Fluorescence: Principles and Applications 53–74 (John Wiley & Sons, Ltd).

104. Davidson, M. W. *et al. Fluorescence Microscopy - Basic Concepts in Fluorescence*. https://micro.magnet.fsu.edu/primer/techniques/fluorescence/fluorescenceintro.html (2015).

105. Abramowitz, M., Johnson, I. D., Parry-Hill, M. J., Flynn, B. O. & Davidson, M. W. *Brief Overview of Fluorescence*. https://www.olympus-lifescience.com/en/microscope-resource/primer/lightandcolor/fluorescencehome/.

106. Singh, S. *et al.* 2D Nanomaterial-Based Surface Plasmon Resonance Sensors for Biosensing Applications. *Micromachines* **11**, (2020).

107. Homola, J. Surface Plasmon Resonance Sensors for Detection of Chemical and Biological Species. *Chem. Rev.* **108**, 462–493 (2008).

108. Kretschmann, E. Die Bestimmung optischer Konstanten von Metallen durch Anregung von Oberflächenplasmaschwingungen. *Zeitschrift für Physik A Hadrons and nuclei* **241**, 313–324 (1971).

109. Otto, A. Excitation of nonradiative surface plasma waves in silver by the method of frustrated total reflection. *Zeitschrift für Physik A Hadrons and nuclei* **216**, 398–410 (1968).

110. Maradudin, A. A. Chapter 1 - Introduction: Plasmonics and its Building Blocks. in *Modern Plasmonics* (eds. Richardson, N. V. & Holloway, S.) vol. 4 1–36 (North-Holland, 2014).

111. Chiu, N.-F., Nien, S.-Y., Yu, C., Lee, J.-H. & Lin, C.-W. Advanced Metal Nanostructure Design for Surface Plasmon Photonic Bandgap Biosensor Device. *Conference proceedings: Annual International Conference of the IEEE Engineering in Medicine and Biology Society. IEEE Engineering in Medicine and Biology Society. Conference* **Suppl**, 6521–4 (2006).

112. Frazier, R. A. *et al. Handbook of Surface Plasmon Resonance*. vol. Chapte 1 (Royal Society of Chemistry, 2008).

113. Liebermann, T. & Knoll, W. Surface-plasmon field-enhanced fluorescence spectroscopy. *Colloids and Surfaces A: Physicochemical and Engineering Aspects* **171**, 115–130 (2000).

114. Szunerits, S. & Boukherroub, R. *Introduction to Plasmonics - Advances and Applications*. (2015).

115. Homola, J. *Surface Plasmon Resonance Based Sensors*. (Springer-Verlag Berlin Heidelberg, 2006).

116. Tumolo, T., Angnes, L. & Baptista, M. S. Determination of the refractive index increment (dn/dc) of molecule and macromolecule solutions by surface plasmon resonance. *Analytical Biochemistry* **333**, 273–279 (2004).

117. Photobiology. in *Introduction to Biophotonics* 159–202 (John Wiley & Sons, Ltd, 2003). doi: 10.1002/0471465380.ch6.

118. Lessard, R. A., Frank, W. F., & Society of Photo-optical Instrumentation Engineers. Polymers in optics: physics, chemistry, and applications. in p.86-113 (SPIE Optical Engineering Press, 1996).

119. Swalen, J. D. Optical wave spectroscopy of molecules at surfaces. *J. Phys. Chem.* **83**, 1438–1445 (1979).

120. Levy, Y., Imbert, C., Cipriani, J., Racine, S. & Dupeyrat, R. Raman scattering of thin films as a waveguide. *Optics Communications* **11**, 66–69 (1974).

121. Fahrenfort, J. Attenuated total reflection: A new principle for the production of useful infra-red reflection spectra of organic compounds. *Spectrochimica Acta* **17**, 698–709 (1961).

122. Veldhuis, G. J., Parriaux, O., Hoekstra, H. J. W. M. & Lambeck, P. V. Sensitivity Enhancement in Evanescent Optical Waveguide Sensors. *J. Lightwave Technol.* **18**, 677 (2000).

123. Wilkinson, J. S. Optical Waveguide Spectroscopy. in *Handbook of Spectroscopy* 1611–1642 (John Wiley & Sons, Ltd, 2014). doi:10.1002/9783527654703.ch48.

124. Lin, C.-Y. *et al.* Surface plasmon-enhanced and quenched two-photon excited fluorescence. *Opt. Express* **18**, 12807–12817 (2010).

125. Bauch, M., Toma, K., Toma, M., Zhang, Q. & Dostalek, J. Plasmon-Enhanced Fluorescence Biosensors: a Review. *Plasmonics* **9**, 781–799 (2014).

126. Helms, V. *Principles of Computational Cell Biology: From Protein Complexes to Cellular Networks*. (Wiley-Blackwell, 2018).

127. *Cy5 dye*. https://www.thermofisher.com/at/en/home/life-science/cell-analysis/fluorophores/cy5-dye.html.

128. Tsaftaris, A., Pasentzis, K. & Argiriou, A. Rolling circle amplification of genomic templates for inverse PCR (RCA–GIP): a method for 5'- and 3'-genome walking without anchoring. *Biotechnology Letters* **32**, 157 (2009).

129. Huang, Y., Xu, W., Liu, G. & Tian, L. A pure DNA hydrogel with stable catalytic ability produced by one-step rolling circle amplification. *Chemical communications (Cambridge, England)* **53**, 3038–3041 (2017).

130. Ducani, C., Bernardinelli, G. & Högberg, B. Rolling circle replication requires single-stranded DNA binding protein to avoid termination and production of double-stranded DNA. *Nucleic acids research* **42**, 10596–10604 (2014).

131. Lechner, B. Rolling circle amplification for plasmonic biosensors. (University of Natural Resources and Life Sciences, 2020).

132. Chi, Q., Wang, G. & Jiang, J. The persistence length and length per base of single-stranded DNA obtained from fluorescence correlation spectroscopy measurements using mean field theory. *Physica A: Statistical Mechanics and its Applications* **392**, 1072–1079 (2013).

133. *Freely jointed chain and characteristic ratio*. http://www.polymerdatabase.com/polymer%20physics/Kuhn.html.

134. Tinland, B., Pluen, A., Sturm, J. & Weill, G. Persistence Length of Single-Stranded DNA. *Macromolecules* **30**, 5763–5765 (1997).

135. Sim, A. Y. L., Lipfert, J., Herschlag, D. & Doniach, S. Salt dependence of the radius of gyration and flexibility of single-stranded DNA in solution probed by small-angle x-ray scattering. *Phys. Rev. E* **86**, 021901 (2012).

136. Milstein, J. N. & Meiners, J.-C. Worm-Like Chain (WLC) Model. in *Encyclopedia of Biophysics* (ed. Roberts, G. C. K.) 2757–2760 (Springer Berlin Heidelberg, 2013). doi:10.1007/978-3-642-16712-6_502.

137. *Kratky-Porod or worm-like chain model*. http://www.polymerdatabase.com/polymer%20physics/Wormlike%20Chain.html.

138. Gangotra, A. & Willmott, G. R. 3.12 - Cellular and Sub-Cellular Mechanics: Measurement of Material Properties. in *Comprehensive Nanoscience and Nanotechnology (Second Edition)* (eds. Andrews, D. L., Lipson, R. H. & Nann, T.) 227–244 (Academic Press, 2019). doi:10.1016/B978-0-12-803581-8.11286-X.

139. Stone, M. T. & Sanchez, I. C. Excluded volume scaling for polymers. *Computational and Theoretical Polymer Science* **9**, 117–123 (1999).

140. *Excluded volume and expansion factor of polymers*. http://polymerdatabase.com/polymer%20physics/Excluded%20Volume3.html.

141. *Temperature and concentration dependence of interaction paramter*. http://polymerdatabase.com/polymer%20physics/Chi%20%20Temp%20dependence.html.

142. Bowler, B. E. 3.5 Characterization of the Denatured State. in *Comprehensive Biophysics* (ed. Egelman, E. H.) 72–114 (Elsevier, 2012). doi:10.1016/B978-0-12-374920-8.00305-2.

143. Wang, X., Lim, H. & Son, A. Characterization of denaturation and renaturation of DNA for DNA hybridization. *Environmental health and toxicology* **29**, e2014007 (2014).

144. Biacore Sensor Surface Handbook BR100571 AC. (2017).

145. Björkesten, J., Patil, S., Fredolini, C., Lönn, P. & Landegren, U. A multiplex platform for digital measurement of circular DNA reaction products. *Nucleic Acids Research* **48**, e73–e73 (2020).

146. Fossati, S., Hageneder, S., Menad, S., Maillart, E. & Dostalek, J. Multiresonant plasmonic nanostructure for ultrasensitive fluorescence biosensing: *Nanophotonics* **9**, 3673–3685 (2020).

List of Figures

List of Tables